Christian Oswald

Tests of DEPFET pixel detectors and Simulation of the Belle II vertex detector

Diploma thesis
at the Faculty of Physics
Ludwig-Maximilians-Universität München
25th March 2011

First reviewer: Prof. Christian Kiesling
Second reviewer: Prof. Jochen Schieck

Advisers:
Assoc. Prof. Zdeněk Doležal and Peter Kodyš, PhD
Faculty of Mathematics and Physics
Charles University, Prague

Abstract

Belle II is a particle physics experiment located at the e^+e^--collider SuperKEKB in Japan. A part of the vertex detector will be equipped with DEPFET pixel sensors. Tests of various prototypes are carried out to chose the most suitable sensor layout. Mini matrices are particular test structures of 8×12 pixels. A low noise test system for these mini matrices is described and the dedicated software package is presented. Besides the hardware control programs, it contains steering scripts for various measurements and macros for the subsequent analysis. First measurements show the performance of the system. Furthermore, this thesis contributed the simulation of the geometry and materials of the vertex detector to the Belle II experiment.

Belle II ist ein Teilchenphysik-Experiment am e^+e^--Kollider SuperKEKB in Japan. Der Vertexdetektor wird zum Teil mit DEPFET-Pixelsensoren ausgestattet sein. Das geeignetste Sensorlayout soll aus einer Reihe von Prototypen mittels verschiedner Tests ausgewählt werden. Minimatrizen sind spezielle Teststrukturen mit 8×12 Pixeln. Es wird ein rauscharmes Testsystem für diese Minimatrizen beschrieben und das eigens entwickelte Softwarepaket vorgestellt. Es enthält neben Kontrollprogrammen für die Hardware auch Steuerungsskripte für verschiedene Messungen sowie Macros für die nachfolgende Auswertung. Erste Messungen zeigen die Leistungsfähigkeit des Systems. Weiterhin trug diese Arbeit mit der Simulation von Geometrie und Materialien des Vertexdetektors zum Belle II Experiment bei.

Contents

1. Introduction

> *Mais sais-tu au moins ce que c'est que de la matière? — Très bien, répondit l'homme. Par exemple, cette pierre est grise et d'une telle forme, elle a ses trois dimensions, elle est pesante et divisible. — Eh bien! dit le Sirien, cette chose qui te paraît être divisible, pesante et grise, me dirais-tu bien ce que c'est? Tu vois quelques attributs; mais le fond de la chose, le connais-tu? — Non, dit l'autre. — Tu ne sais donc point ce que c'est que la matière.*[1]
>
> Voltaire

The excerpt is from "Micromégas", a philosophical science fiction story published in 1752. Today's particle physicists still aim to find an answer to the question: What is matter? Our current description, the standard model, is a successful, well-tested theory which predicted numerous effects which have been verified experimentally. However, it is only a phenomenological description of the *attributes* of matter. As we started breaking the "grey stone" of Voltaire's story in smaller and smaller pieces, we could explain the origin of the grey colour, but finally ended up with a "red quark". The question about the origin of its attributes remains unanswered...

This thesis is a purely experimental one. In the rest of the introductory chapter, I would like to give though a rough impression of particle physics. It starts with a glimpse at elementary particles and the standard model before pointing out how our knowledge can be extended through collider experiments. Particular attention will be drawn to the BELLE II experiment. Finally, the outline of this thesis will be presented.

[1] *"But do you at least know what matter is?" — "We know it very well. For example this stone is grey and has a certain shape. It has three dimensions, and is heavy and capable of being divided into smaller parts." — "Good!" said the Sirian. "This thing that appears to you to be divisible and heavy, can you tell me what it is? You mentioned its attributes, but do you know its essence?" — "No," said the other. — "Then you do not know what matter is at all"* (translation cited from: Andrew Simoson: Voltaire's Riddle, 2010.)

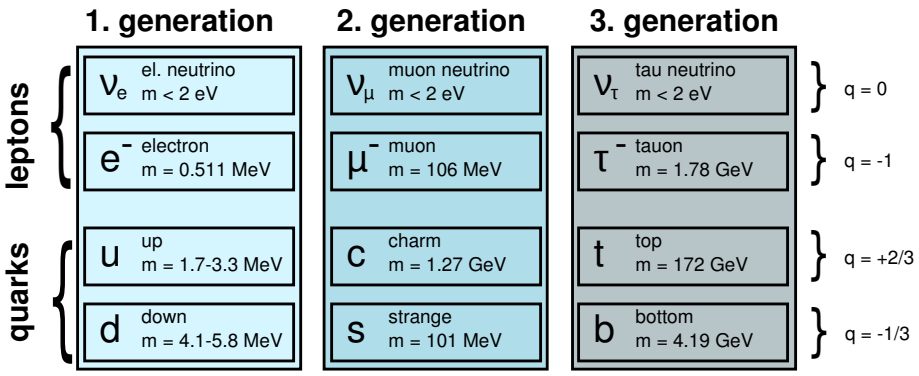

Figure 1.1.: The particles of the standard model (data from [1])

1.1. What is an elementary particle?

Elementary particle physics deals with the smallest subcomponents of matter. These are considered to be *point-like* and *indivisible*. Not all particles occurring in particle detectors are elementary particles. Leptons (= light particles), for example the electron, are considered to be elementary but hadrons (= heavy particles) for example the proton, contain a substructure.

The elementary particles discovered so far are summarised in Figure 1.1. Their properties and interactions are described by the *standard model*. The particles are organised in *three generations* or families. The first generation contains the elementary particles constituting ordinary atoms and the neutrino known from the beta decay. The particles of the second and third generation are identical[2] copies of the first generation but for one small detail: they carry different quantum numbers called *flavour* (for example "strangeness"). Like the electrical charge, the flavour should be conserved.

Every particle has an antiparticle as partner which has the same mass but with all the quantum numbers inverted. The quarks are particular because they carry an electric charge of $2/3\,\mathrm{e}$ and $-1/3\,\mathrm{e}$. To date only particles with a multiple of the elementary charge e have been discovered. This is explained by the fact that quarks only occur in nature bound in pairs (mesons) or triplets (baryons).

The standard model not only explains the composition of matter in terms of elementary particles but also describes dynamic processes such as decays and scattering. These processes can be explained by four fundamental interactions. The interactions themselves are described by the exchange of particles, the *vector bosons*:

[2]The discrepancies in the particle masses are only one minor flaw in the model. For more see the next section.

- electromagnetic interaction (photon: γ)
- weak interaction (W^+, W^-, Z^0)
- strong interaction (8 gluons: g)
- gravitation (graviton?)

Feynman diagrams (see Fig. 1.4) are used to describe these interactions. Every particle is represented by a continuous, dotted or curled line. However, these diagrams are not only a graphical representation. Their content can be translated to a mathematical description for calculating cross sections and decay probabilities. For some processes several different Feynman diagrams are possible and lead from the same initial to the identical final state. In this case all the diagrams contribute to the result of the process.

1.2. Broken symmetries and open questions

The picture of the world of elementary particles as drawn above is unfortunately too idealistic. Intuitively, one would expect that physical laws are the same under certain transformations for example the mirroring of the world at a plane. This transformation, also referred to as *parity transformation* P, flips axial vectors such as angular momenta. The relevant quantity in particle physics is the spin, which is flipped in a parity transformation.

The weak interaction violates this P symmetry[3]. A more global symmetry was re-established by the combination of the parity transformation P with the *charge conjugation* C, transforming a particle into its antiparticle. However, this CP symmetry was also found to be broken in the decay of K mesons and, more recently, B mesons. The fact that the CP symmetry is broken leads to a matter-antimatter asymmetry in the universe[4].

Furthermore, the weak interaction also violates the conservation of the quark flavour. The most prominent example is the beta-decay where a proton (uud) transforms into a neutron (udd), that is a u-quark becomes a d-quark. The situation is even more complex, since quark transitions between the three generations are possible.

[3]The violation is maximal, since the weak interaction takes place only with left-handed particles or right-handed antiparticles. The chirality refers to the direction of the particle spin with relation to the particle impulse.

[4]Although CP violation can explain a part of the matter dominance in the universe, there also have to be additional mechanisms which are still unknown.

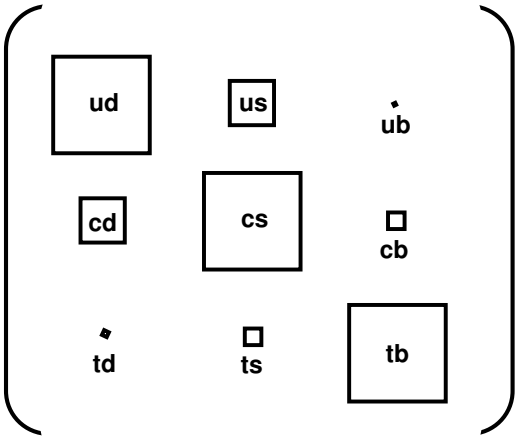

Figure 1.2.: Graphical representation of the CKM matrix (after [2])

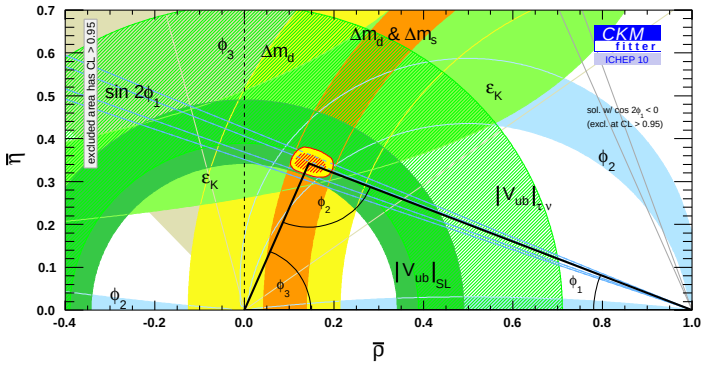

Figure 1.3.: Unitarity triangle with constraints from measurements [3]

The CP and flavor violations of the weak interaction are described mathematically by a unitary 3×3 matrix, the CKM[5] matrix. Figure 1.2 is a graphical representation of this matrix and illustrates that the diagonal elements are dominant. Physically, this means that decays within the same generation[6] are most probable. Due to the unitarity condition, the matrix is determined by 3 real parameters and 1 complex phase[7]. From the unitarity condition follows:

$$V_{ud}V_{ub}^* + V_{cd}V_{cb}^* + V_{td}V_{tb}^* = 0 \tag{1.1}$$

Each term can be interpreted as a vector in the complex plane. Equation 1.1 is then equivalent to the condition that these vectors form a closed triangle [4]. Figure 1.2 shows this triangle[8] using the naming convention ϕ_1, ϕ_2, ϕ_3 for the angles. The coloured areas represent constraints set by various measurements.

One further detail was left out in the discussion up to now: The standard model foresees a unification of the electromagnetic and weak interaction into an electroweak interaction. However, this creates a problem because the *massless* photon then belongs to the same interaction as the *very heavy*[9] W and Z bosons. Hence, a further symmetry is broken. The standard model can be saved by the introduction of a new particle, the famous Higgs boson[10], which has yet to be discovered.

Besides the missing Higgs boson, there are further unanswered questions. Why are the masses of particles from different generations so different? Is it possible to unify all four known fundamental interactions? How can the hierarchy of the CKM matrix be explained? Are there other mechanisms to explain the matter-antimatter asymmetry in the universe? Finally, the standard model contains too many free parameters, namely 18. It would be desirable to deduce these parameters from a more fundamental principle [2].

1.3. The search for new particles

There are two complementary approaches to discovering new particles. Either create the particles *directly*, by colliding available particles (for example protons) at *high energies*; or to carry out experiments with *high statistics* and use these to deduce the existence of new particles *indirectly*. [5].

[5] Cabibbo, Kobayashi, Maskawa
[6] $u \to d$, $c \to s$, $t \to b$
[7] The other 5 complex phases have no physical meaning.
[8] normalised with a factor $(|V_{cd}||V_{cb}|)^{-1}$
[9] $m_W = 80\,\text{GeV}$, $m_Z = 91\,\text{GeV}$ [1]
[10] There has to be at least one Higgs boson, but models with more Higgs bosons also exist

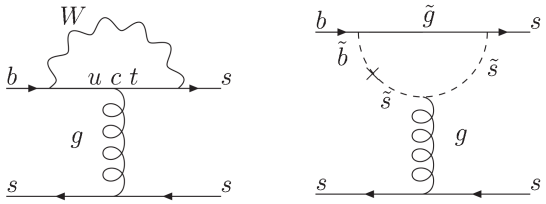

Figure 1.4.: Standard model process (left), SUSY process (right) [5]

The ATLAS and CMS experiments at LHC[11] follow the first approach. Protons are accelerated to a collision energy of up to $2 \times 7\,\mathrm{TeV}$, but the possible rest mass of the created particles is limited to $1\,\mathrm{TeV}$[12] The probability of discovering a new particle depends on the production cross section, the luminosity of the accelerator and the efficiency of the detector. In other words, one only has to wait long enough until the unknown particle (e.g. the Higgs boson) shows up.

The planned experiments with the Belle II detector will use the second approach and try to infer the existence of new particles by studying flavour physics reactions with high statistics. The results of these experiments will be compared to the predictions of the standard model. Discrepancies from the expected outcome point to new physical effects. However, these discrepancies are very small, as, otherwise, they would already have been discovered. Higher statistics improve the precision of the measurements and permit the discovery of even smaller deviations from the expectation.

A detailed overview of the physics prospects at the Belle II experiment is given in reference [2]. The following example (base on reference [5]), will illustrate how discrepancies from standard model predictions are discovered through measurements with high statistics.

The B^0 and $\bar{B}^0$ mesons produced at the SuperKEKB accelerator (see below) decay with a certain probability which can be calculated by means of Feynman diagrams. If a large number of these decays is measured, a decay time distribution is obtained. The possibility of $B^0\bar{B}^0$ mixing before the decay makes the decay time distribution sensitive to $\sin 2\phi_1$, a parameter from the unitarity triangle.

The value of $\sin 2\phi_1$ can be determined by analysing decay time distributions from different decays: $B^0 \to \phi K_S$ and $B \to J/\psi K_S$. The standard model predicts that

[11] Large Hadron Collider

[12] Since protons are not elementary particles, the kinetic energy is shared between their subcomponents (quarks and gluons). Hence, the energy available for the production of new particles is reduced.

the difference between the two measurements $\Delta S \equiv \sin 2\phi_1^{\phi K_S} - \sin 2\phi_1^{J/\psi K_S}$ is small: $\Delta S = 0.03 \pm^{0.04}_{0.01}$.

Consider the process $B^0 \to \phi K_S$. The corresponding Feynman diagram is shown in Figure 1.4 (left). However, new physics processes might also contribute to the decay, for example the process with supersymmetric particles presented in Figure 1.4 (right). This additional contribution results in a small change in the decay probability and consequently a change in the decay time distribution. Since the change is only small, the decay time of the B^0 has to be measured a large number of times to produce a statistically meaningful decay time distribution. The presence of a new physics process would be indicated by a deviation of ΔS from the standard model prediction.

1.4. The Belle II detector at SuperKEKB

1.4.1. The SuperKEKB accelerator

The necessity of high statistics for certain measurements was demonstrated above. Hence, the decision was made to upgrade the former KEKB collider to the SuperKEKB e^+e^-–collider with a higher production rate of B mesons. The higher production rate is achieved technically through an increase of the *luminosity* of the collider. The luminosity $\mathcal{L}$ is the proportionality constant relating the cross section σ to the number of events N. A higher luminosity yields more observations and hence better statistics.

$$N = \mathcal{L} \cdot \sigma \tag{1.2}$$

In the SuperKEKB collider electrons and positrons will be accelerated to different energies (7 GeV and 4 GeV) and then brought into collision. The produced $\Upsilon(4S)$ resonance (an excited state of the $b\bar{b}$ system) decays into a pair of B mesons which have a boost in one direction due to the asymmetry of the beam energies. Producing bottom quarks is of particular interest because they are from the third quark generation and involve all other generations in their decays[13].

1.4.2. The Belle II detector

During the upgrade of the accelerator from KEKB to SuperKEKB, the associated Belle detector will also undergo some improvements and also be prepared for the higher luminosity in the upgrade. Figure 1.5 shows the layout of the whole Belle II detector compared to the former Belle detector. Particles created at the interaction point in the centre fly apart in all directions and have to pass several detector layers.

[13]The production of top quarks is technically not possible due to their much higher rest mass.

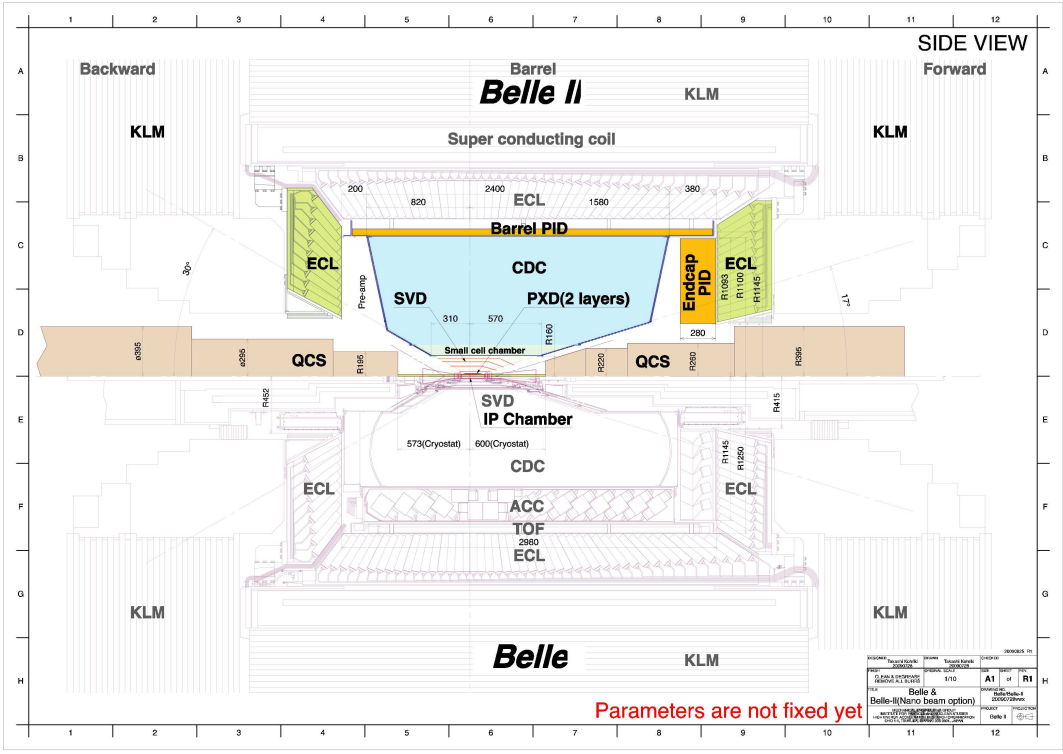

Figure 1.5.: The Belle II detector and its predecessor Belle [5]

The innermost detector is the vertex detector (PXD, SVD) which allows the precise determination of the decay vertex of the particles produced. In the drift chamber (CDC) the momentum of charged particles is determined from the curvature of their tracks in the magnetic field. After crossing the particle identification devices (PID) the energy of the particles is measured in the electromagnetic calorimeter (ECL). The last layer(KLM) is a detection system for K_L mesons and muons. The detectors cover a solid angle of $\phi = 0$ to $360°$ and $\theta = 17$ to $170°$ corresponding to the area of physical interest.

1.4.3. The Belle II vertex detector

B^0 mesons decay by the weak interaction with typical decay times of the order of 10^{-12} s [1]. A direct measurement of such short times impossible. However, the created particles have a boost in one direction due to the asymmetric beam energies. The measurement of the *decay time* therefore corresponds to a measurement of the *decay vertex* which is reconstructed by tracing back the tracks of the decay products with the vertex detector.

The upgraded vertex detector will contain six layers of silicon sensors. Figure 1.6 shows the simulated geometry of the vertex detector. The two inner layers (PXD) are equipped with pixel sensors. They are followed by four outer layers (SVD) of strip sensors. The silicon sensors of all layers are arranged in a *windmill structure* in order to cover the full space in ϕ direction (= rotation about the z-axis). The outer radius of the sixth layer will be as small as 14 cm.

Silicon sensors detect the position of passing particles with structured electrodes. In the simplest case the electrodes are set up as strips allowing a position measurement of the passing particle in one dimension. If two strip detectors are arranged crosswise, a two dimensional position measurement is possible. Each layer of the SVD contains such assemblies of two strip detectors. When more than one particle passes, the position measurement becomes ambiguous as illustrated in figure 1.7. This ambiguity can be resolved by combining the information from other detectors.

The increased luminosity of the SuperKEKB machine creates a particular challenge because it leads to a higher background (= processes of no physical interest). Hence, the number of particles hitting the detector per unit time is also increased. The fraction of strips hit per readout cycle is called the *occupancy* of the detector. If the occupancy is too high, the detector cannot provide unambiguous position information anymore. The closer the detector is positioned to the interaction point the higher the occupancy, because the same flux of particles has to pass through a smaller sensor surface.

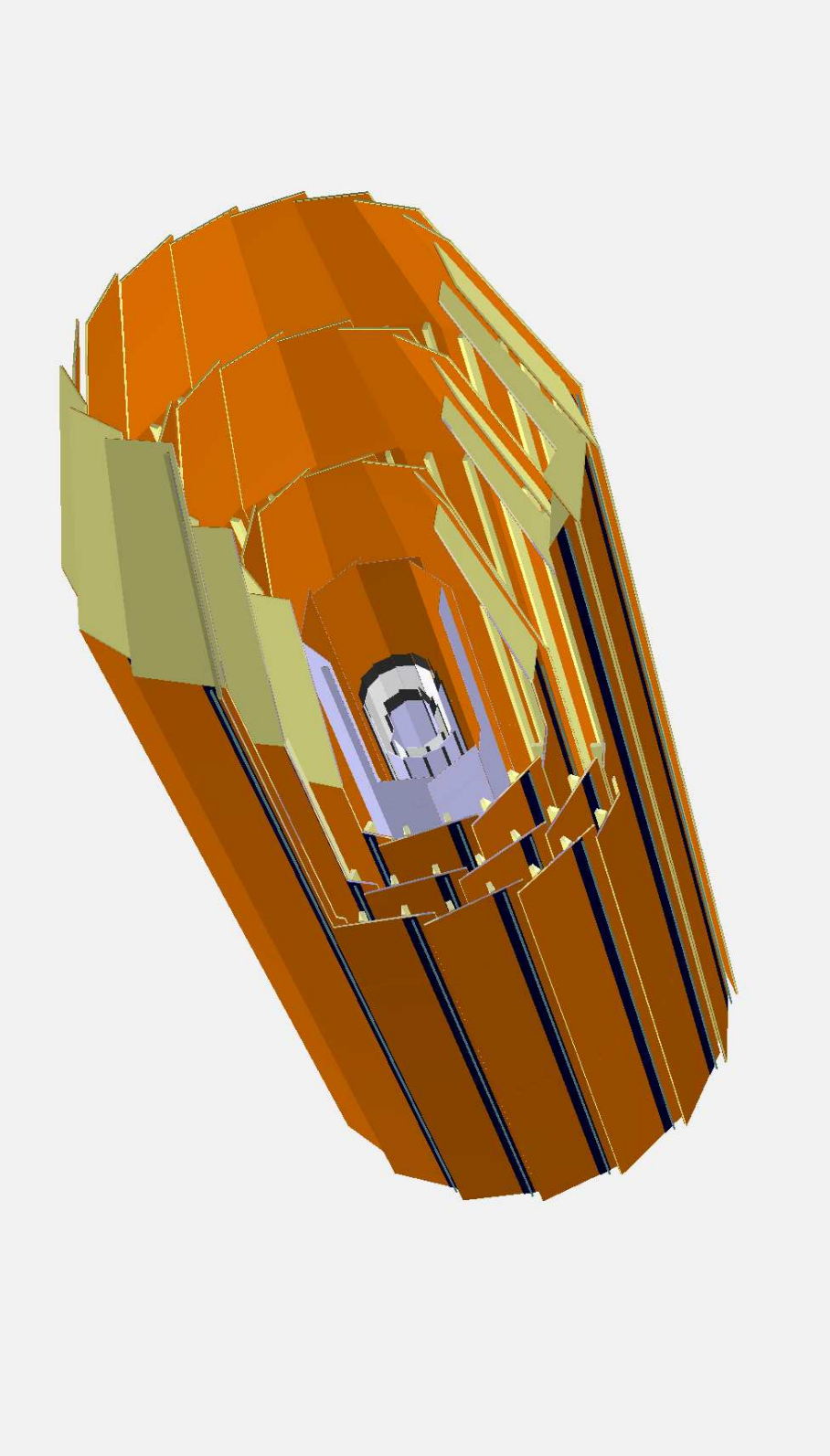

Figure 1.6.: Simulated geometry of the Belle II vertex detector

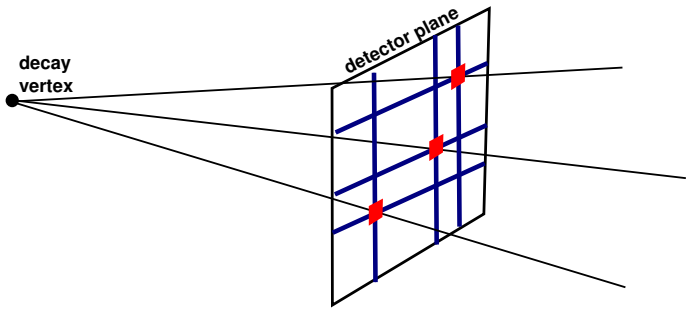

Figure 1.7.: Response of strip detectors arranged crosswise (in blue) and of a pixel detector (in red) (after [6])

This problem is partly overcome with a pixel detector (cf. Fig. 1.7) which is structured in two dimensions. The two innermost layers of the vertex detector are mounted directly on the beam pipe and equipped with DEPFET pixel sensors.

1.5. Overview of the thesis

While the SUPERKEKB accelerator is built and financed by a Japanese initiative, the construction effort of the Belle II detector is shared in the international *Belle II collaboration*. The PXD is built by the separate *DEPFET collaboration* comprising members from China, the Czech Republic, Germany, Poland and Spain. Individual institutes are responsible for tasks such as development, production and testing of the DEPFET sensors, building of a cooling system or design studies.

The results of this thesis were obtained at the Institute of Particle and Nuclear Physics (IPNP), at the Faculty of Mathematics and Physics, Charles University in Prague. This institute is involved in both collaborations mentioned above. A brief introduction to the theory of semiconductor detectors (chapter 2), is followed by the two main parts of this thesis. The first part (chapter 3-5) was prepared in the framework of the DEPFET collaboration. A test system for small prototypes of DEPFET sensors was built and first measurements were performed as a contribution to the selection of the optimal sensor for the PXD. The second part (chapter 6) was the simulation of the geometry and materials of the Belle II vertex detector (PXD+SVD). This was an important contribution within the Belle II collaboration, since the funding agencies requested a full simulation of the complete detector before they were willing to give a full approval to the project.

2. Particle detection with semiconductor detectors

Particle detection is generally based on the interaction of the particles with matter. In the view of a particle physicist the matter of the detector itself is made of elementary particles. The effect of a particle crossing matter can therefore be broken down into a number of single interactions between elementary particles. The results of these interactions are then converted to a form adequate for further processing (e.g. a picture on a photographic plate or electric signals).

In this chapter, after a short summary about semiconductors, the processes describing the interaction of charged particles and photons with a semiconductor are introduced (where possible, silicon is chosen as example). All these processes have in common that free charge carriers are produced, which are detected using a reversely biased pn-junction.

2.1. Semiconductors

Semiconductors are characterised by their small energy gap E_g of typically 1 eV between conduction and valence band (see Fig. 2.1). Charge transport is effectuated by free electrons (= electrons in the conduction band) or holes (= missing electron in the valence band).

Semiconductors with a negligible number of impurities are called intrinsic. It can be shown that the product of the concentration of free electrons and holes

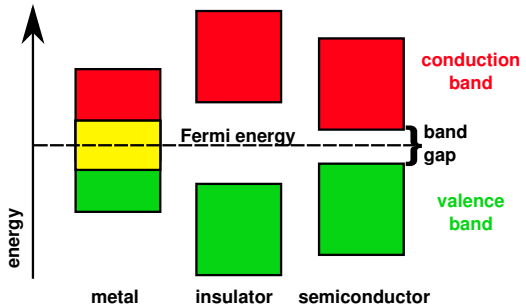

Figure 2.1.: Band structure of metal, insulator and semiconductor

is independent of the Fermi level and thus independent of the concentration of impurities [6]:

$$np = {n_\mathrm{i}}^2 = N_\mathrm{C} N_\mathrm{V} \exp\left(-\frac{E_\mathrm{g}}{kT}\right) \tag{2.1}$$

N_C	effcetive density of states in the conduction band
N_V	effective density of states in the valence band

In intrinsic semiconductors the concentrations of free electrons and holes are equal[1]: $n_\mathrm{i} = n = p$ ($n_\mathrm{i} \approx 1.5 \cdot 10^{10}\,\mathrm{cm}^{-3}$ for silicon at 300 K [7]).

Building semiconductor devices requires a change in the concentrations n and p in a way that one of them becomes dominant. This is achieved by introducing a fraction ($10^{-9} \ldots 10^{-2}$ [8]) of impurities (dopants) in the crystal lattice.

Most semiconductor sensors are made of silicon which belongs to group IV of the periodic table. To produce n-type Silicon, atoms from group V (e.g. Ph or As) are used as dopants. Each silicon atom has covalent bonding to its four neighbours. Hence, the dopant is forced to build up the same bonding when it is integrated in the crystal lattice. There is one excess electron, which is only weakly bound to the nucleus and can be easily ionised (the energy difference to the conduction band is only 0.05 eV). Since the introduced element provokes an increase in the concentration of free electrons, it is called a *donor*. Electrons as *majority carriers* become responsible for the charge transport, holes are *minority carriers*.

A similar process takes places for the introduction of group III materials (acceptors) which leads to an increase in the number of holes and creates a p-type semiconductor with holes as majority carriers.

As this thesis deals with a semiconductor detector for high energy physics, it is important to note at this point that the detector will be exposed in its future application to a harsh radiation environment, encountering high doses. Reactions of the impinging particles with nuclei cause irreversible damages to the crystal lattice and result in the introduction of new energy levels. The effective doping concentration changes and type inversion (n-type silicon becomes p-type) is even possible [6].

2.2. Interaction of charged particles

The main interaction mechanisms of charged particles with matter are inelastic collisions with atomic electrons, elastic scattering from nuclei and bremsstrahlung. Čerenkov radiation and nuclear reactions are of minor importance [8].

[1] Each electron excited to the conduction band leaves a hole in the valence band.

2.2.1. Energy loss of heavy charged particles

The interaction of heavy charged particles is dominated by inelastic collisions with the atomic electrons of the detector material. Most probable are soft collisions transferring only a small fraction of the particles' kinetic energy and leaving the atom in an excited state. Hard collisions occur less often and result in ionisation of the atom. In particular cases, the energy of the recoil electron (delta electron) is high high enough to cause secondary ionisations.

Elastic scattering from nuclei plays a minor role. Only a small amount of energy is transferred because usually the mass of the nucleus is much larger than the mass of the impinging particle.

The energy loss is described by the Bethe-Bloch formula:

$$-\frac{\mathrm{d}E}{\mathrm{d}x} = 2\pi N_a {r_e}^2 m_e c^2 \rho \frac{Z}{A}\frac{z^2}{\beta^2}\left[\ln\left(\frac{2m_e\gamma^2 v^2 W_{\max}}{I^2}\right) - 2\beta^2 + \ldots\right] \tag{2.2}$$

I	Mean excitation potential
Z, A, ρ	refer to absorbing material
z	Charge of incident particle
β, γ	Velocity and Lorentz factor of incident particle
$W_{\max}$	Maximum energy transfer in a single collision

The formula is usually extended by supplementary corrections, for example the density and shell corrections.

A graphical representation of the Bethe-Bloch formula for different particles is given in Figure 2.2. The minimum energy loss is at $\beta\gamma \approx 3$ and is approximately the same for all particles. Particles with this velocity are often referred as minimum ionising particles (MIP).

In the region below the minimum ionisation, the energy loss increases towards lower kinetic energies, which means that slow particles loose more energy than fast particles. Each particle has its characteristic energy loss, and the Bethe-Bloch curves can be well distinguished. This is exploited for particle identification. When the velocity of the particle is decreased further, it is then of the same order of magnitude as the velocity of the orbital electrons of the material ($\beta < 0.1$), and the Bethe-Bloch formula becomes invalid.

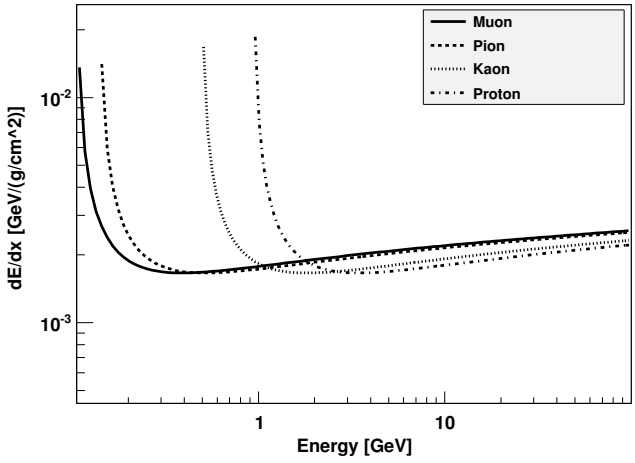

Figure 2.2.: Application of the Bethe-Bloch formula to silicon

In the region above the minimum ionisation, the curve is rather flat and the energy loss grows only slowly (relativistic rise), and the minimum energy loss remains a good approximation.

2.2.2. Energy loss of electrons and positrons

The energy loss of electrons and positrons is described by a modified version of the Bethe-Bloch formula which takes into account that a deflection of these light particles in the the collision process is more likely. A further modification is necessary for electrons, because they are quantum mechanically indistinguishable from the atomic electrons.

At higher energies (tens of MeV), collisions become less important and bremsstrahlung is the almost exclusive energy loss mechanism. In this regime the energy loss of electrons is described by an exponential law:

$$E(x) = E_0 \exp\left(-\frac{x}{X_0}\right) \tag{2.3}$$

The radiation length X_0 indicates the distance after which an electron has lost $1/e$ of its initial energy E_0.

2.2.3. Energy loss distributions

The energy loss presented above is a mean value obtained in a stochastic process of multiple collisions. The actual energy loss is subject to fluctuations and described by an energy loss distribution. In relatively thick absorbers, the distribution is Gaussian, since the relative energy loss is small and the number of collisions is high (Central Limit Theorem).

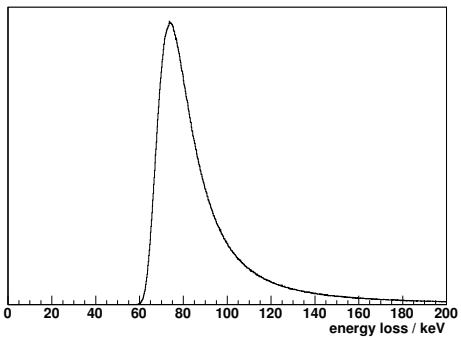

Figure 2.3.: Example of a landau distribution

The situation changes for a thin absorber such as a silicon waver. In this case the number of collisions is too small to apply the Central Limit Theorem. The calculation becomes extremely complicated, since large energy transfers are already possible in a single collision. Landau derived a frequently used distribution making the following assumptions [8]:

- The average energy transfer is much smaller than the maximum allowable energy transfer.
- Only "close"[2] collisions are considered.
- The particle velocity remains approximately constant.

An example of a Landau distribution is given in Figure 2.3. Bak et al. [9] measured the energy loss distribution in silicon for different thicknesses. While the Landau theory is in good agreement with the measurements for silicon of 1040 µm, the measured distribution for thinner samples (especially below 100 µm) becomes wider, and the most probable energy loss is shifted to a lower value than predicted. Bak et al. propose a more adequate energy loss distribution and also cite other approaches [9].

2.3. Interaction with photons

Photons interact with matter via three distinctive mechanisms: photo effect, Compton effect and pair production. The probability of an interaction by each of these mechanisms depends on the photon energy as depicted in Figure 2.4. Photons interacting with matter are either destroyed completely (photo effect, pair production) or significantly deflected (Compton effect). Hence, the intensity of a photon

[2]The term "close" refers to the classical picture of an impact parameter b which is related to the momentum transfer q by $b \sim \hbar/q$ [9]

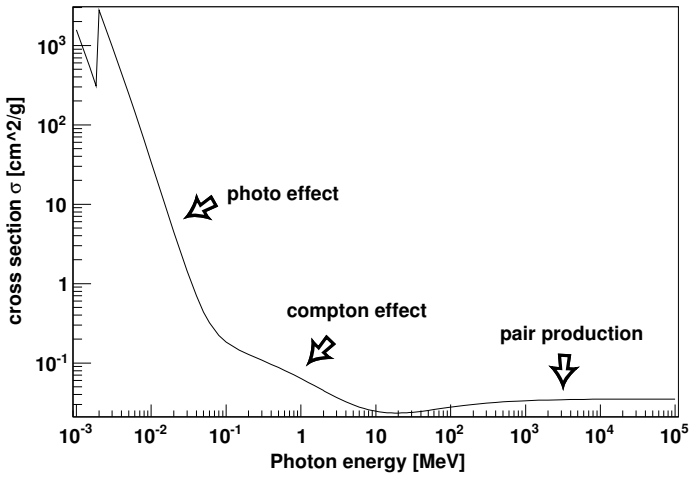

Figure 2.4.: Photon cross section (data: [1])

beam is reduced when it crosses a piece of matter, in contrast to a beam of charged particles which looses energy. The measurements reported in this thesis were performed with laser light of 660 nm and X-rays of 6 keV and 20 keV. Therefore, the photo effect is discussed in greatest detail below.

2.3.1. Photo effect

The photo effect concerns primarily photons with energies below 100 keV. The photon is completely absorbed in this process and its energy transferred to an atomic electron.

Since the conservation of momentum holds, the nucleus has to take over the recoil momentum of the electron. That is why the photo effect never occurs on free electrons. The photo effect is a binomial process: either the energy of the photon is completely transferred to the material (which means that the photon is destroyed in this process) or nothing happens at all.

Photo conductivity

In a semiconductor, the transferred photon energy can excite the electron from the valence band to the conduction band. This effect is called photo conductivity as it increases the conductivity of the semiconductor. In an indirect semiconductor (e.g. silicon), phonons are involved in the excitation process.

The absorption probability can be expressed in terms of an absorption length as a function of the wavelength of the photon. Figure 2.5 shows the curve for

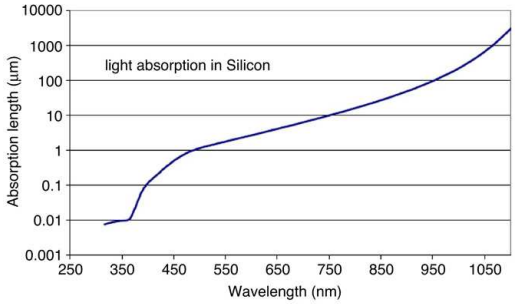

Figure 2.5.: Absorption length of photons [11]

pure[3] silicon. At short wave lengths ($< 400\,\text{nm}$), direct transitions without the involvement of phonons are possible, and the absorption length is very small. In this case, electron hole pairs are mostly generated mostly at the surface of the detector, where the detector might be insensitive (silicon not depleted, cf. chapter 2.4). The absorption length increases with increasing wavelength (smaller energy transfer). At 1100 nm, the photon energy equals the band gap, and for wavelengths beyond this value an absorption becomes very unlikely: The absorption length exceeds the typical detector thickness ($100 \ldots 450\,\mu\text{m}$), and the detection efficiency breaks down.

Photo ionisation

If the photon energy E is higher than the binding energy of the electron E_B, it can be completely removed (ionised) from its nucleus. For X-rays, the deposited energy is high enough to create more than one electron-hole pair. The average energy needed to create an electron-hole pair in silicon is about 3.6 eV, which is more than the band gap of 1.12 eV because a part of the energy is spent in other processes than electron-hole generation [11].

The absorption length d can be calculated by using the cross section σ from reference [12] and the relation:

$$p = \frac{1}{e} = \sigma \cdot \rho \cdot d \tag{2.4}$$

Figure 2.6 shows a graphical representation of the absorption length of photons in the range from 1 keV to 40 keV. Already at 20 keV, the absorption length becomes higher than the typical thickness of a silicon detector, and the detection probability is therefore reduced significantly.

[3] Silicon sensors contain other materials than silicon, for example metals for the electrical connections. A big issue is the dependence of the reflectance on the properties of the sensor surface. Also, interference effects in protection layers, having a thickness of tens to hundreds of nm, change the reflectance in a range of 30 to 95%. [10]

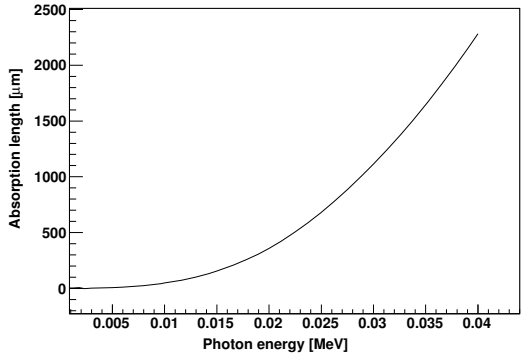

Figure 2.6.: Absorption length of photons (data: [12])

2.3.2. Compton scattering

For photon energies between 100 keV and 5 MeV, Compton scattering is the dominant process. In this range the photon energy is already significantly higher than the binding energy of the electron and the electron can be treated as a free electron. Compton scattering involves a change in momentum and energy of the photon. The cross section is given by the Klein-Nishina formula, which can be found in the literature [8]. The maximum recoil energy of the electron corresponds to the case when the entire energy of the photon is transferred to the electron (i.e. the scattered photon energy is zero). This value is also known as Compton edge and is used for detector calibration.

2.3.3. Pair production

When the photon energy reaches twice the rest energy of an electron $h\nu = 2 \times 511\,\text{keV}$, the production of an electron positron pair becomes possible. Similarly, as for the photo effect, the presence of a nucleus is necessary in order to conserve momentum. For high energy photons, the cross sections of photo effect and Compton scattering become negligible, and the mean free path $\tilde{\lambda}$ of the photons is given by [8]:

$$\tilde{\lambda} = \frac{9}{7} \cdot X_0 \tag{2.5}$$

Hence, the radiation length X_0 characterises not only the energy loss of high energy electrons, but also of high energy photons. In the construction of detector systems it is an essential parameter. For tracking detectors, one tends to reduce the influence of the detector on the particle and goes for high values of X_0. Calorimeters, on the other hand, require complete absorption of the particle energy and are built of materials with small X_0.

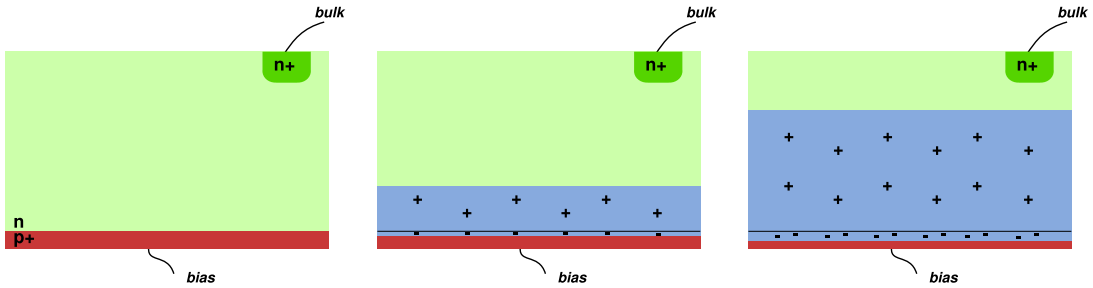

(a) schematic view

(b) space charge region leading to built-in voltage

(c) space charge region extended by external bias voltage

Figure 2.7.: The pn-diode. (Colour key: light green = n-type silicon, dark green = highly doped n-type silicon, dark red = highly doped p-type silicon, light blue = space charge region)

2.4. The pn-junction as sensitive element

In the previous sections of this chapter, I have introduced different processes which result in the creation of free charge carriers. The next step in building a particle detector is to detect the created charge. The heart of a semiconductor detector is the pn-junction, which is, as the name suggests, a p-type and an n-type semiconductor brought together in the same device (fig. 2.7(a)).

2.4.1. Built-in voltage and space charge region

In the n-doped part of the device, there is an excess of available electrons, while, in the p-doped part, there is an excess of holes (i.e. a lack of electrons). Therefore, electrons from the n-part diffuse to the p-part leaving back positively charged ions, while negative charge is accumulated in the p-part. This process is counteracted by the rising electrical field created between the "new" electrons in the p region and the positive ions left back in the n-region (fig. 2.7(b)).

Finally, an equilibrium is established between these two processes. The resulting region is called *depletion zone* or *space charge region*. Depletion means that there are no free charge carriers in this region, but only the positively charged immobile nucleus on the n-side and the new electrons on the p-side. The region holds the properties of an insulator.

The *built in voltage* U_{bi} is defined as the voltage at the boarders of the depletion zone. A typical value is $U_{\mathrm{bi}} \approx 0.5\,\mathrm{V}$. It can be calculated from the concentrations of donors (N_{D}) and acceptors (N_{A}) [6]:

$$U_{\mathrm{bi}} = \frac{kT}{e} \ln\left(\frac{N_{\mathrm{D}} N_{\mathrm{A}}}{{n_{\mathrm{i}}}^2}\right) \tag{2.6}$$

Assuming an abrupt junction between n-type and p-type silicon[4] and no thermal generation and diffusion of charge carriers, the electric field in the space charge region is linear with a maximum at the junction because the charges are uniformly distributed. The field is obtained by solving the Poisson equation [11]:

$$E = -\frac{qN}{\epsilon}(d - z)\ 0 < z < d \tag{2.7}$$

$$E = 0\ z > d \tag{2.8}$$

NB: On each "side" of the depletion region the same absolute value of space charge is located. Let's consider a highly doped p+ region[5] with a high density of space charges on the one side and a lean doped n bulk with low density of space charges on the other. Obviously, the depleted volume is much smaller on the p+ side than on the n side (fig. 2.7(b)). As a result, the thickness of the depleted region can be controlled by adjusting the doping concentrations.

2.4.2. Reverse bias and full depletion

Application of a reverse bias voltage U_{bias} counteracts the repulsing force of the electric field created by the space charge and leads to an extended depletion zone (fig. 2.7(c)). Its thickness d is given by [6]:

$$d \approx \sqrt{\frac{2\epsilon_0\epsilon_{\text{Si}}}{eN_{\text{D}}}U_{\text{bias}}} \tag{2.9}$$

At a certain voltage U_{depl} the depletion zone covers the full thickness of the device. Such fully depleted diodes can be used as particle detectors. The free charge carriers created by impinging particles drift in the electrical field of the space charge region to the electrodes and are detected as a current.

2.4.3. Leakage current and noise

The ideal picture of the reversely biased pn-junction has to be corrected, because even without any external influence a *leakage current* flows through the device. Two effects play a role, namely, the diffusion of free charge carriers from undepleted regions and, more importantly, the thermal generation of electron-hole pairs at generation-recombination centres [6].

[4]Real devices comprise a transition region [7].
[5]The + indicates a high concentration of dopants.

Noise are small fluctuations of the measured signal current. Three types of noise contribute to the overall noise of the detector [13]:

- The electrical current is defined as $I = \frac{\mathrm{d}q}{\mathrm{d}t}$. Since the charge q is a discrete quantity and a current is nothing else than the transport of individual electrons, temporal fluctuations of the number of transported electrons result in *shot noise*.
- White or *thermal noise* is, as the name suggests, caused by the thermal agitation of the electrons.
- Crystal defects representing trapping centres generate flicker or *low frequency noise*.

In the DEPFET sensor described in the next chapter, thermal noise is the dominant source of noise. However, the contribution of the other types of noise is increased after heavy irradiation [14].

3. The DEPFET - a semi-monolithic pixel detector

In this chapter, the concept and operation of DEPFET[1] pixels is described. Different types of DEPFET pixels and their arrangement in matrices are discussed. The chapter closes with a brief summary of other pixel detectors, and the special features of the DEPFET are pointed out.

3.1. The DEPFET detector

The idea behind the DEPFET pixel detector is to read out the created charge not directly as a current, but to first collect and store it at an internal potential minimum first, then read it out via a MOSFET structure, and finally to reset the pixel. This idea was already proposed in 1987 by Kemmer and Lutz [15].

3.1.1. Charge collection: Sidewards Depletion and Internal Gate

Charge is collected and stored by creating a potential minimum for electrons in the bulk silicon. The DEPFET device collects electron by two means, namely, sidewards depletion and a deep n+ implant called internal gate.

Sidewards depletion

Gatti and Rehak proposed in 1984 a silicon device depleted from both sides by introducing an additional p+ implant at the opposite side [16]. Figure 3.1(a) illustrates the principle in a schematic way. By increasing the bias voltage U_{bias}, the resulting depletion zone then grows from front and back plane until both depleted zones touch each other (fig. 3.1(b)).

The thickness of the depletion regions and the position where the regions are touching can be influenced by the concentration of dopants in the n-bulk and the p+-implantations. In DEPFET devices the depleted regions touch each other about 1 µm below the sensor surface [17]. Considering the charge distribution in the device (fig. 3.1(b)), the touching region is obviously a potential minimum for electrons. When electron/hole pairs are created in the depleted bulk, the electrons drift to this region and the holes drift to the p+ contacts.

[1] DEPleted Field Effect Transistor

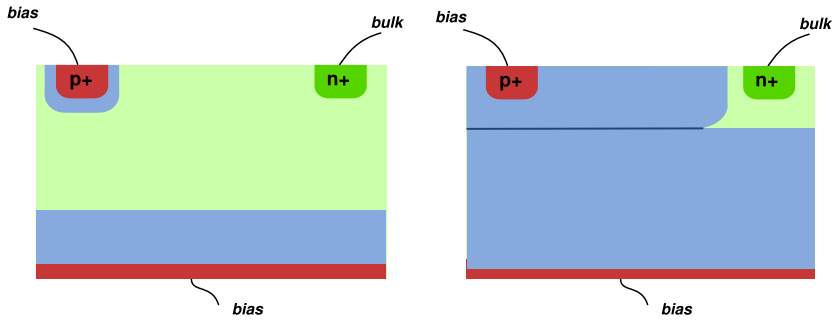

(a) unbiased (b) depletion from top and bottom

Figure 3.1.: Sidewards depletion. (Colour key: light green = n-type silicon, dark green = highly doped n-type silicon, dark red = highly doped p-type silicon, light blue = space charge region, dark blue = potential minimum for electrons)

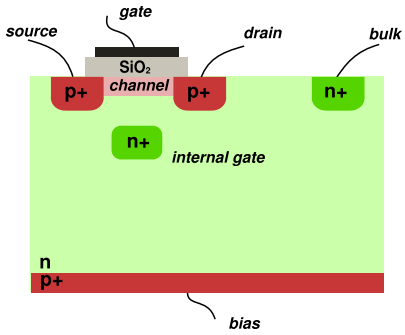

Figure 3.2.: Schematic of a DEPFET sensor. (Colour key: light green = n-type silicon, dark green = highly doped n-type silicon, light red = p-type silicon, dark red = highly doped p-type silicon, light grey = silicon oxide)

Internal gate

The electrons collected by sidewards depletion can still wander in a layer parallel to the sensor surface. When building a pixel detector, this diffusion must be prevented and the charges fixed at a defined place. This can be achieved by means of an additional n+-implantation. This implantation serves as internal gate of a MOSFET transistor and influences its source-drain current. This is explained in the next section.

3.1.2. Charge measurement: The MOSFET

MOSFET transistors are used for amplification of small charges and currents, and various designs exist. Here, only the depletion-mode p-channel type is described. A

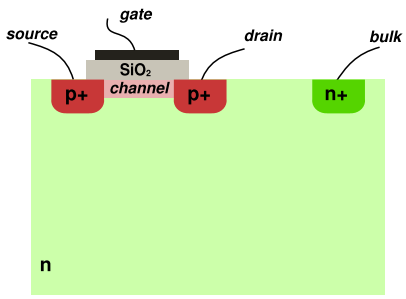

Figure 3.3.: MOSFET with p-channel. (Colour key: light green = n-type silicon, dark green = highly doped n-type silicon, light red = p-type silicon, dark red = highly doped p-type silicon, light grey = silicon oxide)

MOSFET is based on a MOS structure, that is a system of three layers: a (M)etal layer on top, an insulating layer of silicon (O)xide and the n doped (S)ilicon bulk. Further, there are two p+-implantations which form the source and drain contact (fig. 3.3). In the depletion-mode MOSFET the two p+-implantations are connected via a p-channel allowing a current to flow from source to drain contact (the charge transport is accomplished by positively charged holes). The situation changes when the gate contact (metal) is at positive potential. Then electrons are attracted to the p-channel and "fill" the holes, which leads to a decrease of the concentration of charge carriers in the p-channel. Hence, less current I_{sd} can flow from source to drain. The strength of this effect depends on the potential at the gate. If the potential is high enough, (nearly) no current flows - the transistor is completely closed.

In the DEPFET, the source-drain current I_{sd} is additionally affected by the charge at the internal gate. The change of I_{sd} can be exploited to deduce the amount of charge which is created by the impinging particle and then collected at the internal gate. This adds a term $fQ_{\mathrm{sig}}/C_{\mathrm{ox}}$ to the formula describing the source-drain current of a generic MOSFET. The factor f models how strongly the charge at the internal gate influences the source-drain current. Details of how this formula can be obtained are given in reference [14].

$$I_{\mathrm{sd}} = \frac{1}{2}\frac{W}{L}\mu_p C_{\mathrm{ox}}\left(f\frac{Q_{\mathrm{sig}}}{C_{\mathrm{ox}}} + U_{\mathrm{gs}} - U_{\mathrm{THR}}\right)^2 \tag{3.1}$$

I_{sd}	source-drain current
W	width of the transistor gate
L	length of the transistor gate
μ_p	mobility of the holes
C_{ox}	oxide capacitance $WL/(\epsilon_0\epsilon_{\mathrm{ox}}d)$
$C_{\dot{\mathrm{o}}\mathrm{x}}$	sheet capacitance $1/(\epsilon_0\epsilon_{\mathrm{ox}}d)$
f	reduction factor taking into account parasitic coupling
Q_{sig}	charge at the internal gate
U_{gs}	gate-source voltage
U_{THR}	threshold voltage

The derivation of this formula with respect to U_{gs} results in the transconductance g_{m} of the MOSFET. The *internal amplification* g_q of the DEPFET is obtained by derivation with respect to Q_{sig}:

$$g_q = \frac{\mathrm{d}I}{\mathrm{d}Q_{\mathrm{sig}}} = \frac{1}{L^2}\mu_p f\left(f\frac{Q_{\mathrm{sig}}}{C_{\mathrm{ox}}} + U_{\mathrm{gs}} - U_{\mathrm{THR}}\right) \tag{3.2}$$

The formula reveals that the internal amplification g_q is dependent on the charge at the internal gate. However, this non-linear term can be neglected for typical operational parameters. This model has been confirmed in [14] qualitatively, but Rummel points out that not all effects are taken into account. A higher gate potential restricts the charge transport to a region close to the Si-Si:O2 interface. The result is a decreased mobility μ_p of the holes and thus smaller values for g_{m} and g_q than expected. A further necessary correction concerns the factor f. A change of the gate voltage results in a change of the potential distribution in the transistor and thus a spacial shift of the internal gate. Hence, f is not a constant.

Typical values for g_q obtained in previous measurements are in the range of 320 to 655 pA/e^- depending on the details of the DEPFET layout[5]. This means that 1 electron collected at the internal gate of the DEPFET causes a change in the drain current of about 0.5 nA. For comparison, a minimum ionising particle creates about 23000 electrons in a silicon sensor of a 300 µm thickness [11].

3.1.3. Charge removal: Clear and Clear Gate

After the readout, the accumulated charge must be removed from the internal gate. This achieved by applying a high voltage to the clear contact (see fig 3.4). During charge collection and readout, this contact has to be insulated from the rest of the bulk to prevent charge losses. For this reason, it is surrounded by a p-region,

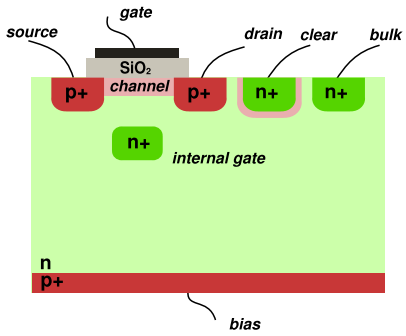

Figure 3.4.: DEPFET sensor with clear contact. (Colour key: light green = n-type silicon, dark green = highly doped n-type silicon, light red = p-type silicon, dark red = highly doped p-type silicon, light grey = silicon oxide)

which can be passed if the applied voltage is just high enough (punch trough effect [6]).

The clear process is improved by a further MOS structure, namely, the clear gate. In the original DEPFET design the clear gate was switched on when the clear pulse was applied, and each row of the DEPFET matrix had its own clear gate contact. This rather complicated design was replaced by a common clear gate (CCG). The CCG is kept at constant potential during the complete readout.

A careful choice of the clear high/low and the CCG potential is crucial for the correct operation of the DEPFET. Known undesirable effects are charges losses due to continuous clear, incomplete clearing, back injection of electrons from the clear contact or parasitic steering of the MOSFET channel [14].

3.2. DEPFET matrices

3.2.1. General properties

Originally created as a device for X-ray spectroscopy, the DEPFET detector was adapted to fulfil requirements of a vertex detector for high energy physics. The technology was changed from JFET to MOSFET to achieve smaller pixel sizes (technology limit $20 \times 20\ (\mu\mathrm{m})^2$) and a double/quadruple pixel structure introduced to speed up the readout [18].

The readout of DEPFET matrices is accomplished in "rolling shutter mode". In this mode a matrix row (or a group of rows) with common gate contact is selected and all pixels of this row are read out in parallel. Fig. 3.5 illustrates the process. The whole matrix is read out by switching on and reading out all rows subsequently.

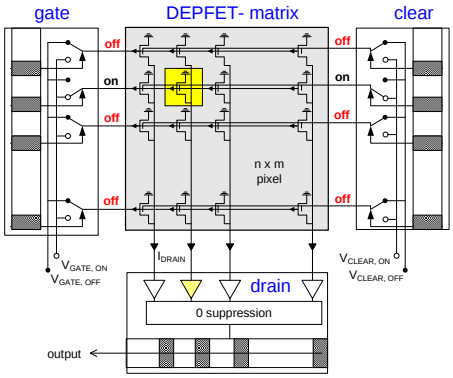

Figure 3.5.: Schematic of a DEPFET matrix [18]

Various iterations of DEPFET productions are available designated PXD4, PXD5 etc. Matrices of the PXD5 production with a pixel size of $32 \times 24(\,\mu\text{m})^2$ were used for the purpose of this thesis. They show the so called ILC[2] layout and the thickness of the silicon is 450 µm. The PXD5 pixels are arranged in a double pixel structure, which allow parallel readout of two matrix rows. The number of necessary ADCs is therefore twice the number of matrix columns.

The Belle II experiment will use pixel sizes of 56 µm × 50 µm and 77 µm × 50 µm [5]. The pixels are grouped in quadruple pixels. A special technology developed at MPI[3] HLL[4] allows the silicon to be thinned down to 50 µm maintaining a support frame of the full thickness of the silicon [19]. The prototype production for Belle II (PXD6) was thinned down to a thickness of 50 µm and was available at the beginning of 2011. Simulations proved that a sensor thickness of 75 µm is more suitable for the Belle II vertex detector and this thickness was chosen for the final design (PXD7).

Generally, thicker silicon means that crossing particles create more charge and the signal-to-noise ratio is improved. On the other hand, thicker silicon increases multiple scattering and the vertexing capability of the detector is deteriorated. The chosen thickness of 75 µm strikes a balance between these two effects.

Due to the high luminosity in the Belle II experiment, an elevated number of pixels will be firing at the same time. The maximum allowable occupancy (fraction of hit pixels) is in the order of 1 %. The planned readout speed for the whole matrix is of 20 µs [5].

[2]International Linear Collider
[3]Max Planck Institute
[4]Semiconductor laboratory (Halbleiterlabor)

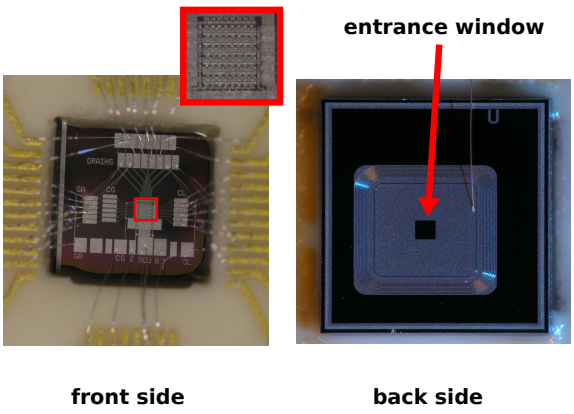

Figure 3.6.: The mini matrix under the microscope (photo: J. Scheirich)

The high readout speed of the system does not allow the full exploitation of the low noise performance of the DEPFET detector. In order to investigate the increase of noise caused by radiation and allow a choice between different pixel layouts, a low noise test system is necessary. Measurements with single pixel structures can be optimised to exhibit noise values down to 1.6 e^-, but effects such as charge sharing between neighbouring pixels are missing. This gap should be bridged by mini matrices.

3.2.2. Mini matrices

Mini matrices are dedicated test structures of several tens of pixels. The layout of the transistors is exactly the same as for the big DEPFET matrices. The PXD5 production contains mini matrices of 8×12 pixels, but only 4×12 pixels are read out with the mini matrix setup. Fig. 3.6 shows the front side with the wire bonds to the ceramics socket and the back side with the entrance window.

The PXD6 production has not yet been tested with the mini matrix setup. It contains 4 mini matrices grouped on a common symmetrical socket which allows the selection of one of the matrices for testing by rotating the socket. Adaptors to the mini matrix setup for PXD6 mini matrices are under construction.

3.3. DEPFET compared to other pixel detectors

Besides the DEPFET sensor, other concepts for semiconductor pixel sensors have been developed. A selection of these devices with their advantages and disadvantages is presented below, and the particular features of the DEPFET are pointed out.

Table 3.1.: Differences between the mini and large matrices [20], [18], [5]

Mini matrix (PXD 5)	CURO readout (PXD 5)	Belle II matrix (PXD 7)
8×12 pixels	64×128 pixels	250×800
24 µs/frame	947 µs/frame	20 µs/frame
double pixels		quadruple pixels
4 µs/pixel	0.32 µs/pixel	0.1 µs/pixel
flexible readout sequence	correlated double sampling	correlated double sampling, single sampling
clear: 225 ns	clear: 20 ns	clear: 225 ns
unthinned, 450 µm		thinned, 75 µm

3.3.1. Hybrid sensors

Pixel detectors contain a large number of pixels in a very small area. This poses a particular problem with respect to the connection to readout electronics. The common solution is to connect dedicated readout chips via bump bonding directly to the sensor. In this technique small metal droplets are positioned on the contacts of the sensor, the readout chip with the corresponding contacts is aligned and then the connection is made by applying pressure and heat. Detectors built by this method are called *hybrid modules*.

Charge coupled devices (*CCD*) are well known from their application in digital cameras. The collected charge is transferred from one pixel to the next by periodical potential changes until the readout contacts at the end of the matrix are reached. Disadvantages are the weak radiation hardness, long readout cycles and the fact that the matrix stays sensitive to new hits during the readout. Nevertheless, this sensor type has already been used in high energy physics and is being considered for use in the ILC vertex detector [11].

Radiation hardness is a big issue for semiconductor sensors in high energy physics. Besides the optimisation of the bulk material (Czochralski, oxygen enriched silicon etc.), a new concept has been proposed: *3D pixels*. Vertical columns of $5 \ldots 15\,\mu\text{m}$ in diameter are etched in the bulk silicon and filled with n- and p-type doped material. The distance between this columns can be as small as $30\,\mu\text{m}$, resulting in small depletion voltages and reduced drift lengths [21].

Currently, hybrid modules are the only option for the high radiation background at LHC. Electron-positron colliders with less background such as SuperKEKB or the future ILC allow a larger variety of sensors.

3.3.2. Monolithic devices

The major disadvantage of hybrid modules is the additional material introduced to the sensitive area by the readout chips and the bump bonds. The consequence is an increase of multiple scattering and a deterioration of the position resolution of the detector system. The dream of detector designers is to integrate sensor and readout electronics on the same wafer and build so called *monolithic devices*.

Monolithic active pixel sensors (*MAPS*) are produced in CMOS technology and contain, in the simplest version 3 transistors, one to select the pixel for readout, one to amplify the signal and one for reset. In contrast to other detector layouts, the sensitive volume is undepleted, which means that charge is collected by diffusion only [22]. Sensors of recent digital cameras are of this type and a whole list of candidates for the ILC vertex detector follows this approach. A further example is

the MIMOSA sensor, which is a part of the EUDET telescope used for DEPFET test beams [23].

Even more sophisticated detectors become possible with the silicon-on-insulator (*SOI*) technology. Here, two silicon wafers are bound directly together. One wafer provides the sensitive volume, the other contains CMOS circuits. Intelligent data handling processors, providing functionality such as sparse data scan, pipelining, clustering etc., can be integrated directly into the pixels. This sensor type might replace the DEPFET vertex detector in Belle II after 5 years of operation when the luminosity of the accelerator reaches its design value [5].

3.3.3. Characterisation and special features of the DEPFET

The DEPFET detector can be classified as a semi-monolithic device because of its integrated MOSFET transistor as first stage of signal amplification. However, the readout and data processing is handled by supplementary chips.

The built-in amplification leads to an excellent *noise performance*. The lowest noise measured with a DEPFET device was 1.6 e^- [17]. However, it has to be admitted that such measurements are performed with specially designed round single pixel structures [6]. The fast readout of a big PXD5 DEPFET matrix showed noise in the order of 300 e^- [5].

The outstanding noise performance of the DEPFET permits the *thinning* of the devices down to 50 µm maintaining a sufficient signal-to-noise ratio [24]. This is a major advantage for the application in a vertex detector where the material budget has to be kept as small as possible.

The collected charge can be stored at the internal gate of the DEPFET for long periods of time, until it is cleared by a clear pulse. This allows a *repetitive non destructive readout* (RNDR) of the matrix. However, this feature is not useful for applications which require fast readout.

In terms of radiation hardness the weak point of the DEPFET are the MOS structures because irreversible ionisation and interface states occur in the oxide layer [5].

4. The mini matrix setup

The details of the mini matrix setup are presented. After a short overview of the electronics, the emphasis will be on the software for DAQ and analysis.

4.1. Electronics

The system can be divided in two parts: The generation of steering signals and the readout. The steering electronics consists of a sequencer unit and a set of switching circuits, the readout of a set of preamplifiers and ADCs. Both parts are tuned to fulfil the low noise requirements. A more detailed description of the setup will be available in reference [25]. The measurements are controlled by a computer with the Windows XP operating system.

Currently two versions of the main board exist. The modification between the first and second version mainly concerns the switching circuits. In this thesis measurements with the second version are presented.

The operation voltages of the mini matrix were chosen in accordance with the CURO readout system [18], which was designed for PXD4/PXD5 DEPFET matrices with the same pixel layout, but a higher number of pixels. The operation voltages are:

source	0 V
drain	−5 V
bulk	3 V
CCG	−5 V
clear low	−3.8 V
clear high	13 V
gate low	−4 V
gate high	6 V
depletion voltage	−160 V

4.1.1. Generation of the steering signals

The XBoard [26], a programmable sequencer unit developed by A. Wassatsch at MPI HLL, is responsible for the correct timing of the readout. The XBoard supplies the timing of the steering signals, which select the rows of the matrix for readout

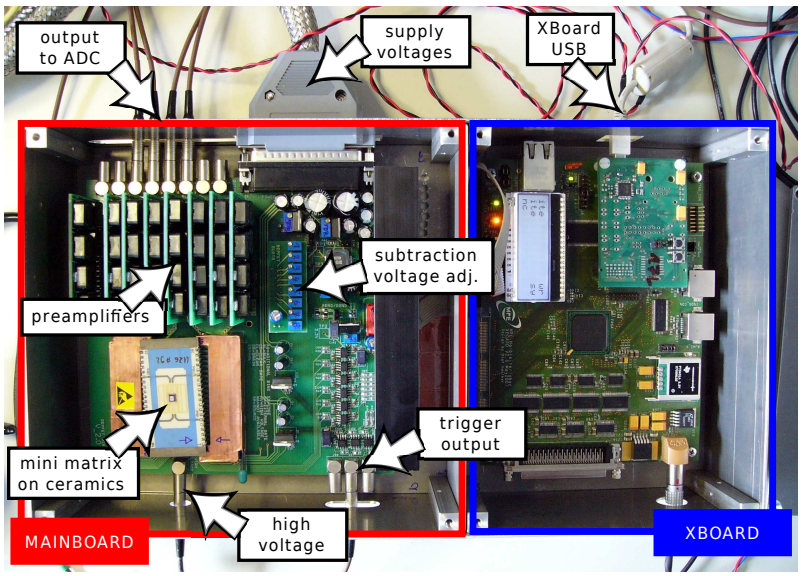

Figure 4.1.: The mini matrix setup (photo: J. Scheirich)

and clear the pixels. A detailed discussion of the readout sequence follows in the DAQ section of this chapter. The XBoard is built on an separate PCB and can be programmed from the computer via a USB connection.

Figure 4.2 illustrates the switching circuit for an individual gate line of the mini matrix (the switchers for the clear pulses are built the same way). An ADuM1100 provides a galvanic isolation between the XBoard and the main board. It works on the principle of a transformer enhanced by a digital circuit. The secondary side is floating and powered directly from the gate voltage. An internal power supply delivers $V_{\mathrm{gate5V}} = 5\,\mathrm{V}$ and $V_{\mathrm{gateREF}} = 2.5\,\mathrm{V}$ with relation to the V_{gateLOW} voltage. Depending on whether the level at the input of the circuit is high or low, there is positive or negative potential with relation to V_{gateREF} at the input of the operational amplifier AD8066, which switches the voltage at the output accordingly between V_{gateLOW} and V_{gate}. The signal shape obtained by this solution is presented in chapter 5.

Fluctuations of the voltage at the external gate are directly visible in the drain current. Differences of the gate voltage between the individual gates result in a offset of the drain current between whole pixel rows. The clear voltage is less critical provided that the clear is complete. The clear gate in this setup is at constant potential and does not have to be switched.

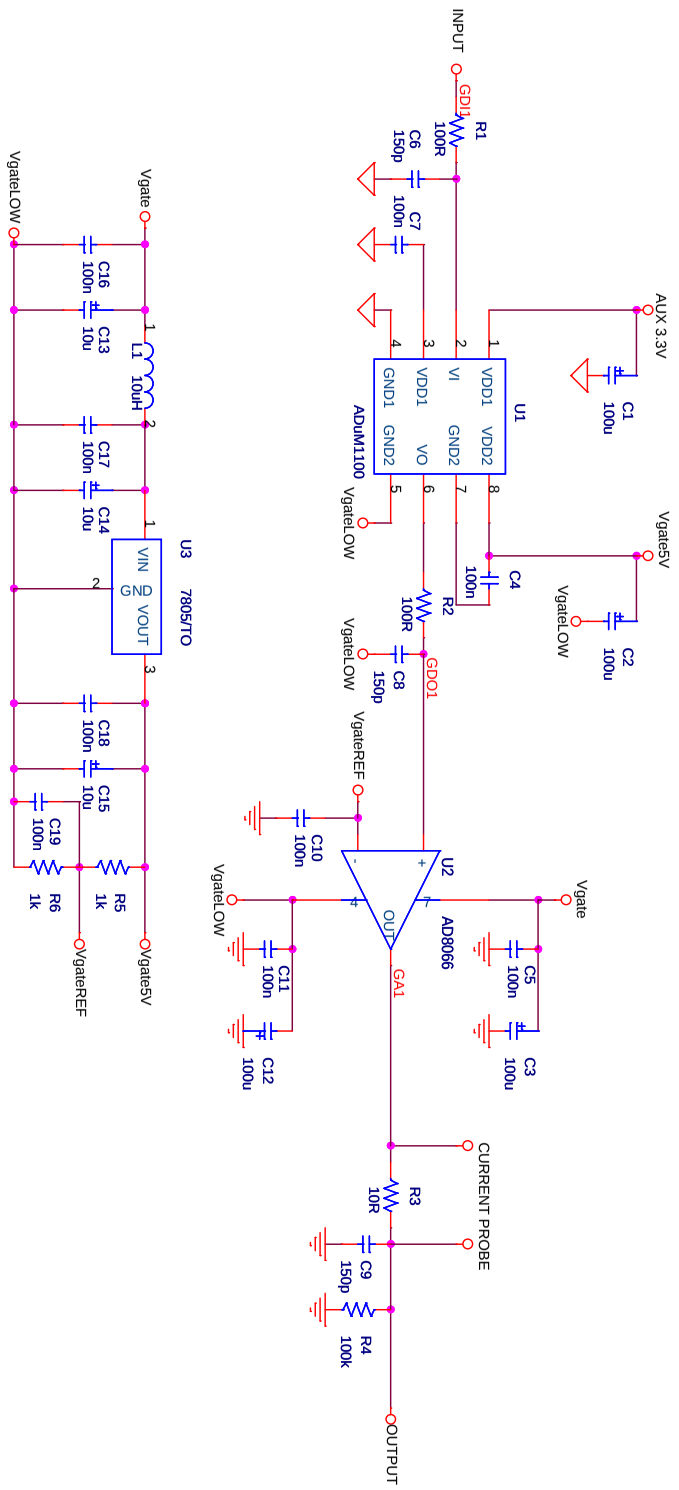

Figure 4.2.: Switcher circuit for one gate channel (layout: J. Scheirich)

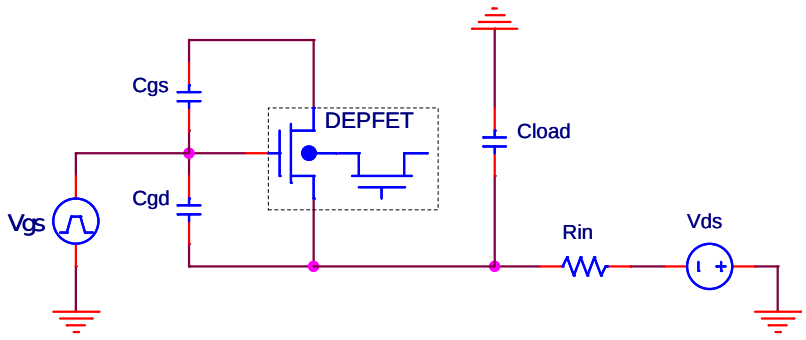

Figure 4.3.: Drain readout configuration (drawing: J. Scheirich)

4.1.2. Signal amplification and digitisation

The preamplifier

The first amplification stage is provided by the built-in MOSFET transistor of the DEPFET pixel. This first amplifier sets the limit to the achievable signal-to-noise ratio of the system [14]. In the ideal case all further amplification stages do not add more noise to the measurement.

Principally, two different readout configurations are possible for a DEPFET pixel: source follower and drain readout. Since the settling time of the source follower is far too long for applications in high energy physics, the drain readout shown in Figure 4.3 is the option of choice [27]. Gate and source of the DEPFET pixel are kept at constant potential and the drain potential is fixed via a transimpedance amplifier. Changes of the collected charge at the internal are reflected in the source-to-drain current [14]:

$$\Delta I_{\mathrm{ds}} = \Delta q \cdot g_{\mathrm{q}} \tag{4.1}$$

The transimpedance amplifier U1 converts the source-to-drain current into a voltage which is then further amplified by the operational amplifier U2 (see Fig. 4.4). The feedback of the amplifiers has to be adjusted carefully to ensure stable operation of the system. In early measurements, a distortion of the output signal was present, which could be eliminated by correcting C1, R10 and R12. The old, unmodified version is given for reference in Appendix B, Figure B.3. It also contains a differential driver for long-distance transmission of the output signal, which has now become obsolete (cable length $< 2\,\mathrm{m}$).

The acquisition card

The output signal of the preamplifiers is digitised by a 14-bits GaGe PCI Octopus card. Measurements were performed at MPI HLL with an 8 channel card, and with

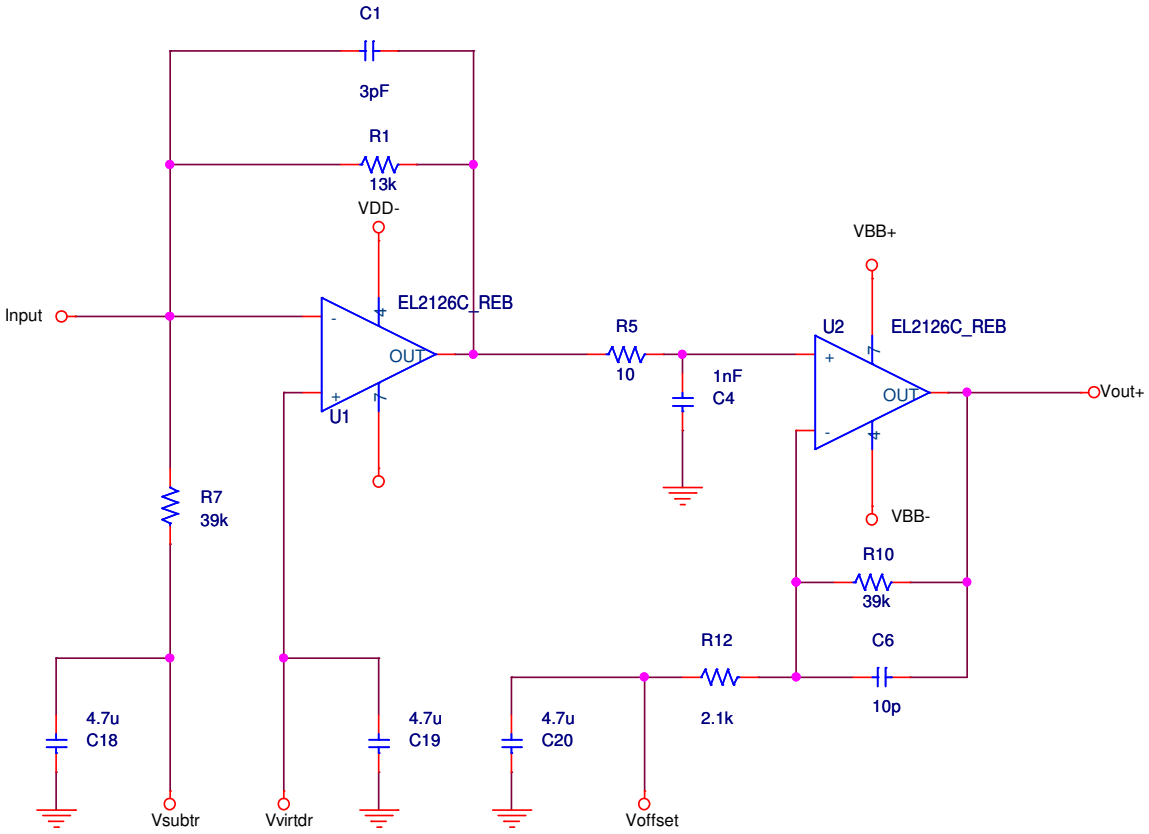

Figure 4.4.: Circuit of amplifier for the drain current (layout: J. Scheirich)

a 4 channel card in Prague. The maximum sampling rate is 125 MS/s. The DAQ software uses the provided API for C.

4.2. Overview of the software package

The MiMaTools software package can be divided into several independent parts as illustrated in Figure 4.5.

The programs for the *hardware control* are written in Microsoft Visual C++ and run on a computer with the Windows XP operating system. They allow for communication with the GaGe scope card, the XBoard, the motor stage and the programmable power supplies. All required parameters are supplied in configuration files or as command line argument. Once compiled, these programs do not require any further modification.

The steering of the *DAQ* is accomplished by a set of python scripts. They call the hardware control programs and write the log files.

The output of a measurement are the raw data saved in ASCII text files and one or more log files. The complete configuration files are copied into the log file. This log file is evaluated in the analysis to extract the conditions of the measurement. The complete information relating to the measurement is available, and it is possible to run the analysis on a different computer or exchange data between different institutions.

The *analysis* is based on ROOT [28] and therefore runs on computers with Windows or Linux operating system. Basic functionality such as reading/saving of data files, signal evaluation or clustering, is provided by a number of *generic analysis classes* especially developed for the mini matrix setup. The *analysis macros* carry out the major steps of the analysis while the details are hidden in the analysis classes.

The following sections summarise the DAQ and analysis. More details are given in Appendix B.2 and the numerous comments in the source code.

4.3. DAQ

The core of each measurement is a python steering script, which then calls external programs to perform tasks such as configuring the XBoard, collecting data with the ADC or moving the motor stage. The measurement is organised in a loop as depicted in Figure 4.6 consisting of 1. steering of additional hardware, 2. data collecting, 3. data saving.

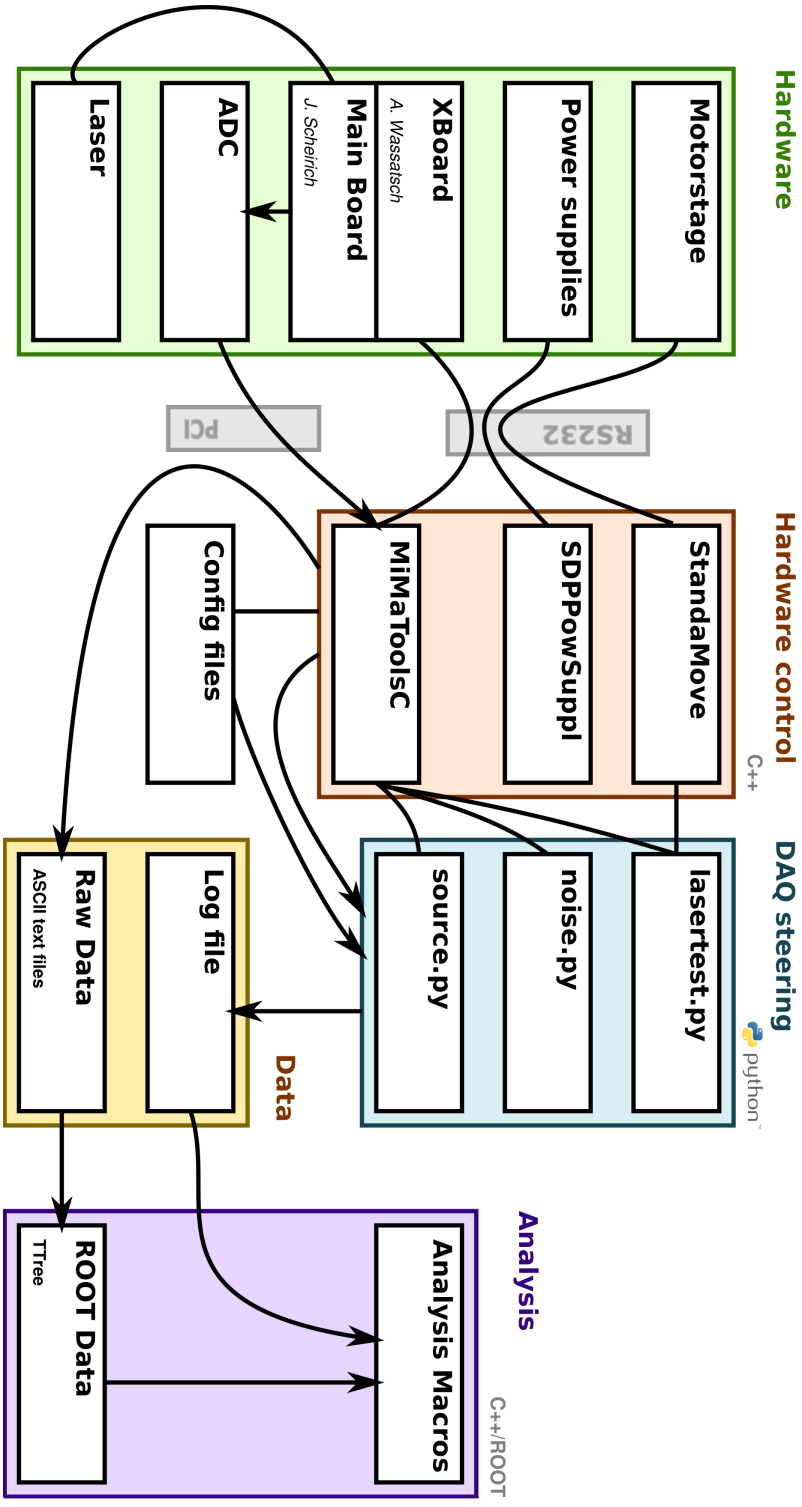

Figure 4.5.: Overview of the MiMaTools software package

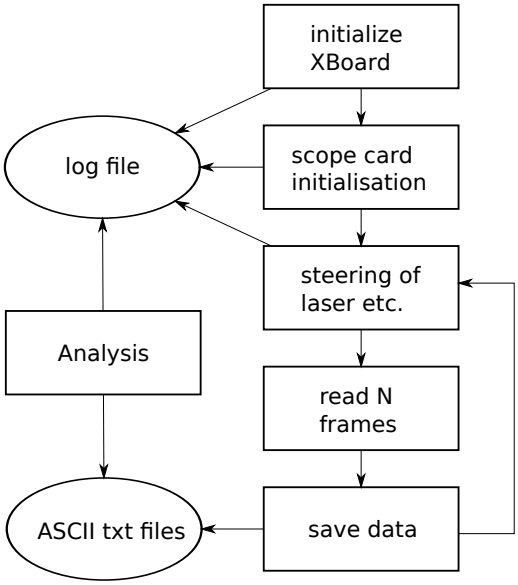

Figure 4.6.: Overview of the DAQ

The measurement is configured through parameters directly supplied within the steering script. A set of configuration files contains common information for different measurements. For each run all parameters and configuration files are saved in the log file.

4.3.1. Configuration of the readout sequence

There is not only one way to read out a DEPFET matrix. A good overview over the different readout strategies is given in reference [14]. The mini matrix setup is not limited to a specific mode due to its flexible sequencer unit. Furthermore, an essential difference to other DEPFET readout systems is that the mini matrix setup acquires the drain current continuously, which means that the raw data is saved as a complete scope signal and no restrictive preprocessing is applied. Hence, it can be decided later in the analysis which parts of the signal are evaluated.

The sequence is uploaded to the XBoard at the beginning of the measurement or the running sequence can be maintained. The system has to be powered down during the (re-)configuration of the XBoard because random signals appear at its output and could destroy the setup. The sequence is defined individually for each channel in a number of steps using commands such as "switch channel i on/off for n time ticks" or "jump to step number s" [26]. One time tick lasts 7.5 ns corresponding to a clock rate of 133 MHz.

The standard sequence run by the XBoard is depicted in Figure 4.7. Unless specified otherwise, the measurements are performed with this standard sequence.

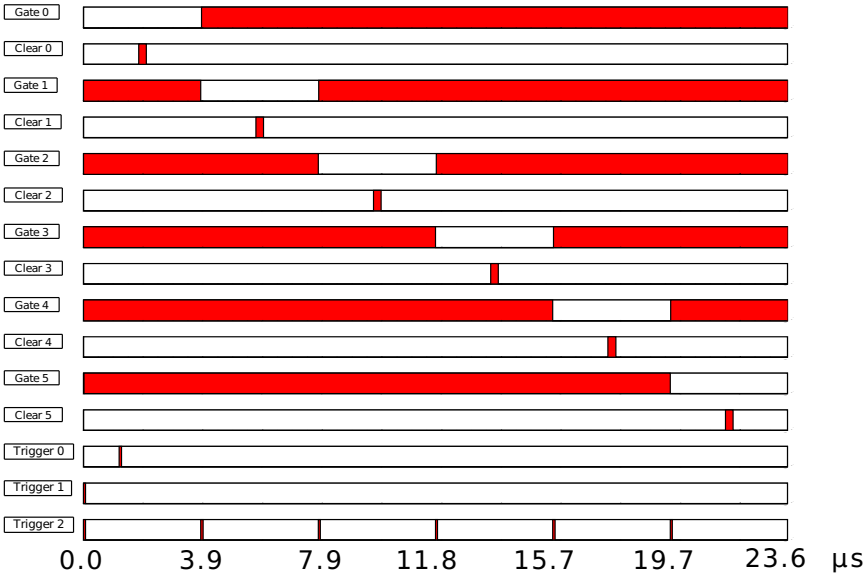

Figure 4.7.: Standard XBoard sequence, length of 1 cycle 23.58 µs

White areas correspond to low potential and red areas to high potential. The rows of the matrix are switched on subsequently by setting the gate to the low potential. The readout of the whole matrix takes 23.58 µs. The rise and fall time of the gate switching circuits has to be compensated by an overlap of 22.5 ns between consecutive gates (the overlap is not visible in the picture). While the gate is open, the internal gate is cleared by applying a pulse of 255 ns at the clear contact of the same row. Hence, the drain current of the pixel is measured first with the integrated charge at the internal gate and then with an empty internal gate.

The creation of a sequence is not trivial, because the maximum number of time ticks per step is limited to 1024 and the gate steering pulses have to overlap to compensate the rise/fall time of the switchers. Therefore, a ROOT macro was developed to create sequences of custom length.

4.3.2. Digitisation

The voltage at the output of the preamplifiers are acquired continuously by a GaGe scope PC card. Trigger channel 0 as shown in Figure 4.7 is used to trigger the data acquisition. It can be seen, that the drain current flowing while the first gate is open is not acquired completely; a part at the beginning is missing. This corresponds to processing time of the scope card which is unfortunately necessary between two triggers.

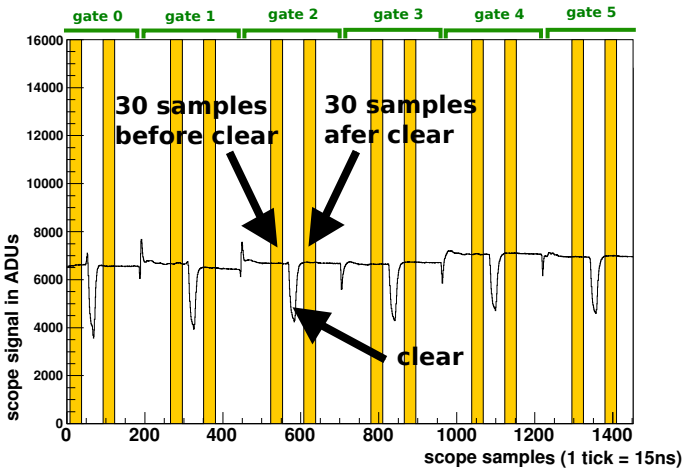

Figure 4.8.: Evaluation and averaging of the raw scope signal

4.3.3. Raw data format

The structure of the raw data is described in terms of a number of substructures: The smallest unit is a *sample* (given in ADU) signifying the result of the digitisation of the output voltage of one preamplifier at a given moment. When the scope card is ready and a trigger is received, a predefined number of samples is acquired in each channel. This is an *event* characterised by an event number and a channel number. A *frame* is the group of all events acquired simultaneously by the 8 channels of the scope card after a trigger. A frame is characterised by the event number and corresponds to the full readout of the matrix. The scope card is able to collect not only one frame, but a whole series of frames one after the other. This series of frames will be referred to as *bunch*.

After the acquisition of a bunch, the scope card stops and waits for the DAQ software to transfer the binary data from the internal memory of the card to the memory of the computer. Then the binary data is converted to numbers and stored in a human readable ASCII text file. Each bunch is stored in its own text file. In the whole process of data acquisition, this step is the most time consuming and represents a veritable bottle-neck. Writing the binary data directly to the disk and postponing its processing to the analysis might be preferable in future releases of the software.

Figure 4.8 shows an example of an event. The signal contains the information of 6 pixels before and after clear. It can be seen that the signal of the first pixel before clear is not entirely acquired as mentioned above.

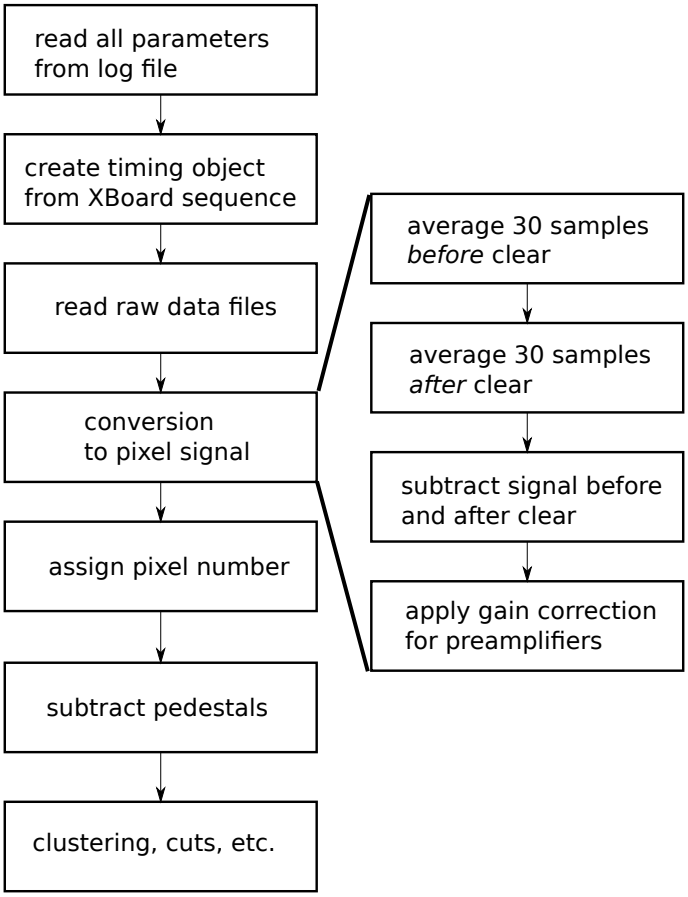

Figure 4.9.: Overview of the Analysis

The number and size of the raw data files ranges from a couple of files with tens of kB each to several thousands files with a size of hundreds of MB, depending on the type measurement. Since the large number of ASCII text files creates a large data overhead and slows down further data processing, the text files are converted into the ROOT TTree format.

4.4. Analysis

The analysis is performed by subsequent execution of a number of ROOT macros. Figure 4.9 shows a flow chart diagram. The following sections discuss the individual steps.

4.4.1. Averaging

The first step in analysis is to extract the pixel information from the raw data TTree. To improve the accuracy of the current measurement the average $\bar{q}_{\mathrm{BC}}$ is

taken over several samples, typically $n_{\mathrm{AdcCounts}} = 30$. The yellow areas in Figure 4.8 contain these 30 samples. The standard error $\sigma(\bar{q}_{\mathrm{BC/AC}})$ of the average is given by:

$$\sigma(\bar{q}_{\mathrm{BC/AC}}) = \sigma(q_{\mathrm{BC/AC}})/\sqrt{n_{\mathrm{AdcCounts}}} \tag{4.2}$$

4.4.2. Correlated Double Sampling

The pixel signal is calculated in this thesis using correlated double sampling. The data acquired by a "read-clear-read" sequence contains information of both the signal current $\bar{q}_{\mathrm{BC}}$ (before the clear pulse) and the pedestal current $\bar{q}_{\mathrm{AC}}$ (after the clear pulse). The first sample corresponds to the collected charge plus a pedestal. The second sample is the pedestal current after clearing the internal gate. It is therefore possible to correct the signal current for the fluctuating pedestal current by means of a simple subtraction:

$$\bar{q} = \bar{q}_{\mathrm{BC}} - \bar{q}_{\mathrm{AC}} \tag{4.3}$$

The full error of the pixel signal is given by:

$$\sigma(\bar{q}) = \sqrt{\sigma(\bar{q}_{\mathrm{BC}})^2 + \sigma(\bar{q}_{\mathrm{AC}})^2} \tag{4.4}$$

The drawbacks of this solution are a slower readout (no problem for the mini matrix setup) and the sensitivity to incomplete clearing [14].

In Figure 4.8 it is demonstrated how the correlated double sampling is applied to the acquired data. In order to find the correct sampling position, information about the timing is needed, i.e. which pixel row is active at what time and when exactly the internal gates of the pixels are cleared. This information can be drawn from the log file containing the sequence of the XBoard. This, however, brings a first uncertainty into play: the timing of the sequencer and the acquisition card have to be synchronised. This requires exact knowledge concerning both the sampling rates and the offset between the opening of gate 0 and the start of the acquisition Any error in this respect results in the evaluation of slightly different parts of the scope signal for the different pixels. The regions to be evaluated are defined manually by adjusting the sample rate, the offset and the number of averaged samples. A visual check is performed using the plot in Figure 4.8 whereby the evaluated regions are depicted in yellow. The yellow areas are also referred to as *soft trigger*.

4.4.3. Gain correction

Tolerances of the electrical components of the preamplifiers are compensated by applying a gain correction to the obtained pixel signal $\bar{q}$. The gain g_{i} of all n

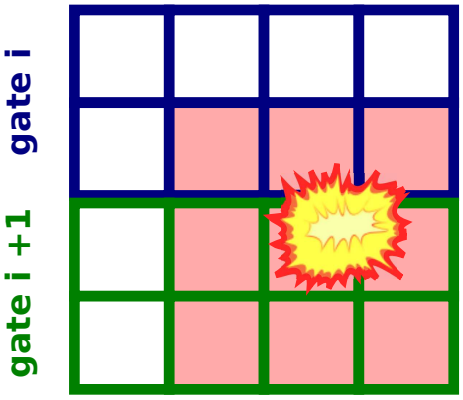

Figure 4.10.: Hit with 3×3 cluster

amplifier modules i was measured (cf. chapter 5.2.2). The final pixel signal for a pixel connected to drain channel i is then calculated by:

$$\bar{q}_{\text{final}} = \bar{q} \, \frac{g_{\text{i}}}{\frac{1}{n} \sum_{i=0}^{7} g_{\text{i}}} \tag{4.5}$$

4.4.4. Pedestal subtraction

The measurements in the next chapter show that the correlated double sampling works quite well. Nevertheless, charge is accumulated in the internal gate even without an external source due to the leakage current. This charge results in a pixel signal[1] different from zero, which will be referred to as *pedestal*. This definition of pedestal should not be confused with the *pedestal current* which is the current measured after the clear pulse.

The pedestals were found to be different for every individual pixel, but stay constant in long term measurements. They are calculated by the median[2] of 1000 frames taken at the beginning of the measurement and then subtracted.

4.4.5. Common mode correction

A distortion in the signal of a gate switcher has the same effect in all pixels which are connected to the responsible switcher. Similarly, temporal variations in the preamplifier-ADC chain affect all attributed pixels. These fluctuations can be determined by analysing the signal of groups of pixels. If the average signal of the group goes up or down, this offset is called *common mode*. In this thesis the average is calculated by the median.

[1] difference of drain current before and after clear
[2] the result is then less influenced by outliers

The data can be in principle corrected by subtracting the common mode. In the mini matrix system this correction is restricted to empty frames due to the low number of pixels (a matrix double row consists of only 8 pixels!). If a pixel is hit, the neighbouring pixels might also contain some charge. The exclusion of these neighbouring pixels leads to an insufficient number of pixels for a reasonable common mode correction as illustrated in Figure 4.10.

4.4.6. Clustering, general approach

When a particle passes the detector, the charge is generally collected not only in one pixel, but distributed over several pixels. This phenomenon of charge sharing is desirable as it improves the spatial resolution of the detector (η-algorithm [29]). All pixels hit by the same particle are grouped into a *cluster*. The cluster pixel with the highest signal is called *seed pixel*. It is common use to set the cut for seed pixels at 6σ, where σ is the pixel noise. Clustering algorithms usually start by looking for seed pixels. Then an area of 3×3 to 7×7 pixels around the seed pixel is examined and the cluster signal (= charge) is calculated by one of the following methods [18]:

- The signal of all pixels in the examined area is simply added up (fixed area).
- The pixels are ordered from the highest to the lowest signal and then the pixel signals are added up starting from the highest until a predefined number of pixels in the cluster (cluster size) is reached. The rest of the pixels are neglected. (fixed cluster size).
- The signal of hit pixels only, i.e. pixels above a certain threshold, is added up (variable cluster size).

Assuming that the noise of the individual pixels is statistically independent (which is not necessarily the case), a rough estimation for the error of the signal of a cluster of size N_{cluster} is given by:

$$\sigma(\text{cluster}) = \sqrt{\sum_{\text{clusterpixels}} \sigma(\text{pixel})^2} = \sqrt{N_{\text{cluster}} \cdot \sigma(\text{pixel})^2} = \sqrt{N_{\text{cluster}}} \cdot \sigma(\text{pixel}) \tag{4.6}$$

4.4.7. Clustering, special considerations for the mini matrix system

The cluster object in the mini matrix software is nothing else but a list of pixels ordered by their signal. As the number of pixels of the mini matrix is small, it can be assumed that only one cluster per frame is recorded or the conditions of the measurement can be changed in such a way that this assumption is true. At the

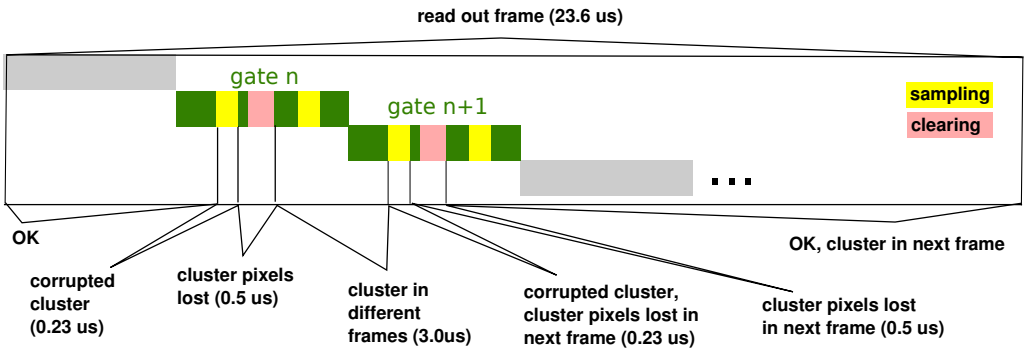

Figure 4.11.: Annotated part of the readout sequence in Figure 4.7. The 3×3 cluster from Figure 4.10 is read out in two steps.

beginning of the analysis, the entire mini matrix is taken as a cluster of fixed size (4×12). This very rough way of clustering can be improved by applying a number of cuts which result in more reasonable clusters according to the options presented above.

Initially, it is a good idea to reject all pixels below a *hit threshold* of 3σ noise. To select only frames containing a hit, the *seed threshold* is set to 6σ noise, so at least one pixel of the matrix has a signal significantly higher than noise.

Sometimes the matrix contains *noisy pixels*, that is pixels that very often and randomly show a signal above noise. These pixels can be excluded from the analysis as it is likely that they do not deliver any reliable information. Pixels located at the border of the readout area are not suitable as seed pixels, since a part of the cluster charge could be collected outside of the readout area and taking a *border pixel* as seed pixel would lead to an incomplete cluster.

After applying these restrictions, the cluster is a list of pixels with the seed pixel at first position. The next step is to limit the cluster to the neighbourhood of the seed pixel, that is to keep only pixels in the list which are geometrically direct *neighbours of the seed pixel* (3×3 cluster). The macro also allows to neighbours of neighbours to be included (5×5 cluster). If a threshold has been set previously, the cluster size is variable depending on how many pixels around the seed pixel are above the given threshold. Otherwise, all pixels around the seed pixel are considered as hit and clusters of fixed size are obtained

If the expected cluster size is known, it is useful to limit the *cluster size*, for example to allow only clusters with 2 to 6 pixels. This cut excludes clusters which do not fit in the given range.

Table 4.1.: Fraction of corrupted clusters

Problem	Fraction
Information in different frames	13 %
Corrupted pixel signal	2 %
Lost pixels	4 %
Total	19 %

One particularity of the mini matrix system is the slow readout time in order to ensure better noise properties. However, this implies a problem for measurements with radioactive sources. Let us consider a cluster of 3×3 pixels visualised in Figure 4.10. It is clear that such a cluster occupies two different gates of the mini matrix. As a consequence, the pixel signals of the clusters are not read out at once, but in two separate steps first gate i, then gate $i + 1$. Figure 4.11 illustrates this process. Problems can occur if the hit is produced during the readout of the corresponding cluster. Depending on the exact moment of the hit, this can lead to different outcomes. Hits during the signal sampling create corrupted pixel signals because not all samples contain the full signal, but in the analysis the pixel signal is calculated by taking the average over all samples. If the hit happens in the time after the signal sampling and before the end of the clear pulse, the pixel signals of this gate are lost for the cluster and the result is an incomplete cluster. Finally, a hit between the readout of the first gate and the readout of the second gate splits up the cluster into two subsequent frames. Table 4.1 summarises the problems mentioned and the corresponding fraction of affected hits.

These problems can be solved in a very elegant way simply by adding supplementary integration time before the readout (see Fig. 4.12). Then the time for the collection of correct events increases while the time of the incorrect event collection stays constant. Therefore, the probability of collecting incorrect clusters is reduced. Considering the case of a ten times longer integration time, the probability for corrupted clusters is lowered from 20% to only 2% which is acceptable. The increase of integration time naturally increases the probability of having an event in the frame, but if the event rate is low enough the condition of only one event per frame is still valid.

4.5. Conclusion

The author contributed to the mini matrix system with the development of a complete software package. It offers hardware control, DAQ steering and the complete analysis chain from raw data to final plots. Furthermore, a ROOT macro has been written for the creation of XBoard steering sequences. The controllable

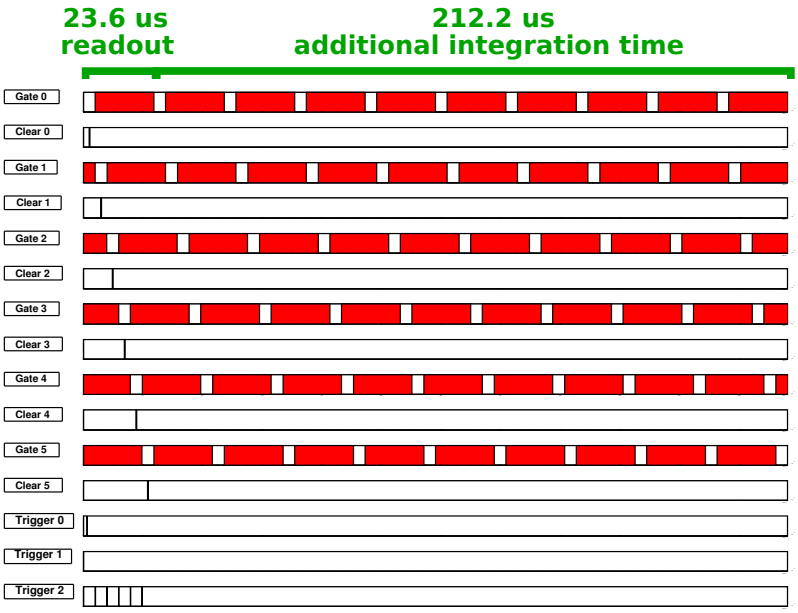

Figure 4.12.: Modified readout sequence with additional integration time. The input current of the preamplifiers has to be kept at constant level, so always one gate has to be opened. The simplest solution would be to keep gate 5 switched on after the readout. However, it is better not to give preference to one gate, but to open the gates one after another in the same way as during the readout, but of course no clear pulses are applied.

hardware comprises the XBoard sequencer unit, the GaGe scope card, the motor stage and the programmable power supplies. Amongst the analysis features to have been implemented are the preprocessing of the raw data, conversion from raw data to pixel data, and evaluation of noise, laser and source measurements. The results of all steps can be represented graphically.

A problem encountered in the software design was the high amount of raw data to be processed. The transfer of the data from the scope card memory to the memory of the DAQ PC proved to be a veritable bottleneck. Moreover, the large ASCII raw data files posed a challenge. Nevertheless, it was decided to keep the full scope signal in the raw data as a feature of the mini matrix setup and profit from the full flexibility in the later analysis. In future releases, saving the raw data to binary files may be an option in order to avoid the unwieldy ASCII text files. The prolonged integration time for source measurements increases the fraction of frames which contain a hit and consequently speeds up the measurement by reducing the number of empty frames transferred.

5. Measurements with the mini matrix setup

The measurements presented in this chapter show the performance of the system and the developed software for DAQ and analysis.

5.1. Signal shape of the switching circuit

The shape of the gate steering signals was digitised with a digital scope and then analysed in ROOT. Trigger 2 (cf. Fig. 4.7) was used to compare the precision of the timing. Figure 5.1(a) shows the good agreement between all gate steering signals. The interesting parts of the plot have been magnified: the stability of the voltage while the gate is switched on (Fig. 5.1(b)) and the rise/fall time (Fig. 5.1(c)).

The noise of the gate-on baseline can be roughly estimated with $\sigma = 7\,\mathrm{mV}$. The two spikes shortly before and after the 2 ms time-mark may be caused by the the switching of the clear signal. The actual noise of the gate signal at the mini matrix is expected to be less than measured here, because it is very likely that noise has been picked up in additional cables necessary for this measurement.

The rise/fall time from 10 to 90% of the gate-on has been measured as 35 ns (42 ns for 0 to 100%). This is in good agreement with the empirically tuned overlap of 22.5 ns between two consecutive gate steering signals.

5.2. Calibration of the preamplifiers

5.2.1. Linearity

The preamplifiers used differ slightly in their gain. These differences are taken into account by an individual calibration. A 10 Hz saw-tooth generator generates a variable input voltage U_{in}, and a current flows through a resistor R_{in} to the input of the preamplifier. U_{in} and the output voltage U_{out} of the preamplifier are measured simultaneously and then plotted.

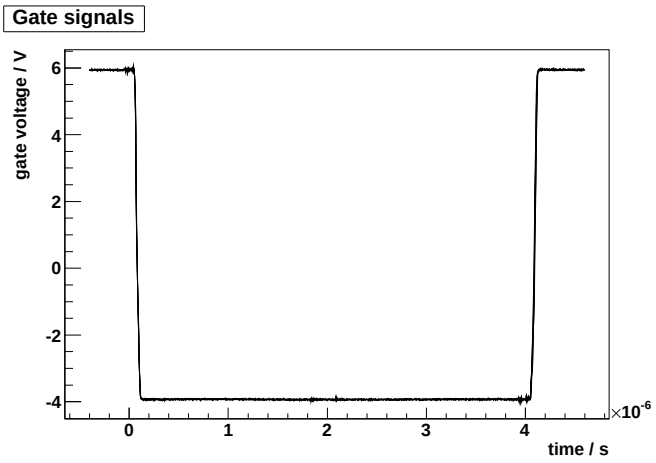

(a) all 6 gates

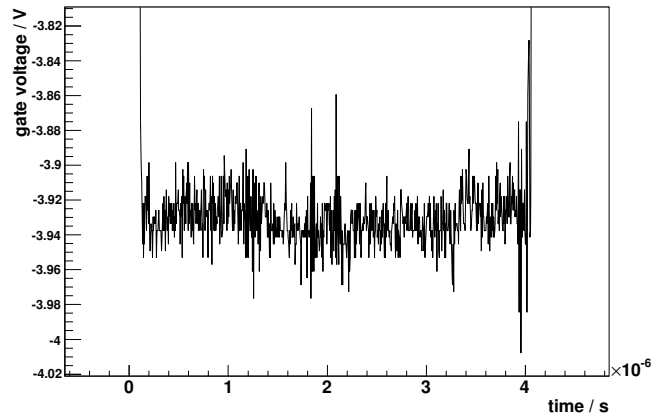

(b) zoom of gate 0

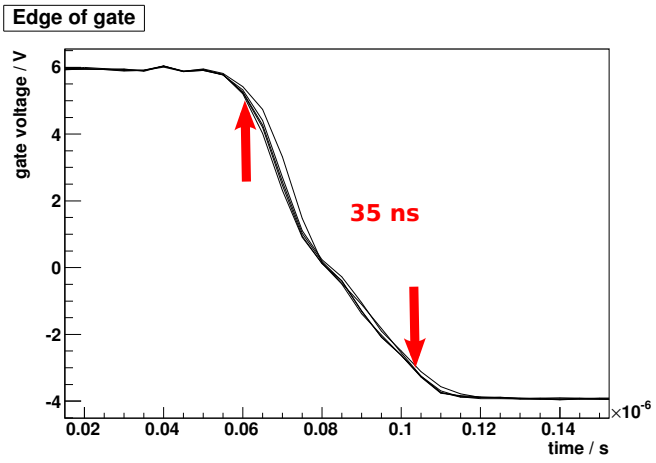

(c) edge of all 6 gates

Figure 5.1.: Shape of the gate steering signal

In addition, the subtraction voltage U_{subtr} and the virtual drain voltage U_{virtdr} (see Appendix B, Fig. B.2) are measured to convert the input voltage U_{in} into the input current I_{in} (except for an offset I_{offset}):

$$I_{\text{in}} = \frac{U_{\text{in}} - U_{\text{virtdr}}}{R_{\text{in}}} - \frac{U_{\text{virtdr}} - U_{\text{subtr}}}{R_7} + I_{\text{offset}} \tag{5.1}$$

An example plot is shown in Figure 5.2(a), and the full calibration in Appendix B, Figure B.5. The red line corresponds to a linear fit. The maximum deviation from the linear fit is 300 nA, while typical currents in measurements of mini matrices are in the order of thousands of nA. The residuals of the fit are shown in Figure 5.2(b). The fact that they are described by Gaussian distribution is a proof that the data of the fit is acceptable.

As the system is very sensitive to environmental effects, external sources of non-linearity (e.g. sampling noise of the scope card) can be eliminated by dividing the fit range in small intervals of a few samples, and subsequent averaging of the values within these intervals. It is important to stress that internal instabilities of the system may also be cancelled out by this average. Therefore, the evaluation of the measurement by this method reveals only the linearity of the system and not possible temporal instabilities. By this method, the maximum deviation from the linear fit is 15 nA.

In the first attempts of calibration, the residual distribution was a double Gaussian. A closer look at the data led to the discovery of a non-linearity of the preamplifier around zero. Figure 5.3 shows the deviation from the linear fit. The subtraction voltage V_{subtr} (cf. Fig. 4.4) was adjusted such that the range used in the measurement does not contain the non-linear region.

5.2.2. Gain of the preamplifiers

The slopes of the calibration curves correspond to the inverse gains of the individual preamplifiers ($g_i = \frac{\mathrm{d}V_{\text{out}}}{\mathrm{d}I_{\text{in}}}$). The axes were swapped because it better describes the situation in the mini matrix setup: the output voltage is measured in order to determine the input current.

The gain g varies from 1 V / 8265 nA to 1 V / 8201 nA (cf. Appendix B, Fig. B.5) and the scope card range used is 4 V / 16000 ADU. From this, the relation between input current and ADUs can be derived[1][2]:

$$\boxed{1\,\text{ADU} = 2.058 \pm 0.008\,\text{nA}}$$

[1] The first version of the preamplifiers contained a differential driver at the output which reduced the gain by about 50%. In measurements with the old amplifier 1 ADU corresponds to 4.2 nA.
[2] In the CURO readout (used in TB2009) 1 ADU corresponds to 7.7 nA [18].

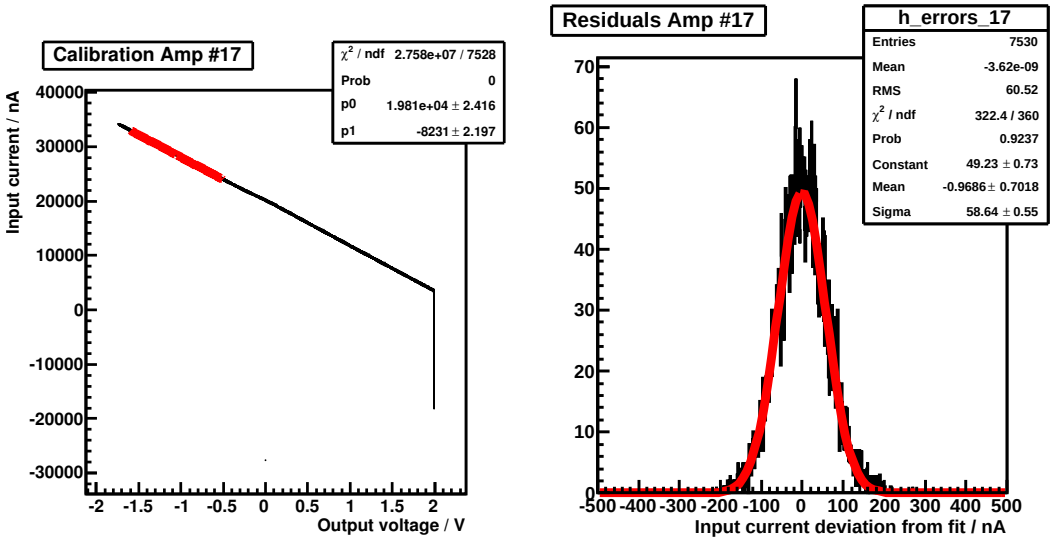

(a) linear fit (b) residuals

Figure 5.2.: Calibration of preamplifier number 17

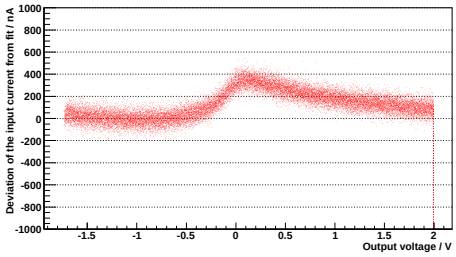

Figure 5.3.: Deviation from linear fit, non-linearity of the preamplifier around zero

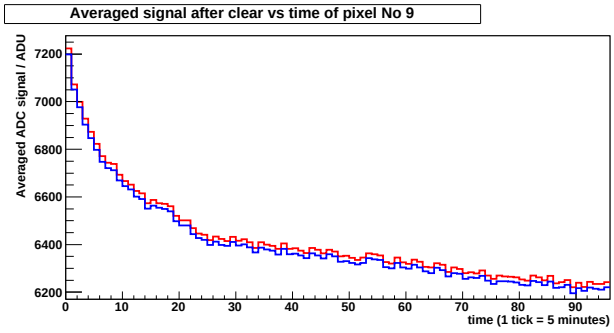

(a) Run 34, Stability of the drain current

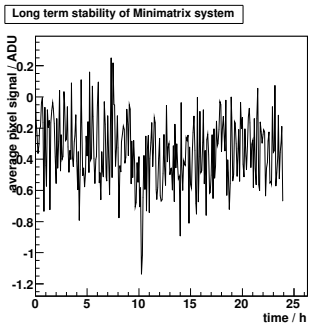

(b) Run 149, Pixel 25: Stability of the pedestal

Figure 5.4.: Long-term stability of the system

5.3. Stability

The stability measurements were performed in a black box with the first version of the amplifiers (Appendix B, Fig. B.3).

After switching on and initialising the cold system, the drain current changes drastically, as can be seen in Figure 5.4(a). The blue graph represents the evaluated drain current before the clear pulse, the red graph after the clear pulse. The most significant change of approximately 3400 nA occurs within the first two hours of the measurement. After 8 h the system is more or less stable.

Figure 5.4(b) shows the stability of the pedestal signal. Over a 24 h period, 100 frames were taken every 5 minutes, and the average pedestal signal of one pixel was calculated. The average pedestal signal remained stable.

This long term stability tests demonstrates the effectiveness of the correlated double sampling. Despite the immense change in the absolute value of the drain current during the measurement, the pixel signal, calculated as the difference between the current before and after clear, did not change. Nevertheless, attention has to be paid to the shift of the drain current in measurements which not only measure the pedestal signals, but also the collected charge in the internal gate: The operating point of preamplifiers could have moved to the non-linear region discovered in the previous section.

5.4. Signal shapes

The signal shape was investigated with a very slow sequence which keeps gate 3 open during the entire measurement, but subsequently clears all double rows (see

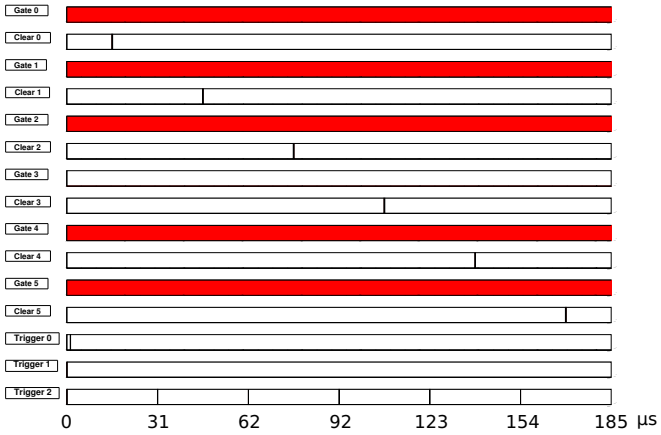

Figure 5.5.: Slow readout sequence, which keeps gate 3 open all the time, but clears all rows

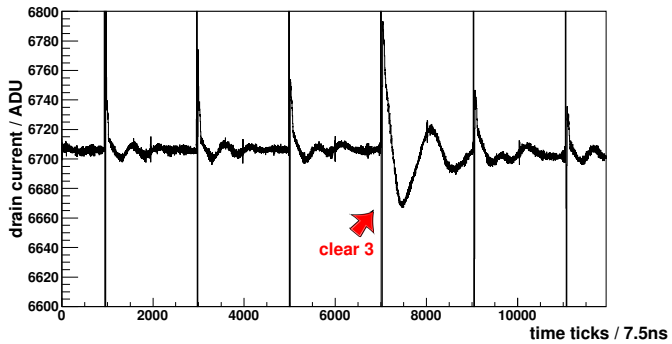

(a) old version of amplifiers (1 $ADU \approx 4\ nA$)

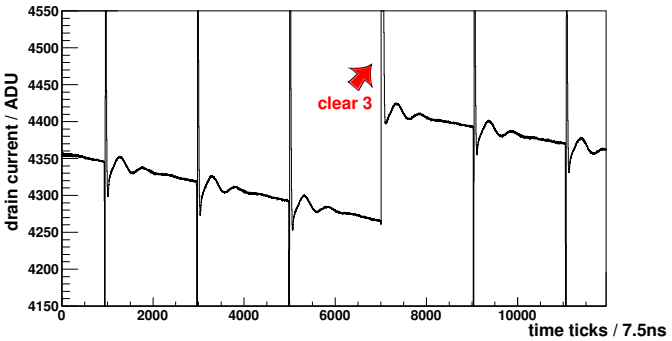

(b) new version of amplifiers (1 $ADU \approx 2\ nA$)

Figure 5.6.: Scope signal of a pixel connected to gate 3, very slow readout sequence

Fig. 5.5). The measurement was performed first with the old version of the amplifiers (cf. Appendix B, Fig. B.3) and then with the new version (cf. Appendix B, Fig. B.2).

The resulting shapes of the drain current are presented in Figure 5.6(a) and Figure 5.6(b), respectively. In the latter plot the drain current is inverted. Both plots show an average over 100 frames to eliminate sampling noise. The y-axes of the plots were adjusted such that they have the same drain current range. The high vertical spikes correspond to the clear pulses, which influence the drain current even if they are applied to a different double row.

The signal of the old amplifiers (Fig. 5.6(a)) is considerably distorted – the oscillation induced by the clear pulse has not damped down even after 31 µs when the next clear pulse is applied. Furthermore, one would expect to see an increasing drain current caused by the accumulation of charge at the internal gate due to the leakage current. However, the drain current remains constant. A possible explanation may be that there is an insufficient clear high voltage.

After a change in the amplifier feedback (cf. Appendix B, Fig. B.2) and an increase of the clear high voltage from 14 to 17$[V]$, the drain current is much less distorted (Fig. 5.6(b)). The expected increase due to the leakage current and a step after the clear of the corresponding gate 3 can be observed.

5.5. Pedestals

5.5.1. Measurement

The pedestal signal was measured by acquiring frames in a black box without a source which means several hundreds of "empty" frames were acquired. The pixel signals $\bar{q}_{\text{final}}$ (cf. eq. 4.5) of these frames are then averaged to obtain the pedestals.

5.5.2. Problem: Inhomogeneity of pedestals

The pedestal signal obtained is shown in Figure 5.7(b). The pedestal signal is not uniform but the differences are less than $\Delta I = 170\,\text{nA}$. A comparison with the pixel map (Appendix B, Fig. B.1) reveals that pixels of the same gate have similar pedestal signal (two consecutive rows are always connected to the same gate).

In generally, the pixels of the mini matrix all have the same layout, and significant changes in the material properties of the silicon are not expected in distances of hundreds of µm present in the mini matrix [30]. In other words, all pixels of a mini matrix should have the same properties.

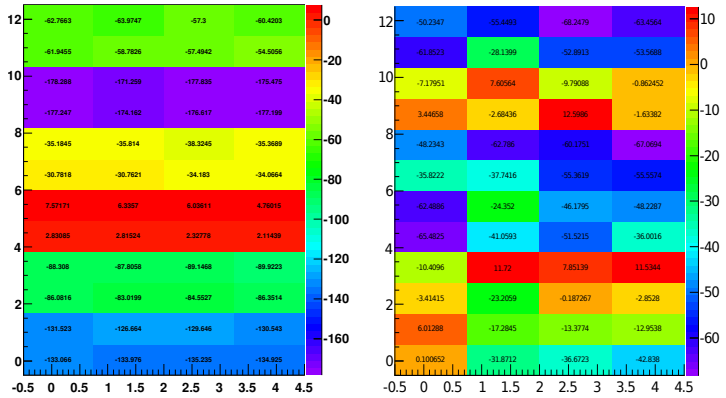

(a) old switchers, first version of amplifiers

(b) new switchers, second version of amplifiers

Figure 5.7.: Pedestal signal

The observed similarity of pedestals of the same gate could be caused by the shape of the gate steering signals because it directly influences the drain current of the pixels. Each gate has its own switching circuit, so any differences between the switchers are directly projected to the drain current.

5.5.3. Problem: Negative pedestals

Of greater concern are the negative values of the pedestal, because this means that a higher amount of charge should to be in the internal gate after the clear than before. A very simple explanation is that the clear pulse represents a considerable perturbation of the drain current and therefore influences the sensible preamplifiers as seen in the previous section on signal shapes. This is not necessarily a problem, if the signal after the clear is independent of the filling level of the internal gate, because then it is sufficient to measure the pedestal and subtract it from the signal. The stability test has demonstrated that the average pedestal stays constant even during a 24 h measurement. However, one has to consider that the pedestal is an averaged value. Possible variations of the pedestal could cause a loss of precision when a fixed pedestal is subtracted.

Future measurements with the mini matrix system should use readout sequences which provide longer relaxation times after the gate switching and particularly after the clear pulse.

5.6. Noise

Three different kinds of noise can be determined in the setup: the noise of the digitisation of the drain current, the common mode noise of groups of pixels, and

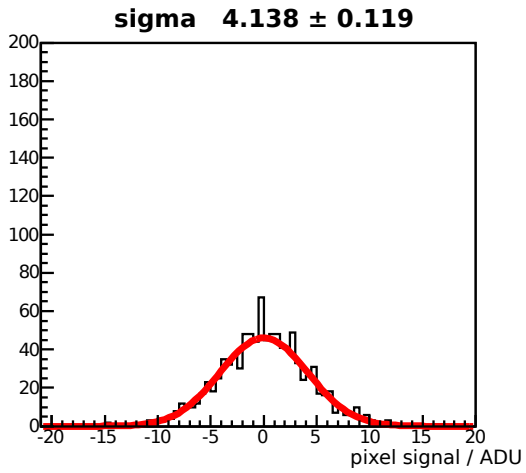

Figure 5.8.: Run HLL 281, Pixel 21: Pedestal distribution

the noise of repeated readout of a pixel.

5.6.1. Noise of the current digitisation

The noise of the drain current digitisation is cancelled out by averaging over a period of several samples (e.g. 30). However, this noise causes an uncertainty in the measurement which is given by equation 4.4. In the measurements presented, $\sigma(\bar{q})$ was in the order of 7 ADU = 14 nA.

5.6.2. Detector noise

The most interesting value is the noise of the detector. It can be measured by reading a DEPFET pixel out continuously several hundreds times in a black box and then filling a histogram with the pixel signal of the acquired empty frames. The histogram contains a Gaussian distribution with zero as mean value, if the pedestal subtraction works. The detector noise is defined as the standard deviation of this distribution. This noise comprises the noise of the DEPFET detector plus the noise of the read out electronics. Hence, the noise measured by the described method can be seen as an upper limit for the DEPFET noise.

An example of a noise measurement is given in fig. 5.8. The Gaussian fit results in a standard deviation of 4.1 ADU = 8.5 nA, which corresponds to a maximum detector noise of 24 e^- assuming a g_q of 350 pA/e^-.

5.6.3. Common mode noise

Common mode noise is the simultaneous variation of the signal of a group of pixels. Figure 5.9(a) shows how the average signal of the pixels sharing gate 2

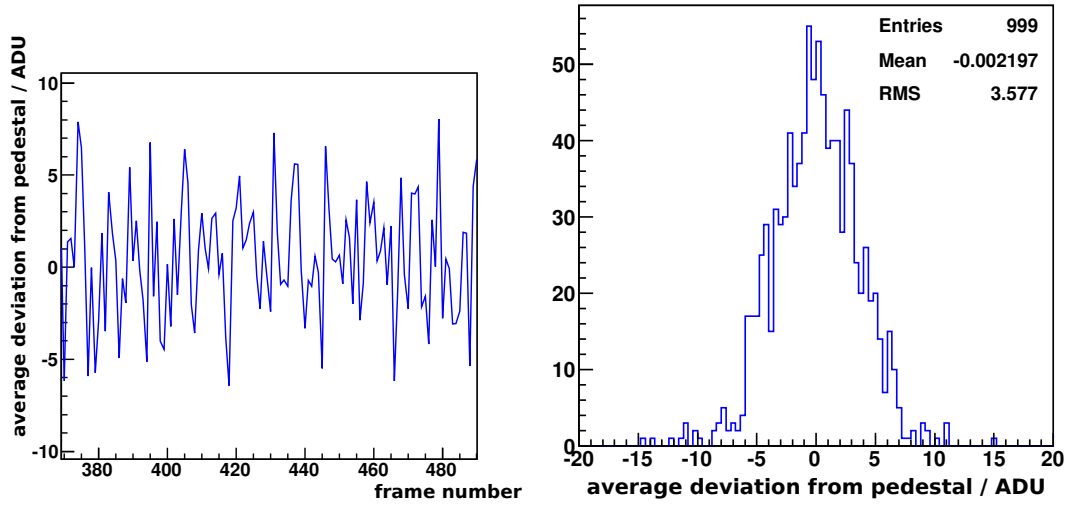

(a) temporal evolution (b) noise distribution

Figure 5.9.: Average variation of pixel signals from gate 2

changes from one frame to the other. The corresponding noise distribution is given in Figure 5.9(b).

The observed common mode noise is probably caused by the readout electronics, especially instabilities of the gate voltages between different frames could affect the final pixel signal. Therefore, a correction of the acquired data for the common mode noise in the analysis is advisable. Figure 5.10 shows the detector noise obtained with the corrected data. The correction reduces the estimated detector noise to 2.002 ADU, but, as explained in Appendix B, this value has to be corrected with a factor of $\sqrt{8/7}$. This results in a noise of 2.14 ADU or 13 e^-, assuming a g_q of 350 pA/e^-.

5.7. Laser tests

Laser tests give information about spatial differences of the pixel response. Studies of the intra pixel structure are of special interest. In contrast to beam tests the cost of laser tests is low and it is possible to have a setup in the local lab.

5.7.1. Preparation of the setup

The components of the setup are shown in Figures 5.11(a) and 5.11(b). A pulse generator defines the pulse shape of the 660 nm laser, which is connected via an optical fibre to the setup. By default the minimal achievable pulse length of 10 ns is chosen. The intensity of the laser is regulated via an optical attenuator. An optical head focuses the Gaussian laser beam to a typical spot size of $\sigma = 3\,\mu$m [10] on the

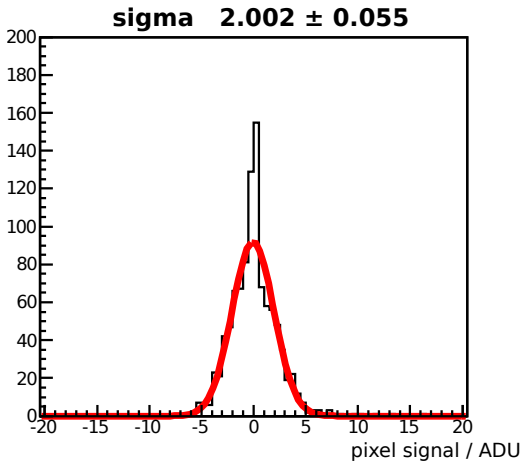

Figure 5.10.: Detector noise obtained after all corrections (including common mode correction)

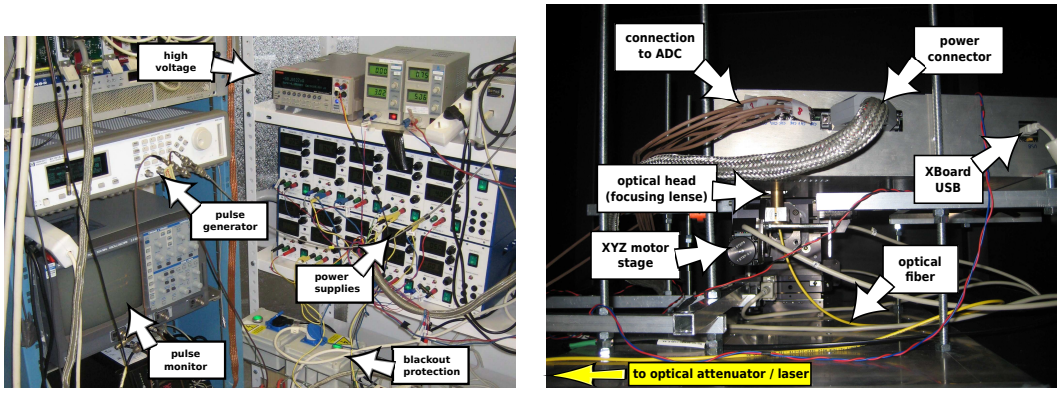

(a) power supplies

(b) content of black box

Figure 5.11.: Equipment used for the laser test

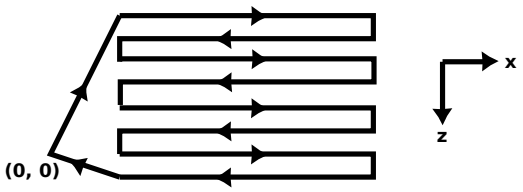

Figure 5.12.: Scanning scheme used in laser tests

backside of the matrix (see Fig. 3.6). The nominal focus distance of the optical head is 12 mm [31].

Finding a spot of several µm with a sensitive area of less than half a mm is not an easy task. The laser was set temporally to higher intensity (higher pulse rate, longer pulse length) for this purpose, and the spot was searched moving the setup manually and simultaneously looking at changes in the scope signal of the drain currents.

An XYZ motor stage controllable via RS232 ports is used to scan the matrix (X, Z direction) in steps of 2.5 µm and to focus the laser (Y direction). The scanning scheme is shown in Figure 5.12. The measurements were performed with the 4 channel version of the scope card which reads out only half of the matrix columns. To obtain the full picture of the matrix two scans of the entire matrix area were combined. In the first scan, the inner two columns of the matrix were read out, in the second scan, the outer columns. The data was then merged in the analysis.

The analysis consists mainly in the subtraction of the pedestals and clustering with the following algorithm:

1. Hit threshold: 20 ADU.
2. Minimum seed pixel signal: 50 ADU.
3. Clustering: consider only neighbours of the seed pixel (3×3 cluster).

Warning: The laser scans presented were performed with the first version of the preamplifiers and slightly insufficient clear voltage. The significance of the results is therefore limited.

5.7.2. Considerations about spot size and shape

In a naive approach, shape and size of the laser spot can be determined by using only one pixel of the matrix as detector and measuring its response for different laser spot positions to obtain a map of the laser spot. In reality this does not work for two reasons.

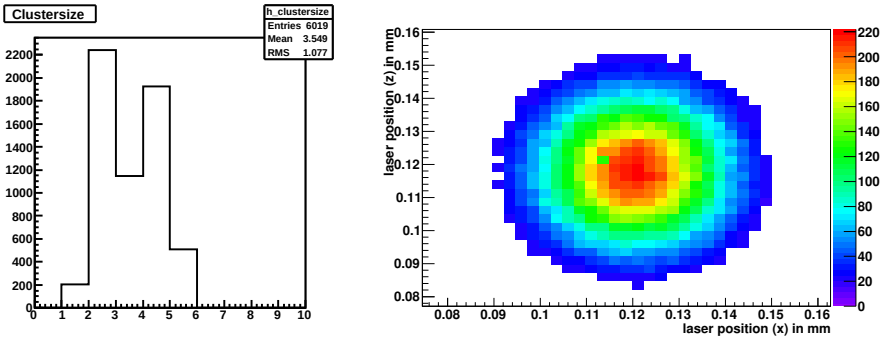

(a) Cluster size distribution (b) Response of pixel 21 for different laser positions

Figure 5.13.: Measures for the laser spot size

Firstly, the DEPFET pixel is not a point-like device, but charge is collected over a certain area. Things are made even more complicated by the fact that the charge collection efficiency varies in the sensitive area of the pixel depending on its internal structure. The pixel response can be described by a function depending on the position in X and Z within the pixel surface. Hence, the function describing the result of the proposed measurement would correspond to the convolution of the function describing the shape of the spot and the function describing the pixel response.

Secondly, the pixel can in no way be thought of as being a flat plane: with a thickness of 450 µm, the pixel is much thicker than it is long and wide! Additionally to the position in X and Z, the position in Y, which is the depth at which the measured electrons are actually created, also has to be taken into account. Electrons created right at the surface of the detector have a longer distance to traverse before they reach the internal gates and therefore show higher diffusion than electrons created deep inside the silicon.

When the backside of the matrix is irradiated with 660 nm laser light, the energy is deposited almost exclusively at the surface due to the extremely short attenuation length of only several µm (cf. Fig. 2.5). In this case, it is possible to assume the sensitive volume as a flat plane located at the detector surface.

Information about the spot size is crucial in laser tests to bring the optical head to the ideal focus distance and to obtain a minimum spot size. Large DEPFET test matrices used in beam tests are equipped with a metal cross for alignment in the centre of the detector [10]. This cross is also helpful for focusing because it provides a sharp edge. Mini matrices lack this cross and focusing can be achieved only by optimising the spot size by checking the scope signals of the matrix readout

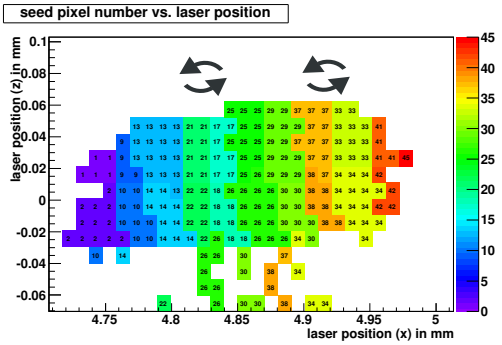

Figure 5.14.: Run 202: Example of wrong pixel assignment (rows are swapped)

and trying to reduce the number of firing pixels to a minimum, or by the proposed method of scanning a single pixel.

5.7.3. Verification of the pixel assignment

Since the raw data is only the signal of 8 scope channels, in order to describe the subsequent readout of the matrix rows, it is necessary to define in the software which part of the signal corresponds to which pixel and where it is located geometrically. Errors may occur in the definition of the readout sequence (the gates have to be switched on subsequently from 0 to 5), in the definition of the soft triggers or in the definition of which pair (scope channel, gate) corresponds to which position (X, Z) in the matrix. Moreover, the pixel assignment is not only a software issue. Swapped connections on the main board, or wrong cabling to the scope card have fatal effects.

Laser scans provide reliable information about the pixel assignment and are indispensable in the first testing phase of a system. Figure 5.14 illustrates how scrambled rows were identified and fixed (wrong relation between (scope channel, gate) and (X, Z)).

5.7.4. Results

Figure 5.15(a) shows the response of the seed pixel as a function of the laser position[3]. The individual pixels are clearly visible and apparently the first and last rows of double pixels have a lower signal than the rest of the matrix. The same conclusion can be drawn from Figure 5.15(b). It shows the maximum pixel response during the laser scan, which was obtained by searching the pixel data of the whole laser scan for maximum values. One column contains increased signals. It is not clear whether these observations are a property of the mini matrix and the setup,

[3] The plot is distorted because the axes have different units.

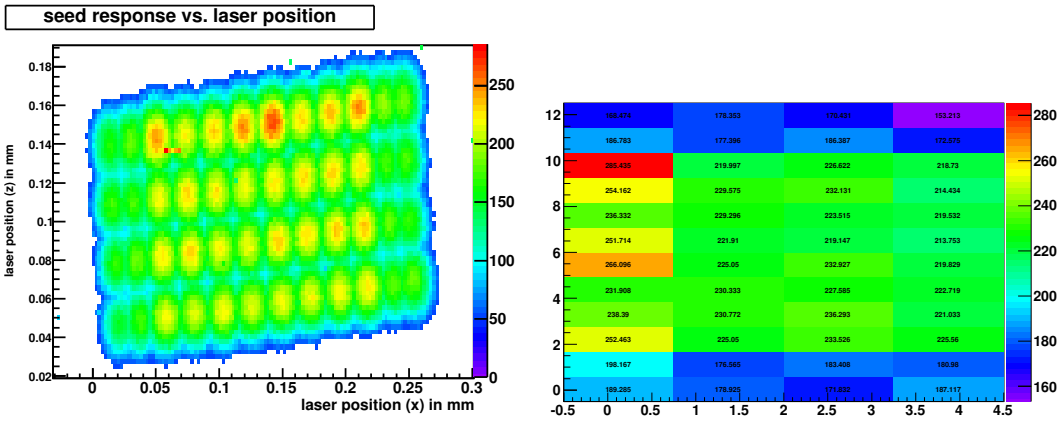

(a) seed pixel signal (b) maximum pixel response

Figure 5.15.: Differences in pixel response

or just caused by an incorrect setting of clear voltage and preamplifier feedback. A source test presented in the next section of this chapter will clarify this issue.

Other properties of interest investigated with the laser tests are the cluster charge and the ratio between seed charge and cluster charge. The results of such an analysis are depicted in Figures 5.16(a) and 5.16(b). Pixel borders are marked with black lines[4].

The cluster charge (Fig. 5.16(a)) is significantly lower at the edges of the matrix where the clusters lack the charge created outside of the matrix. The analysis also reveals a structure inside the pixels with differences up to 25% of the total collected charge. In addition to the incorrect operation parameters of the system, the spot size of the laser might play a role: the charge created diffuses to a radius larger than the pixel size (cf. Fig. 5.13(b)), and parts of the created charge might be outside the 3×3 cluster area and be cut off differently depending on where the pixel is hit.

The seed-to-cluster ratio (Fig. 5.16(b)) decreases towards the edges of the pixels because more charge is shared with the neighbouring pixel. The ratio reaches its minimum at the corner where four pixels are touching each other.

5.8. Source tests with ^{55}Fe and ^{109}Cd

Laser tests are limited by the fact that it is hard to determine the amount of charge created in the sensor, because the intensity of the laser pulse might be subject to changes over time and the reflectance of the sensor surface is not uniform.

[4]The plots are distorted because the axes have different units

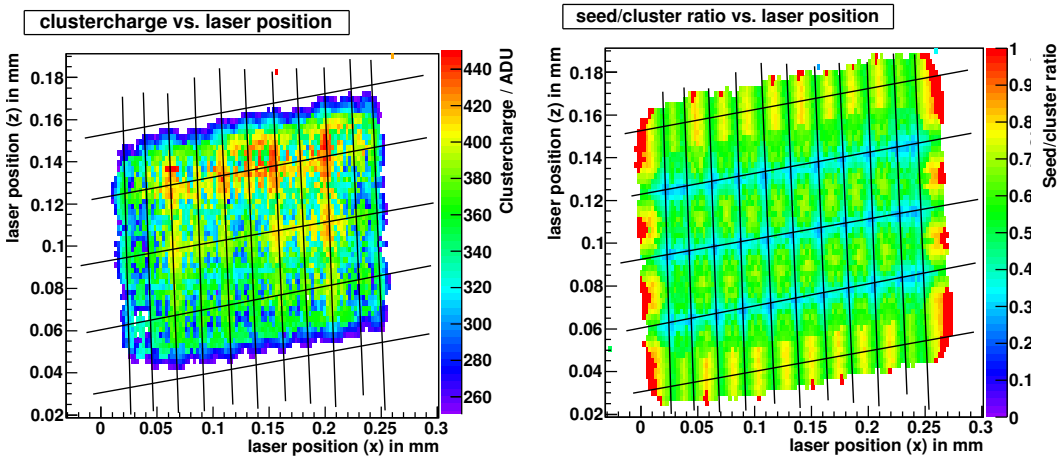

(a) Cluster charge (scope range 4V)

(b) Seed to cluster ratio

Figure 5.16.: Clustering

More elaborate setups have been proposed to compensate these fluctuations of created charge [32]. However, measurements using radioactive sources are far easier to perform and provide an exact knowledge of the deposited energy and therefore of the created charge. Hence, source tests are more suitable and widely used for detector calibration .

5.8.1. Experiment

The measurements presented were performed at MPI HLL with ^{55}Fe and ^{109}Cd sources placed (2 ± 1) *mm* above the backside (cf. Fig. 3.6) of the mini matrix. The exact position could not be determined, since the mini matrix is not aligned when it is glued to its ceramic socket and the pins of the socket are twisted. The activities of the sources were in the order of MBq.

The sampling rate of the scope card was lowered from 125 to 50 MS/s in order to achieve faster data processing and smaller raw data files. During the data collection an on-line hit selection was applied for further reduction of the raw data file size. Only the frames which contain a pixel signal over a preset threshold were saved to disk. The threshold can be set individually for the different gates of the matrix and was determined by taking into account the pedestal and noise of the pixels. The first bunch of the measurement was saved entirely to have data available for the calculation of the pixel pedestals.

Table 5.1.: Sources with relevant photon energies [33]

Element	Energy/ keV	number of created electrons	branching
^{55}Fe	5.9	1639	
^{109}Cd	22	6111	85%
	25	6944	14%
	88	24444	4%

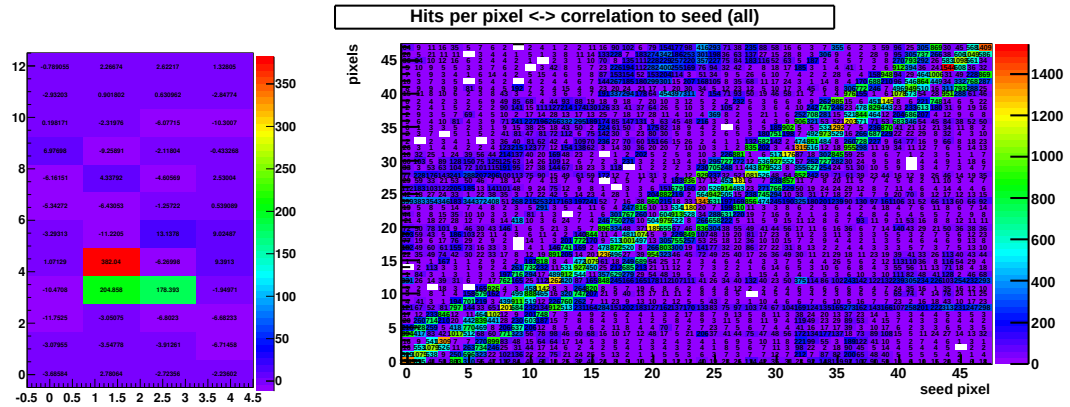

(a) Example event from ^{109}Cd

(b) Seed pixel vs. hits correlation plot

Figure 5.17.: Consistency checks

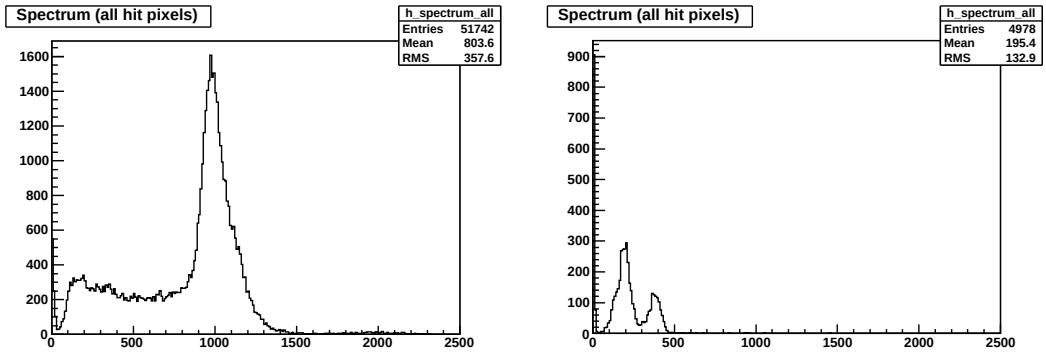

(a) ^{109}Cd (b) ^{55}Fe

Figure 5.18.: Spectra before clustering

5.8.2. Hit correlations

Hit correlation plots are a very effective test for the plausibility of the measurement and the integrity of the whole system. A first check is to look at events selected by the hit recognition algorithm. An example of such an event is given in Figure 5.17(a). It is clear that this event meets all requirements of a selectable event and conforms with the cuts presented above.

A correlation plot gives information about the whole measurement. The principle is simple: statistically, pixels which are neighbours of the seed pixel should be hit in a source measurement more often than other pixels. The x-axis of Figure 5.17(b) indicates the seed pixel number[5], the y-axis the pixel number of hit pixels. Let us consider for example pixel number 21 as a seed pixel. The numbers above 21 on the x-axis represent how often the corresponding pixels on the y-axis have been hit in *all* events where pixel 21 was the seed pixel. The highest entry is of course for pixel 21 because it is always hit itself when it is the seed pixel. Neighbour pixels of pixel 21 have also neighbouring pixel numbers. Hence, a "good" correlation plot is a diagonal band from the lower left to the upper right[6].

5.8.3. Spectra

Figures 5.18(a) and 5.18(b) show the spectra after the subtraction of the pedestals. All pixel signals of the whole matrix above a threshold of 12 ADU are simply added up without any further cuts. Incomplete clusters from the edge of the matrix are therefore included.

[5]for the pixel assignment see Appendix B, Figure B.1

[6]Due to the pixel numbering (cf. Appendix B, Fig. B.1), there are actually 3 bands in the correlation plot

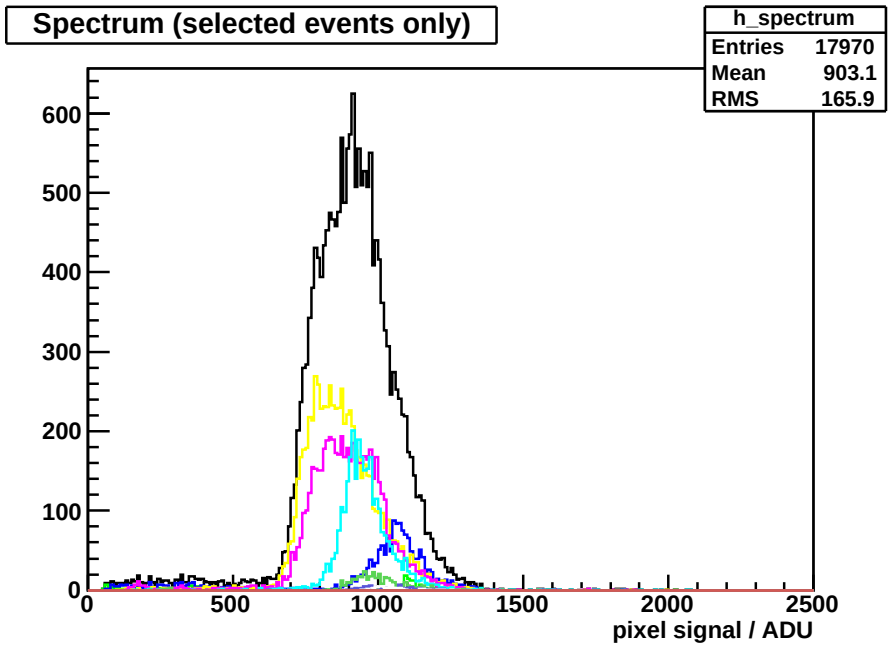

(a) ^{109}Cd

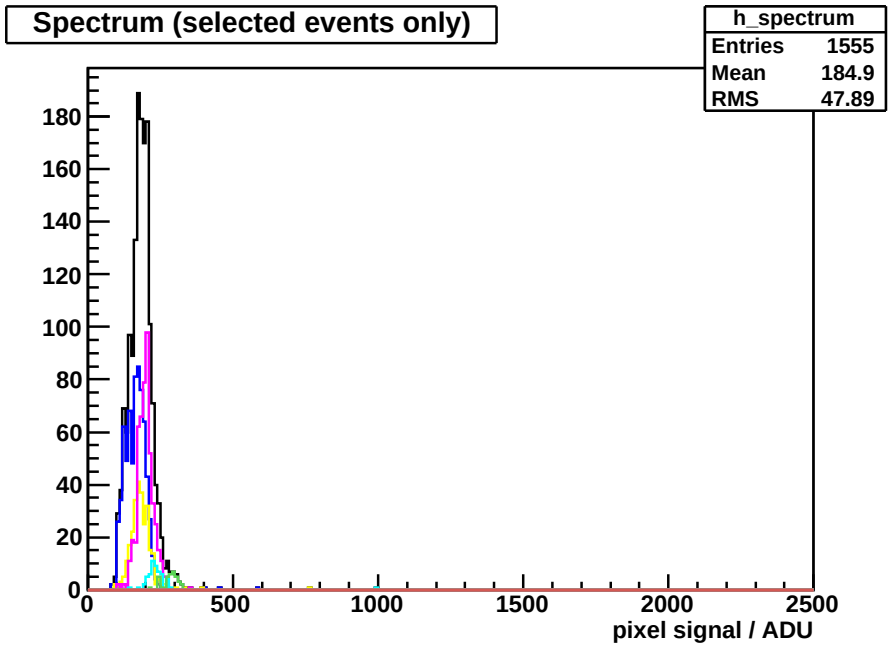

(b) ^{55}Fe

Figure 5.19.: Spectra measured with the mini matrix setup (The total spectrum is represented by the black line, contributions of different cluster sizes by the coloured lines. Figures 5.20(a) and 5.20(b) explain the colour key.)

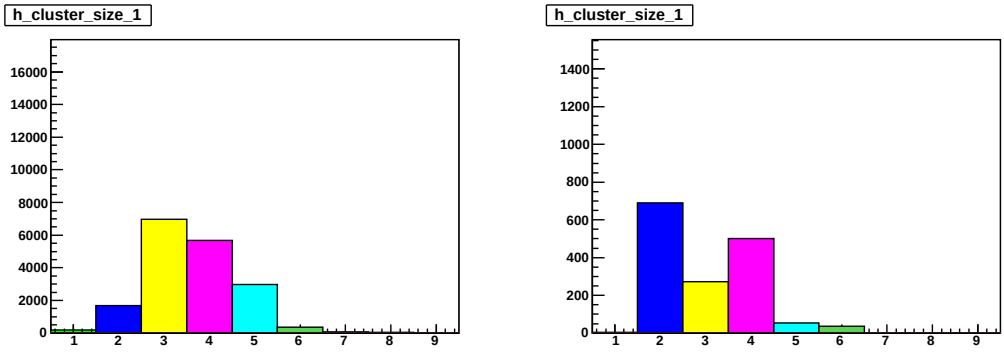

(a) ^{109}Cd (b) ^{55}Fe

Figure 5.20.: Cluster size

The data was processed with the `MimaRoot2SpectrumFast` macro. The following cuts were applied:

1. Hit threshold: 12 ADU.
2. Minimum seed pixel signal: 24 ADU.
3. Seed pixel is not located at the edge of the matrix.
4. Consider only direct neighbours of the seed pixel (3×3 cluster).

The resulting spectra are presented in Figures 5.19(a) and 5.19(b). The overall spectra are plotted in black; the coloured spectra correspond to the contribution of different cluster sizes. Figures 5.20(a) and 5.20(b) give the distribution of cluster size and explain the colour key.

Cluster size

The ^{109}Cd spectrum has significantly higher contribution of clusters of size 3 and 5 than the ^{55}Fe spectrum. Two effects may provide a possible explanation.

One is the generation of less charge by ^{55}Fe photons. Assuming that the most probable cluster size is 3 or 5 and considering clusters of 3 or 5 pixels containing 2 and 4 high-signal pixels, respectively, and one further low-signal pixel, the low-signal pixel would be below the threshold in the ^{55}Fe and therefore excluded from the analysis while it is included in the ^{109}Cd spectrum.

A further effect to be taken into account is the dependence of the photon absorption probability on the energy (cf. Fig. 2.6). Photons from ^{55}Fe have a higher probability of being absorbed and most of them are already absorbed near the surface of the detector. This hypothesis is supported by a comparison with the cluster size distribution of the laser test (Fig. 5.13(a)) where the 660 nm light is also absorbed near the detector surface. The different positions of charge generation might lead to different cluster size distributions.

Contribution of different cluster sizes to the spectrum

Figures 5.19(a) and 5.19(b) show that clusters of different sizes result in different peaks causing a broader peak in the total spectrum. In the ^{109}Cd spectrum the highest amount of charge is collected by clusters of two pixels, but this is not a general rule, as the ^{55}Fe spectrum shows.

Variations in the charge collection depending on the absorption position of the X-ray photon can explain this observation. A similar result was already obtained in the laser test. DEPFET devices for X-ray spectroscopy application are usually equipped with larger pixels to reduce this effect.

5.8.4. Estimation of the internal amplification of the DEPFET

The internal amplification of the DEPFET describes how much the output current of the DEPFET transistor changes for a given number of electrons collected at the internal gate.

Method

X-ray sources have a spectrum with discrete energy peaks. Table 5.1 lists the used radioactive elements. Photons with energies below 100 keV interact mainly via the photo effect (cf. chapter 2.3) with the detector silicon and are destroyed during this process. Hence, their complete energy is deposited in the detector and used to create electron–hole pairs. The number of created electrons can be derived from the mean energy to create one electron–hole pair ($E_{\mathrm{eh}} = 3.6\,\mathrm{eV}$):

$$N(e^-) = E_\gamma / E_{\mathrm{eh}} \tag{5.2}$$

Results

Under ideal conditions the X-ray spectra would be described by a Gaussian distribution. Due to reasons discussed above, this is not the case for the present measurements. The peak positions can only be given as a range. Table 5.1 lists the measured current ranges. The internal amplification of the DEPFET is given by equation 3.2 and can be approximated by:

Table 5.2.: Data for the determination of g_q

	X-ray peak	created charge	measured current
^{55}Fe	5.9 keV	1639 e^-	309 . . . 412 nA
^{109}Cd	22 keV	6111 e^-	1616 . . . 2181 nA

$$g_q = \frac{\mathrm{d}I}{\mathrm{d}Q} \approx \frac{\Delta I}{\Delta Q} \tag{5.3}$$

Using this equation, the g_q of the measured mini matrix is in the range of 269 to 419 pA/e^-. The result is compatible with values from previous measurements [34] [35] [17] [14]. A more precise measurement would require a better understanding of the spectra and the evaluation of further spectra to be able to make a linear fit through several reference points.

5.8.5. Seed pixel spectra

If the cluster size is limited to one pixel (1 × 1 cluster), a seed pixel spectrum is obtained. The seed pixel spectrum contains all events and all pixels. The cluster charge is equal to the seed pixel charge. This has to be distinguished from a single pixel spectrum which would contain all events, but only the signal of one pixel (e.g. pixel number 12) is evaluated.

Figures 5.21(a) to 5.21(d) show seed pixel spectra for the first row of double pixels (gate 0) and the inner rows (gate 1 to 4). In the latter, the number of entries is four times higher, corresponding to the number of evaluated double rows which is four times higher. The ^{109}Cd peak is at a 2% lower value and the ^{55}Fe at a 10% lower value in the first row of double pixels.

This confirms the result from the laser test, according to which the pixels of the first and last row of double pixels have smaller gain than pixels from the inner rows, although the effect observed in the source measurement is less pronounced.

5.9. Conclusion

The first group of measurements evaluated the properties of the system itself. Specifically, the signal shapes of the steering pulses were measured, the linearity of the preamplifiers was determined, and the long term stability of the system was investigated. Furthermore, a detailed look at the signal shape of the preamplifier output signal led to a significant improvement of the preamplifier circuits.

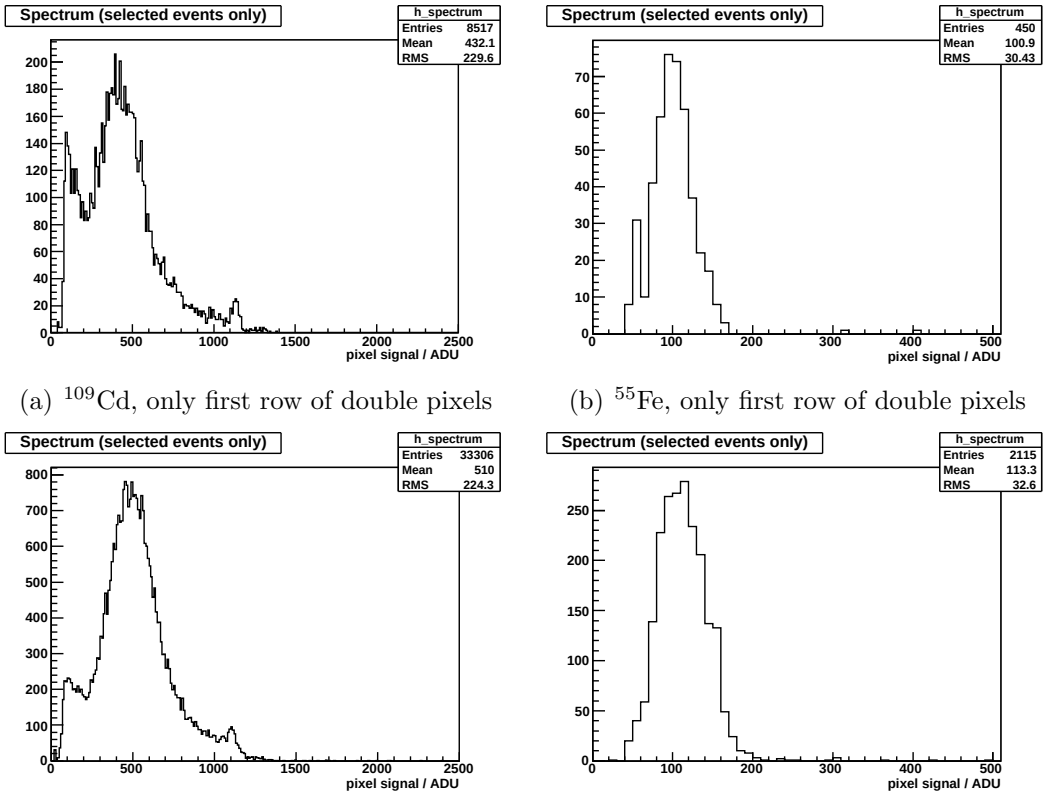

(a) ^{109}Cd, only first row of double pixels

(b) ^{55}Fe, only first row of double pixels

(c) ^{109}Cd, only inner rows of double pixels

(d) ^{55}Fe, only inner rows of double pixels

Figure 5.21.: Seed pixel spectra

Table 5.3.: Causes of uncertainty in measurements with the mini matrix setup

Cause of uncertainty	Effect on pixel signal ΔI	Remedy
incomplete clear	unknown	higher clear voltage, longer clear pulse
non-linearity of the preamplifiers	$< 15\,\mathrm{nA}$	negligible, if non-linearity at zero is avoided
distortion of the preamplifier signal after switching	$40\,\mathrm{nA}$	slower readout, longer relaxation times
sampling noise	$14\,\mathrm{nA}$	averaging
common mode noise (gate switchers)	$7\,\mathrm{nA}$	common mode correction
imprecise setting of soft triggers	$15\,\mathrm{nA}$	—
incomplete clusters in source tests	—	additional integration time

The second group of measurements were tests of DEPFET mini matrices. The evaluation of the pedestal signals resulted in negative pedestals distributed inhomogeneously over the mini matrix matrix. Different sources of noise in the system were identified and measured, namely, the noise in the current digitisation, the DEPFET noise and the common mode noise caused by the switching circuits. Laser tests helped to correct the erroneous pixel assignment of the matrix. Moreover, it was demonstrated that it is possible to perform laser tests using a scope card with only 4 channels. The system is ready for standard analyses of laser tests such as charge collection and seed-to-cluster ratio plots. First spectra of ^{55}Fe and ^{109}Cd were obtained. These spectra allowed the determination of the internal amplification g_q of the mini matrix DEPFETs. The integrity of the source tests was checked with correlation plots. The inhomogeneity of the charge collection in the first and last matrix row already discovered in laser tests was confirmed in the analysis of seed pixel spectra.

Table 5.3 lists the sources of uncertainty in measurements with the mini matrix setup, as well as aspects mentioned in chapter 4. Currently, the most relevant problem of the system is that there is not enough relaxation time after the application of the steering pulses (see Fig. 5.6(b)). However, the readout time of 4 ns was maintained after the discovery of this unwanted effect in order to ensure that the results of all measurements were comparable. Future measurements should use a slower readout sequence.

6. Implementation of the PXD and SVD geometry and materials in the BASF2 framework

A high energy physics experiment needs an comprehensive collection of software for design studies, analysis and also for its operation. This software is integrated in a framework. Improvements in the available software were made since the relase of the former *basf*[1] framework. Furthermore, the Belle II experiment will contain an additional detector: the PXD. All in all, the old framework of the Belle experiment could not meet the requirements. As an interim solution, first performance studies of the Belle II vertex detector were carried out with the ILC framework[2] as interim solution. However, the ILC framework lacked some essential functionality necessary for the Belle II experiment[3] and so an intensive development of a new framework, basf2, was started in April 2010. Less than one year later (February 2011) a first release could be presented.

One of the objectives of the framework is to provide a realistic simulation of the detector. This involves a precise description of the shape of the detector components, their position within the detector and the composition of its materials. Moreover, the response of the detector to a passing particle has to be simulated with a so called digitiser. The IPNP in Prague contributes the implementation of the geometry and the digitiser for the vertex detector (PXD and SVD).

After a short introduction to the general principles of simulating the geometry, I will describe how the geometry is integrated in the basf2 framework. This will be followed by the presentation of the details of the geometry implementation of the PXD and SVD. Finally, the material budget studies performed in the ILC framework are compared to the results obtained in the basf2 framework.

[1] Belle Analysis Framework
[2] created for design studies for a future international linear collider
[3] e.g. tracking capability for the slanted detectors of the SVD

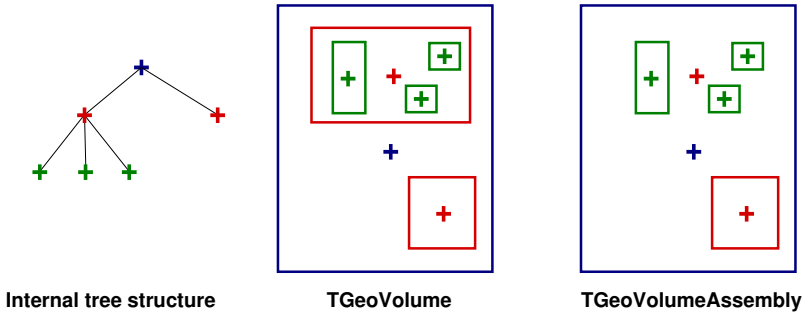

Figure 6.1.: Internal tree structure of the ROOT geometry, comparison of TGeoVolume and TGeoVolumeAssembly

6.1. The geometry implementation within the basf2 framework

6.1.1. The ROOT geometry package

Geometric objects are represented in the ROOT software[28] by the TGeoVolume class. They are characterised by their shape (TGeoShape) and the material they are made of (TGeoMaterial). ROOT organises TGeoVolume objects in a tree structure to keep track where they are positioned in space. Every volume contains a reference point (origin) located at its centre. Volumes are positioned in relation to the origin of the mother volume. Figure 6.1 illustrates the geometry structure.

ROOT provides a set of basic shapes (box, tube, etc.) to create the detector geometry. However, these standard shapes are not sufficient to represent the complex structure of the detector. Three different options are provided to generate more complicated structures:

- Several volumes described by standard shapes are positioned in a mother volume described by a standard shape. The mother volume may be made of air and therefore be "invisible".
- When no adequate mother volume comprising all daughter volumes can be found, a *TGeoVolumeAssembly* provides an origin to position daughter volumes, without a shape having to be defined (cf. fig. 6.1).
- *Composite shapes* obtained from the standard shapes by Boolean operations (union, intersection, subtraction).

A prerequisite for navigation within the geometry is to provide an answer to the question: Where am I? ROOT provides the answer by searching the tree structure of the geometry starting from the top volume. All contained daughter volumes are

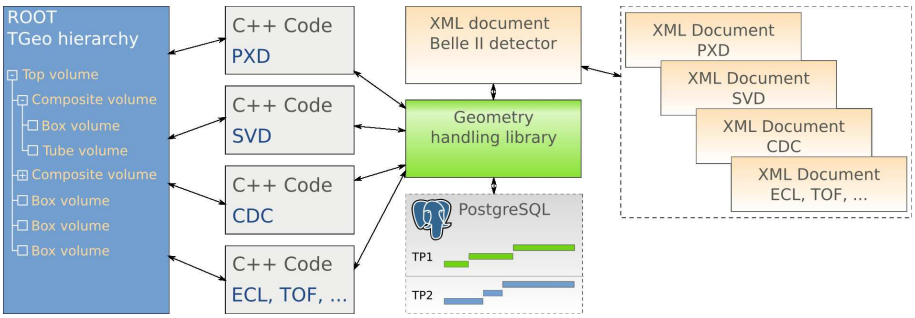

Figure 6.2.: Generation of geometric objects within the basf2 framework[36]

checked to see if they contain the requested point in space. If the requested point is found in one of the contained volumes, the navigation code continues its search within this volume and so on.

It follows from this algorithm, that the navigation through a geometry using a tree structure of volumes containing other volumes is much faster than a flat structure where all volumes always have to be checked to see if they contain the requested point. Furthermore, TGeoVolumeAssemblies should be avoided because they do not define a proper container for their daughter volumes and thereby deteriorate the speed of navigation. This disadvantage is further compounded when TGeoVolumeAssemblies are positioned inside other TGeoVolumeAssemblies.

6.1.2. Integration of the ROOT geometry into the basf2 framework

Figure 6.2 illustrates how the ROOT geometry package is integrated in the basf2 framework. The parameters of the geometry are stored in XML files and a database. A geometry handling library manages the creation of the geometry. For each subdetector it calls C++ programs for building the geometric structure. While the structure of the geometry (see next section) is described by the C++ programs, parameters such as dimensions and materials are included in the XML-files or a database in order to facilitate any changes that may be necessary in the future.

XML[4] is a language dedicated to the exchange of data. XML files are plain text files which organise the data in a tree structure. This parallel to the tree structure of the ROOT geometry makes XML an attractive candidate for storing information about the detector geometry. However, a detector such as the PXD is build of several identical parts, for example, the silicon sensors. A replication of the parameters can be avoided by saving common information into external XML files which can then be included in the main XML document wherever the identical information is needed.

[4]Extensible Markup Language

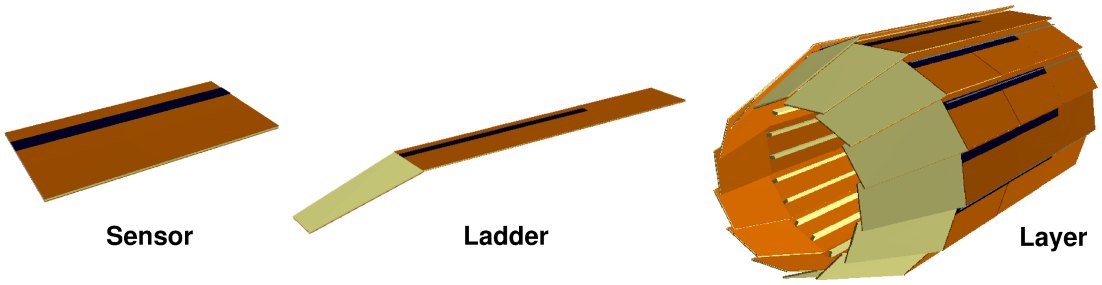

Figure 6.3.: Structure elements of the vertex detector using the SVD as an example

6.2. Design of the geometry implementation of PXD and SVD

The Belle II vertex detector is composed of two separate subdetectors, namely the PXD and SVD. Nevertheless, their geometrical design follows the same hierarchical and symmetrical structure. The individual *sensor* modules are grouped in z direction to form a *ladder*. These ladders are arranged in a total of $2+4=6$ *layers*. The elements of the structure are summarised in Figure 6.3.

The C++ code of the geometry implementation follows this structure of Sensors, Ladders and Layers. Each `TGeoVolume` object of the geometry is created by a dedicated C++ class. This C++ class reads the parameters from the parameter storage with an `init()` method and then creates the corresponding `TGeoVolume` object with a `make()` method. A number of identical tasks have to be done for every object, for example, reading parameters for the dimensions (length, width, thickness) and the material. Therefore, a base class `B2GeoVolume` providing this common functionality was developed.

Figure 1.6 shows the current status of the geometry implemenation of the vertex detector. Implemented details are: the silicon sensors including the sensitive area, a simplified version of the readout chips and, for the SVD, the support structure, cooling pipe and the electric connection with a Kapton flex cable.

6.3. Density correction

The simulated geometry provides only a simplified model of the real detector. Despite the possibility of building complicated structures from the provided basic shapes, the working capacity of the people involved limits the achievable complexity of the geometry. Furthermore, an excessively detailed geometry is not desirable, because it prolongs navigation times through the structure, extends the time needed to run the simulations and thus increases the computing costs.

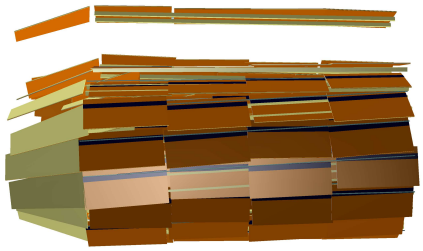

Figure 6.4.: Example of (extreme) offsets from ideal positions

However, a realistic simulation of the particle transport is desirable in spite of the simplified simulated geometry. The particle transport is influenced by the number and type of atoms a particle encounters during its passage. The crucial parameters are *mass* and *material composition* of the detector components.

All detector components are listed in a spreadsheet document[5]. Even small components (e.g. a stainless steel screw) are represented with their correct mass. If such a component is not included in the description of the geometry, the corresponding amount of material is added to another adjacent volume by changing its material composition and mass. During the geometry creation a dedicated algorithm recalculates the density of the detector components in order to implement their correct masses. In other words, an incorrect density goes into the simulation, but the mass is correct.

6.4. Offsets from ideal positions

Up to now only an ideal detector geometry, as defined by the technical drawings, has been considered. In real life the mechanical precision is limited, structures are deformed by their weight and even time dependent fluctuations of detector positions are expected. The position of the sensors (= active material) is derived from the tracks of passing particles in an alignment procedure whereas the position of the mechanical support structure cannot be measured.

A problem arises when the sensors are moved according to the result of the alignment to their real positions, because this might cause illegal overlaps with the support structure. Two different approaches are possible to deal with this problem:

[5]This document is maintained by Peter Kodyš (peter.kodys@mff.cuni.cz)

- Disconnection of the sensors from the support structure by leaving a sufficient gap in between. The entire support structure is then treated as rigid and the sensors are moved relatively to it.
- Estimation of the position of the support structure using the sensor positions. This offers a more realistic description of the actual situation.

In the present geometry description the second approach was chosen. The offset of the sensors are read from the parameter storage. Offsets of ladders and layers are then calculated as average value of the offsets of all contained sensors. An example is given in fig. 6.4. It is clearly visible that the support ribs of the SVD ladder moved with the attached sensors.

6.5. Material budget

A good validation of the implemented geometry may be obtained by comparison with the geometry previously implemented in the ILC framework. Material budget plots serve as a powerful tool supplying a picture of the detector as a particle would see it. The material budget is expressed in units of radiation length X_0, which has been introduced in the theory chapter. For each subdetector two plots are presented: one describing the material budget for different angles ϕ (rotation about z axis) and the other for different angles θ. The algorithm for obtaining the plots is as follows:

1. Go to start point = nominal interaction point = $(0, 0, 0)$
2. Generate a random direction vector.
3. Go to next geometrical boundary in this direction.
4. Calculate the covered distance in terms of radiation lengths and add it to the total radiation length for this direction.
5. If the end of the detector is not reached, go to step 2.
6. Add the total radiation length for this direction to the corresponding bin of the material budget histogram.
7. If there are not enough entries in the histogram, continue with step 1.
8. Normalise the histogram to one entry per bin.

First, I would like to go into the details of the PXD plots. The material budget simulation performed with the basf2 framework does not distinguish between the passive material from the silicon support frame and the electronics. The red and green area in the ILC plots (Figs. 6.5(c) and 6.5(d)) is equivalent to the red area in the basf2 plots (Figs. 6.5(a) and 6.5(b)).

All in all, the amount of material is the same in both simulations with a slightly higher material budget in the basf2 simulation. However, the "peaks" in Figures 6.5(a) and 6.5(c) are in reverse order. This is caused by a wrong orientation of the windmill structure in the basf2 implementation. This bug has been already fixed — the plot obtained from the erroneous geometry was kept here to show the effectiveness of material budget plots.

The plots in θ direction differ in that the (green) hills present in the ILC geometry are missing in the basf2 geometry. This can be explained by the fact that the ILC geometry contains a more detailed implementation of the electronics bonded to the silicon sensor. The basf2 geometry contains at present only a simplified description of the electronics which will be updated later. Furthermore, the two peaks at 50° in the ILC geometry correspond to one broader peak in the basf2 geometry. This is due to the more precise description of the DEPFET sensor thinning in the new framework.

The material budget of the SVD detector is also, on the whole, identical in both implementations. Differences can be explained in terms of simplified readout chips, the missing support ribs in the basf2 framework and the distances between the sensor modules being too large in the ILC framework.

6.6. Conclusion

The full Belle II vertex detector was implemented in the basf2 framework with an object oriented approach. Each detector component is represented by a C++ class. A base class `B2GeomVolume` provides common functionality for all components. A density correction algorithm ensures that the correct amount of material is subjected to the simulation, even if the shapes of detector components are simplified. Moreover, the handling of detector offsets was integrated. A ROOT macro for material budget plots was written, and the results obtained are in good agreement with previous simulations in the ILC framework.

The XML files contain the position of the detector components as positions in the corresponding mother volumes. A spreadsheet document or a script deriving these parameters from the numbers shown in the technical drawings would be advantageous. The simulation speed could be significantly improved by replacing the `TGeoVolumeAssembly` objects for the detector layers by appropriate `TGeoCompositeShape` objects.

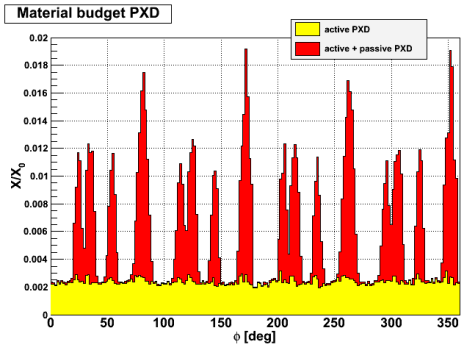

(a) in ϕ (simulation: C. Oswald, basf2)

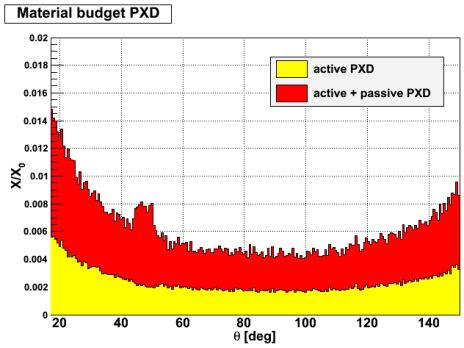

(b) in θ (simulation: C. Oswald, basf2)

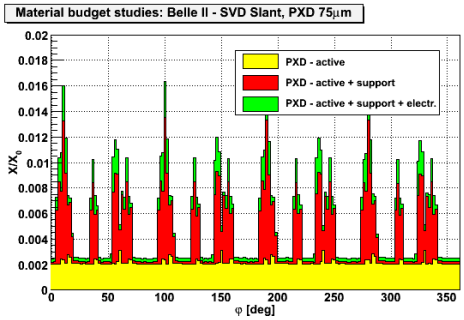

(c) in ϕ (simulation: Z. Drasal, ILC)

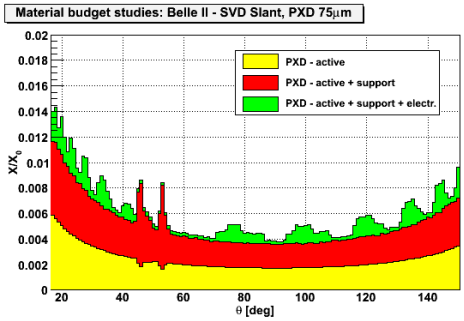

(d) in θ (simulation: Z. Drasal, ILC)

Figure 6.5.: Material budget studies for the PXD

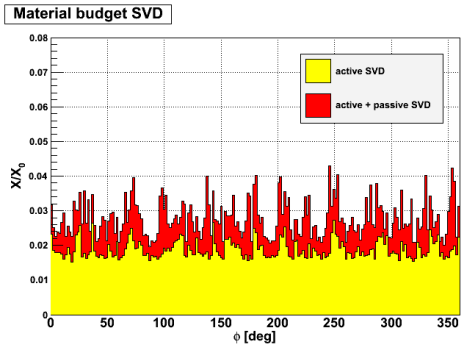

(a) in ϕ (simulation: C. Oswald, basf2)

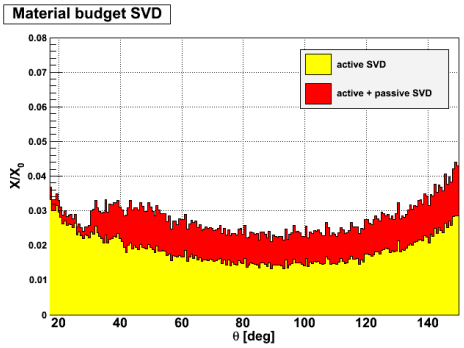

(b) in θ (simulation: C. Oswald, basf2)

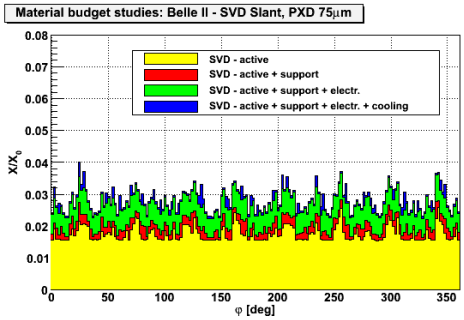

(c) in ϕ (simulation: Z. Drasal, ILC)

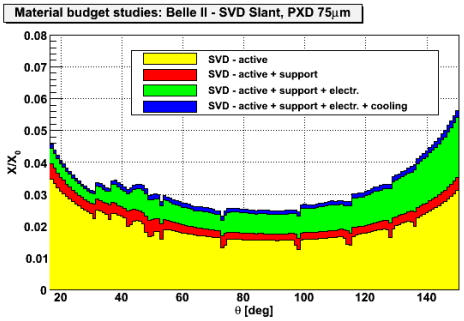

(d) in θ (simulation: Z. Drasal, ILC)

Figure 6.6.: Material budget studies for the SVD

7. Conclusion

The mini matrix system, a low noise readout system for small DEPFET matrices of 8×12 pixels, was studied, a software package was developed and first measurements were performed.

The software package comprises dedicated programs for controlling and programming the hardware, namely, the sequencer unit (XBoard), the ADC card and a motor stage for laser tests. Furthermore, a concept for steering the measurements was developed and implemented. All standard measurements for detector tests are possible. The results from the the measurements are evaluated with dedicated analysis macros.

First measurements were performed, namely noise measurements, laser scans and source tests. The functionality of the system was validated and the low noise performance confirmed. Moreover, the careful characterisation of the system led to substantial improvements of the hardware.

Besides the presented work on the mini matrix system, the simulation of the whole Belle II vertex detector was implemented in the new basf2 framework. Special features are the density correction maintaining the correct masses of simplified detector components and the offsets. The geometry was validated by comparison of the material budgets in the basf2 framework and the ILC framework.

This thesis showed that diverse tasks have to be accomplished to build a high energy physics experiment. The contribution of many people, not only physicists, is necessary to make it possible to start the BELLE II experiment in 2014, as planned...

A. Abbreviations, formula symbols and frequently used terms

A.1. Abbreviations

ADU	Analogue-to-Digital Unit
ADC	Analogue-to-Digital Converter
API	Application Programming Interface
BASF	Belle AnalySis Framework
CCD	Charge Coupled Device
CCG	Common Clear Gate
CERN	Conseil Européen pour la Recherche Nucléaire
DAQ	Data AcQuisition
DEPFET	DEPleted Field Effect Transistor
HLL	HalbLeiterLabor (semiconductor laboratory)
ILC	International Linear Collider
IPNP	Institute for Particle and Nuclear Physics
LHC	Large Hadron Collider
MOSFET	Metal Oxide Silicon Field Effect Transistor
MPI	Max Planck Institut
PCB	Printed Circuit Board
PXD	PiXel Detector
SVD	Silicon Vertex Detector
TB	Test Beam
USB	Universal Serial Bus
XML	eXtensible Markup Language

A.2. Used formula letters

g_q	Internal amplification of the DEPFET
r_e	Classical electron radius
m_e	Electron mass
N_a	Avogadro's number
A	Atomic weight
Z	Atomic number
ρ	Mass density
β	v/c
γ	$1/\sqrt{1-\beta^2}$
$\tilde{\lambda}$	Mean free path
X_0	Radiation length

A.3. Frequently used terms

Bunch	Collection of several subsequent readout frames
Common Mode	
Cluster	Group of pixels hit by the same particle
Cluster charge	Sum of the charge collected in all pixels of a cluster
Cluster size	Number of pixels contained in the cluster
Event	One readout cycle of a scope channel
Frame	One readout cycle, which reads outs the complete DEPFET matrix
Pedestal	Pixel signal without external source
Pedestal current	Drain current of the DEPFET directly after the clear
Pixel signal	Difference between the drain current before clear and the pedestal current
ROOT	Analysis framework designed for high energy physics
Seed pixel	Pixel of a cluster with the highest signal
Soft trigger	Specifies which of the acquired samples are evaluated to calculate the pixel signal
XBoard	Flexible sequencer unit developed by A. Wassatsch MPI HLL

B. Appendix: Mini matrix setup

B.1. Pixel map

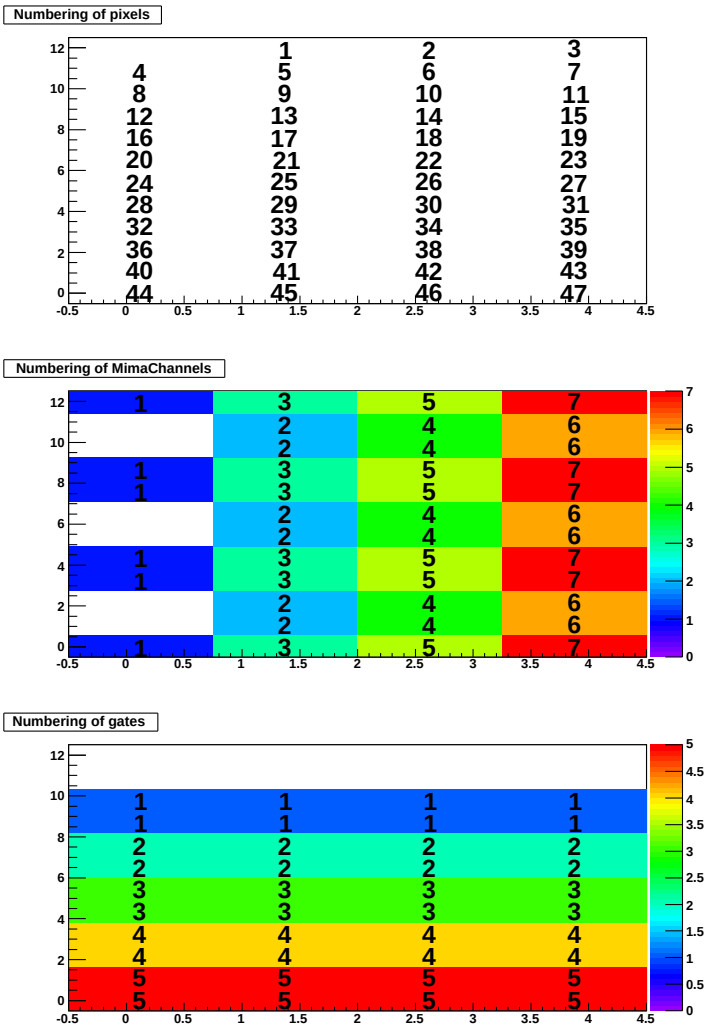

Figure B.1.: Pixel map of the mini matrix, assignment of drain channels and gates

B.2. Common Mode Correction

Let's consider a common mode in the $m = 6$ gates of c_i ($i = 0 \dots 5$) and a common mode in the ($n = 8$) amplifiers of d_k ($k = 0 \dots 7$). The common modes c_i and d_k add to the actual pixel signal q_{ik} and the measured pixel signal $\hat{q}_{ik}$ reads:

$$\hat{q}_{ik} = q_{ik} + c_i + d_k \tag{B.1}$$

For the common mode of the gates follows:

$$c_i = \hat{q}_{ik} - q_{ik} - d_k = \tag{B.2}$$

$$= \frac{1}{n} \sum_{l=0}^{n} (\hat{q}_{il} - q_{il} - d_l) \tag{B.3}$$

The correction c'_i for the gate common mode c_i is calculated by taking the average of all measured signals $\hat{q}_{ik}$ of gate i:

$$c'_i = \frac{1}{n} \sum_{l=0}^{n} \hat{q}_{il} = \tag{B.4}$$

$$= c_i + \frac{1}{n} \sum_{l=0}^{n} q_{il} + \frac{1}{n} \sum_{l=0}^{n} d_l \tag{B.5}$$

In order to obtain the corrected pixel signal q'_{ik}, the calculated common mode c'_i is subtracted from the measured pixel signal $\hat{q}_{ik}$:

$$q'_{ik} = \hat{q}_{ik} - c'_i = \tag{B.6}$$

$$= \cancel{c_i} + q_{ik} + d_k - \cancel{c_i} - \frac{1}{n} \sum_{l=0}^{n} q_{il} - \frac{1}{n} \sum_{l=0}^{n} d_l \tag{B.7}$$

The next step is to calculate the common mode of the amplifiers d'_k by averaging over the obtained pixel signals q'_{ik}. Then the final pixel signal q''_{ik} is calculated by subtracting d'_k from q'_{ik}:

$$d'_k = \frac{1}{m} \sum_{s=0}^{m} q'_{sk} = \tag{B.8}$$

$$= \frac{1}{m} \sum_{s=0}^{m} q_{sk} + d_k - \frac{1}{n} \frac{1}{m} \sum_{l=0}^{n} \sum_{s=0}^{m} q_{sl} - \frac{1}{n} \sum_{l=0}^{n} d_l \tag{B.9}$$

$$q''_{ik} = q'_{ik} - d'_k = \tag{B.10}$$

$$= q_{ik} + \cancel{d_k} - \frac{1}{n} \sum_{l=0}^{n} q_{il} - \cancel{\frac{1}{n} \sum_{l=0}^{n} d_l} - \frac{1}{m} \sum_{s=0}^{m} q_{sk} - \cancel{d_k} + \frac{1}{n} \frac{1}{m} \sum_{l=0}^{n} \sum_{s=0}^{m} q_{sl} + \cancel{\frac{1}{n} \sum_{l=0}^{n} d_l} \tag{B.11}$$

The derived equations relate the calculated pixel signals q'_{ik} and q''_{ik} to the actual pixel signal q_{ik}. This relation allows the actual noise of the pixel signal σ_{ik} to be estimated from the noise of the calculated pixel signal σ''_{ik}. It is assumed that the noise of all pixels is approximately the same ($\sigma_{ik} \approx \sigma$) and the average over several pixel signals is approximately zero ($\sum q_{ik} \approx 0$).

$$\sigma''^2 = \sigma^2 \left[1 - \frac{1}{n} - \frac{1}{m} + \frac{1}{nm}\right] = \frac{35}{48}\sigma^2 \tag{B.12}$$

If the pixel signal is evaluated by correlated double sampling, the common mode of the amplifiers (= fluctuating pedestals) should be already eliminated in the subtraction of the signals before and after clear. It follows $d_k = 0$ and the amplifier wise common mode correction becomes obsolete. For the calculated pixel noise follows:

$$\sigma''^2 = \sigma^2 \left[1 - \frac{1}{n}\right] = \frac{7}{8}\sigma^2 \tag{B.13}$$

B.3. Circuits

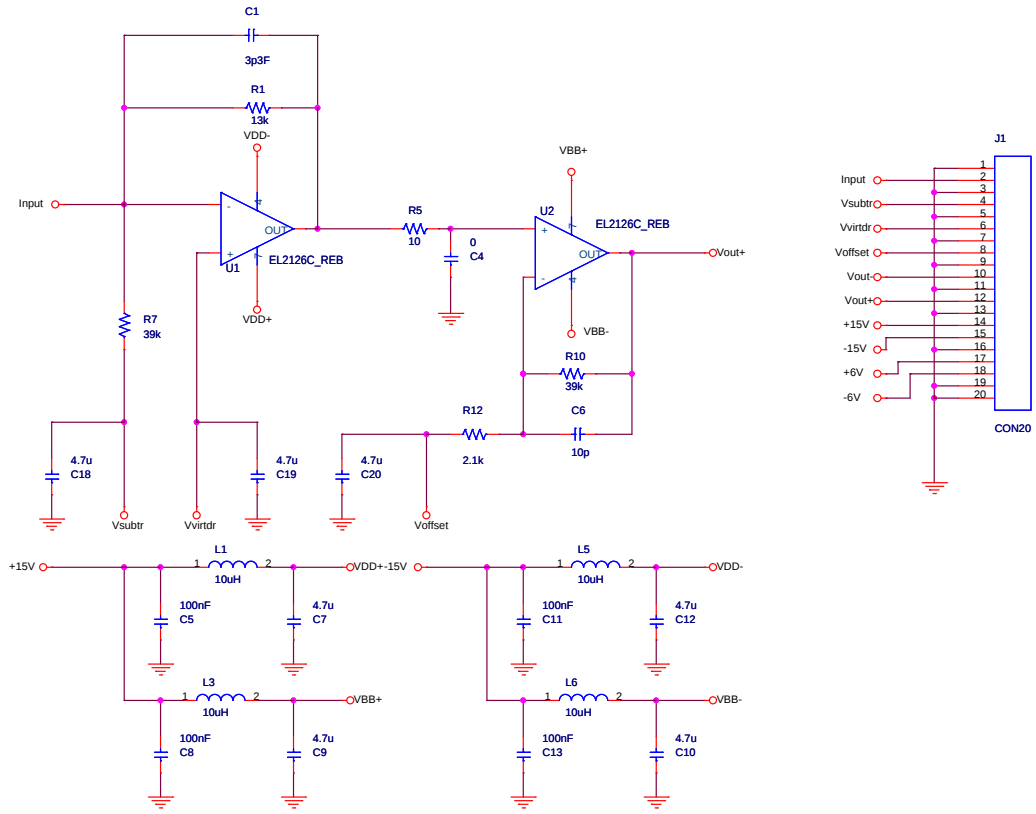

Figure B.2.: Final version of the preamplifier (layout: J. Scheirich)

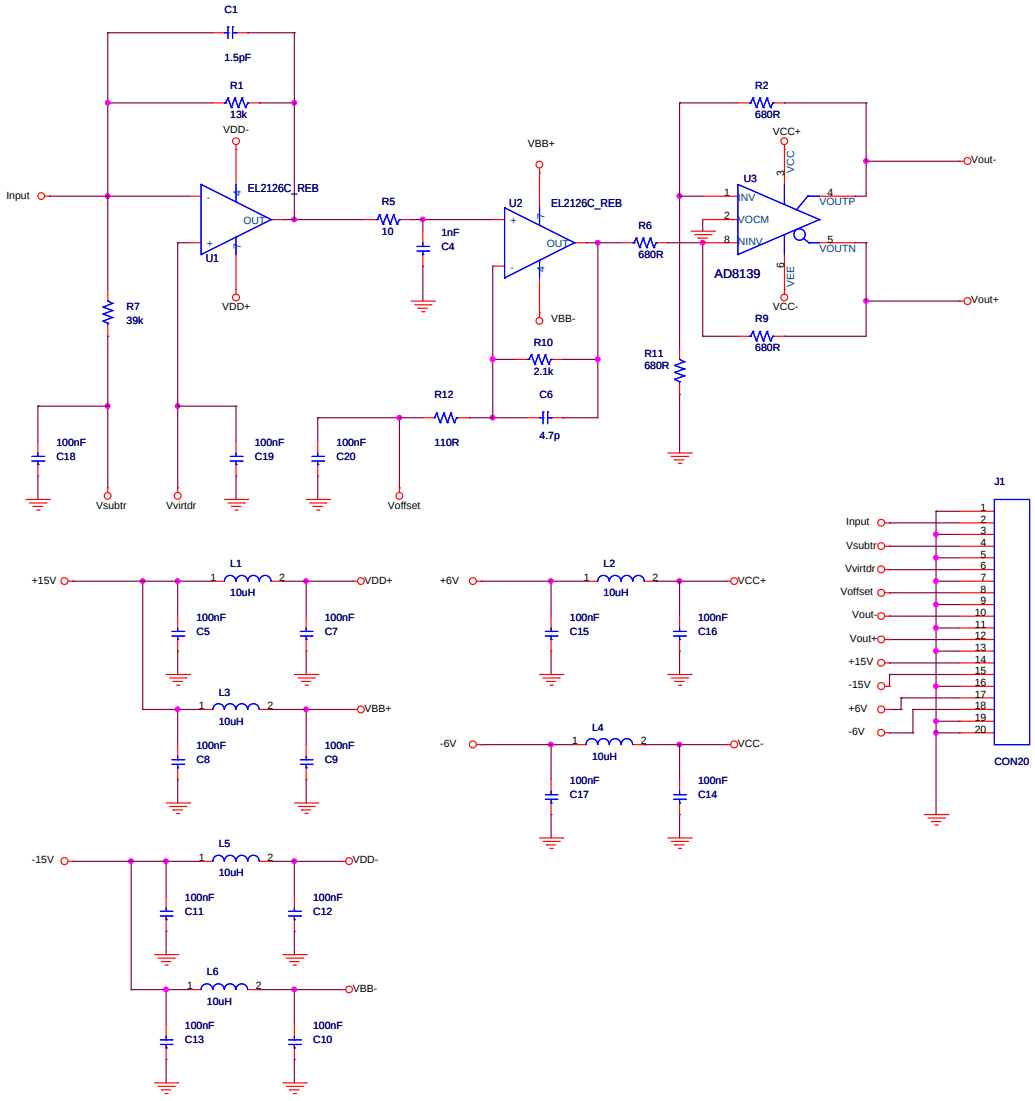

Figure B.3.: First version of the preamplifier (layout: J. Scheirich)

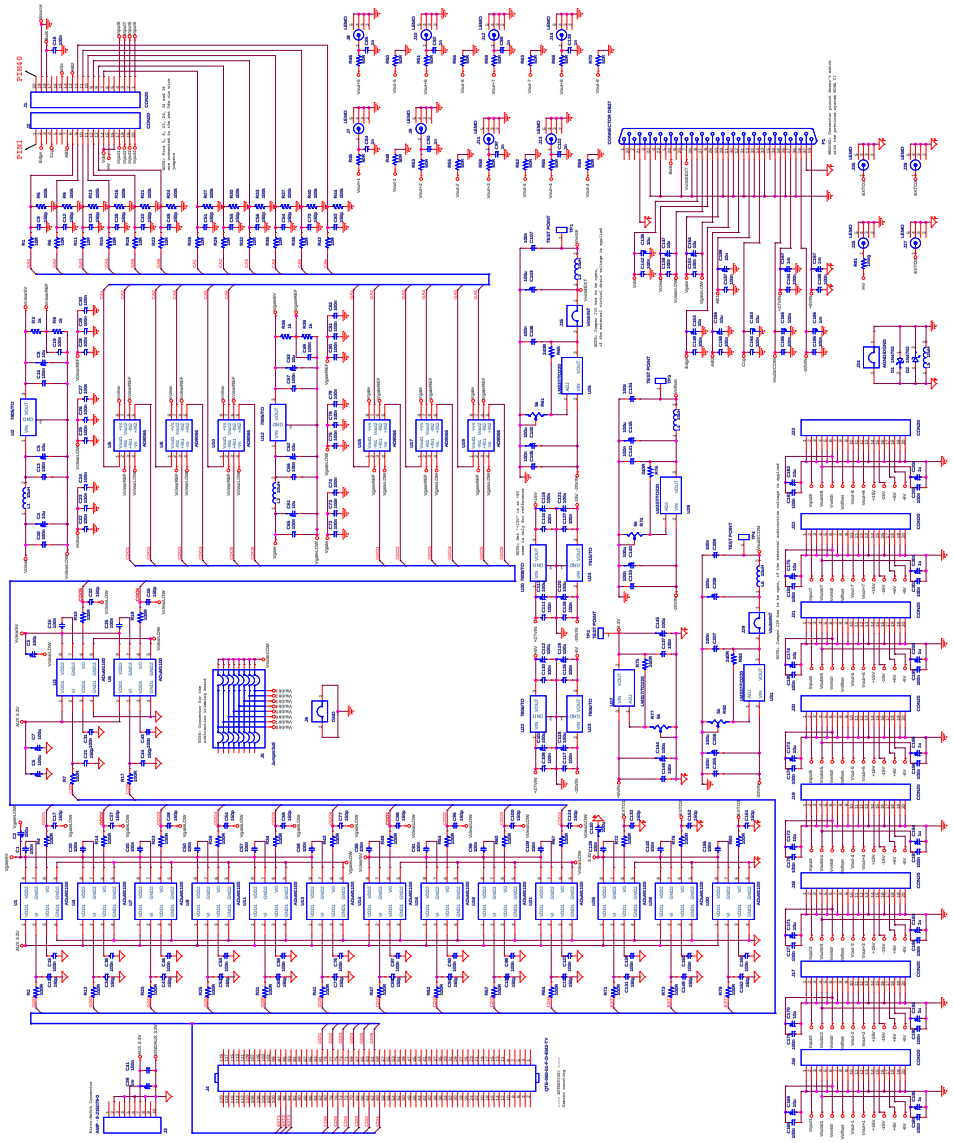

Figure B.4.: Motherboard of the mini matrix setup (layout: J. Scheirich)

B.4. Calibration of the preamplifiers

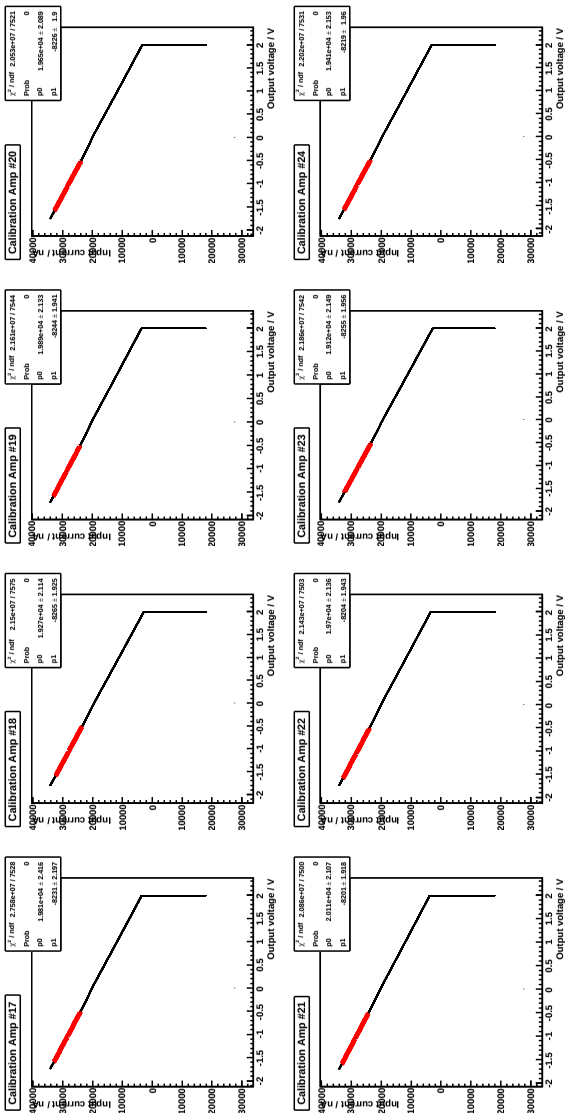

Figure B.5.: Calibration of the preamplifiers

B.5. Setup sequence

The voltages of the setup have to be switched on in a defined way to assure the correct settling of the preamplifiers:

1. fan + XBoard power supply
2. configuration of XBoard
3. bulk voltage
4. trigger voltage
5. CCG, gate high, gate low, -18 V, +11 V
6. clear low voltage
7. clear high voltage
8. high voltage

B.6. The MiMaTools software package

B.6.1. Hardware control programs

MiMaToolsC.exe

This is the control program for the hardware directly connected to the mini matrix main board (XBoard and GaGe scope card). It has to be called with two command line options:

```
MiMaToolsC.exe -? pathTo/steering.txt
```

The file `steering.txt` contains the paths of the configuration files. The option `-?` defines in which mode the program runs. The following options are available:

-s prints the configuration file to stdout

-x configures the XBoard using the sequence file given in `steering.txt`

-d configures the GaGe scope card and then does loop: 1. wait for user input, 2. acquire bunch of data

-t configures the GaGe scope card, only events above a given threshold are saved (source measurement), exit when maximum number of bunches is reached or user interrupts

StandaMove.exe, motor.py

This program was mainly developed by P. Kodyš for the Standa 8SMC1-USBhF motor stage driver [37]. It takes two arguments, namely, the axis `iAxis` (0 = back/front, 1 = down/up, 2 = left/right) and the shift `fShift` in mm:

```
StandaMove.exe iAxis fShift
```

A python class `motor.py` was developed to facilitate the handling of the motor stage. It provides initialisation, positioning and a scanning of a given range. The current motor position is saved to the `motorposition.txt` file in the `Config/` directory. Further, a log file in the `Log/` directory lists all movements of the motor stage.

SDPPowSuppl.exe

The Manson SDP2405 power supplies [38] can be programmed by calling this program with 3 arguments:

```
SDPPowSuppl.exe -? iId fValue
```

A connected power supplies is selected by its id `iId` and a command corresponding to the argument `-?` is executed:

-v sets the voltage to `fValue` Volts

-l sets an upper voltage limit of `fValue` Volts

-c sets a current limit of `fValue` Amperes

B.6.2. Configuration files

The DAQ software requires a number of configuration files which are listed and briefly commented here:

Run number

The current run number.

Bunch number

The current bunch number.

GaGe scope card

Configures the scope card: voltage range, number of samples per frame, number of frames per bunch.

Amplifier data

Which amplifier is connected to which scope channel? Gain corrections.

Hit threshold

Threshold settings and sampling for each gate.

Stop request

Stops the DAQ when the file contains a "`1`" (for `MiMaToolsC.exe` with `-t` option).

COM port

Defines the settings of the COM port for the XBoard (emulated RS232 port).

XBoard sequence

XBoard sequence in (semi-)raw format (human readable)

Channel assignment

Which XBoard channel is connected to which gate/clear/trigger channel?

Motor position

Current motor position.

B.6.3. Steering scripts for the DAQ

Different versions of the steering scripts exist. They are numbered consecutively. It is always a good idea to start from the latest version (= highest number), create a copy and then adapt the parameters and configuration files according to need. Generally, it is preferable not to introduce major changes in configuration files and steering scripts, but rather to create a new file. Measurements can then subsequently repeated with ease. A selection of the most relevant scripts is presented here.

All steering scripts contain the paths to the adapted configuration files and write these paths to the `steering.txt` file which, is then read by the `MiMaToolsC.exe` program.

noise_dark.py

Noise and system stability measurements in a black box can be performed with this script. It consists basically of a loop:

1. Acquire `nAdcEvents` (defined in GaGe scope configuration file) frames = 1 bunch

2. Wait `sleepTime` seconds

3. If maximum number of bunches `maxBunchNo` not reached, continue at 1.

laserscan.py

This script is used for laser scans. It scans the given range with the Standa motor stage and saves for each laser position a predefined number of frames (=bunch). The relation between bunch number and laser position is stored in the `%iRunNo_motor.log` file located in the `Log/` directory.

movelaser.py

While the `StandaMove.exe` program is only able to move the motor stage relative to the current position, this script allows the motor stage to be moved to an absolute position. This is possible because the script accesses the current absolute position saved in the `motorposition.txt` file.

source.py

Source measurements differ from the other measurements in the fact that only frames with hits are to be saved. This requires calling the `MiMaToolsC.exe` program with the `-t` option and the specification of a file containing the hit thresholds.

B.6.4. Details of the analysis classes

DaqSeq

The XBoard sequence is stored in the .seq files. It provides functionality to read and write .seq files. The .seq files contain low-level commands which are sent to the XBoard and are difficult to understand. Also, a simple integrity check of the sequence is provided. This class is also used by the DAQ.

TDaqSeq

A description of DaqSeq by `TChannel` objects. A conversion method to DaqSeq objects is provided.

TChannel

User-friendly timing information of 1 XBoard channel. The sequence is stored in steps which define the output (on/off) and the duration of the step in units of 10^{-10} ns. The time has to be a multiple of $75 \cdot 10^{-10}$ ns (duration of a XBoard tick).

Logfile

Extracts information from the log file and makes it available to the other analysis classes.

Timing

Defines the soft triggers, which designate the samples to be evaluated.

Scopesignal

The signal as it is acquired by the GaGe scope card is described by this object. The collection of samples of one frame acquired by one channel corresponds to one `Scopesignal` object.

Rawdata

The raw data ROOT files can be loaded or ASCII raw data files can be converted to ROOT raw data files. The data is stored in a TTree. A standard analysis consists in looping over all entries of the raw data file. A call of the `getScopeSignal()`

method returns the current scope signal in the TTree as `Scopesignal` object and jumps to the next entry.

Pixel

The `Pixel` object always contains the pixel signal. Furthermore, it may contain the scope signal evaluated before and after clear, the standard deviation of the scope signal averaging and the pixel number.

Minimatrix

The pixel signals of one frame are represented by the `Minimatrix` object. The pixel information is stored in `Pixel` objects. The pixel numbering is according to fig. B.1.

Mimadata

The mini matrix data file contains a TTree with the pixel signals. It can be loaded from the `Results/` directory, or pixel information can be extracted from a given `Rawdata` object. The current entry of the TTree can be retrieved by the `getMima()` method which returns a `Minimatrix` object.

Cluster

The `Cluster` object holds a sorted list of (pixel number, pixel signal) pairs and provides clustering functionality, e.g. all pixels which are not direct neighbours of the seed pixel are removed from the list.

B.6.5. Macros related to the XBoard sequence

createStdSequence

This macro creates the standard readout sequence which subsequently reads out the gates. The readout sequence for the gate and clear sequencer channels have to be defined by providing the number of steps, the time per step in units of 10^{-10} s and the output (high/low). Further, the overlap of two subsequent gate steering pulses has to be defined. Example:

```
const Int_t nStepsClear = 3;
iDurationClearT[0] = 38550;
iValueClearT[0] = 0;
iDurationClearT[1] = 2550;
iValueClearT[1] = 1;
iDurationClearT[2] = 38550;
iValueClearT[2] = 0;
```

The channel assignment file and the output file have to be defined in the lines:

```
tds->assigch("../Config/test3.cas");
sprintf(filename, "../Config/standard.seq");
```

showSequence

A sequence and a channel assignment file have to be supplied:

```
tds->assigch("../Config/test3.cas");
ds->init("../Config/test3a.seq");
```

A graphical representation of the sequence is going to be displayed.

B.6.6. Macros for the analysis

In this section the ROOT macros located in the `macros/` directory are presented. Other macros in the directory can be ignored because they are broken or created only for the purpose of system tuning.

RawAsc2RawRoot

The ASCII data files are is read in, converted and written to a ROOT TTree and then saved to a ROOT file. The tree has the following branches: the bunch number iBunchNo, the event number iEvent, the ADC channel nAdcChannel, a timestamp fTriggerTime, and the array containing the scope signal samples nAdcCounts[] in ADUs. All further analysis uses the data from this TTree.

RawRoot2QuickView

After conversion of the ASCII files to a ROOT file, the soft triggers have to be set to the right position. The required plot (Fig. 4.8) is created by this macro. In addition the average scope signal and a histogram of the acquired scope signal is displayed. Parameters: *run number*, *bunch number*.

The soft triggers have to be set inside the source code in the line:

```
timing->defineSoftTriggers(logfile->nAdcSamples,
                           50500000,
                           -10000,
                           5, 30, 65, 30
                          );
```

The first parameter is the *number of samples* and is read automatically from the log file. It is followed by the *sampling rate* (50500000) of the scope card and the *offset* (-10000) between the opening of gate 0 and the start of acquisition. The next two pairs of numbers define the distance of the evaluated area before (after) clear and the number of samples to evaluate before (after) clear.

RawRoot2MimaRoot

The tree created by `RawAsc2RawRoot` contains only scope signals. For most purposes the pixel signal has to extracted by this macro. The correct settings for the soft triggers have to be determined with the macro `RawRoot2QuickView`. The parameters to be supplied are: *run number*, *distance before clear*, *distance after clear*, *number of samples to evaluate*, *sample rate* and *offset*.

The output of the macro is a TTree saved to a ROOT file which can be found in the `Results/` directory. The TTree contains the pixel signals as an array.

MimaRoot2MatrixView

Shows a graphical representation of the pixel signals and their standard deviation calculated according to equation 4.4. *Run number*, *bunch number* and *event number* define the frame/event to be displayed.

MimaRoot2MatrixViewAverage

The functionality is the same as for `MimaRoot2MatrixView`, but the displayed pixel signal is the average of several frames. If only the *run number* is given, the average is taken of all frames of the run. The averaging can be limited to only one bunch by supplying the *bunch number*.

MimaRoot2NoiseAnalysis

The pixel signal histogram is displayed according to the given *run number*, *pixel number* and *bunch number*. If the bunch number is omitted all bunches of the run are considered. Further the histogram is fitted with a Gaussian distribution.

TwoMimaRoot2MimaRoot

If only a 4-channel ADC card is available, the laser test can be split to two runs. Both runs have to follow exactly the same scanning scheme and have to contain the same number of bunches. A new mini matrix data file is created from the provided *run numbers*. The run number of the merged data is the run number first provided +990000.

MimaRoot2LaserscanView

Analyses the data from a laser scan. The *run number* and the run number of a separate *pedestal measurement* have to be supplied. Further it is necessary to give the *number of bunches* which were acquired.

MimaRoot2SelectedHitsImproved

Before processing a spectrum the pedestal signal has to be subtracted from the data by this macro. Further, the clustering algorithm of the `Cluster` class can be too slow for processing a large amount of data. This macro also selects events which contain at least one pixel with a signal above a given threshold. The run number of the processed output (a `Mimadata`) ROOT file is the run number of the input file +950000. The parameters to be passed are the *run number* and *threshold* in ADU. If the threshold is set to a very low value (e.g. −16000), the script effectively subtracts only the pedestals, but keeps all events of the run.

MimaRoot2SpectrumFast

The only parameter of this script is the *run number*. Different cuts and clustering settings can be changed inside the source code of the macro which is well documented.

Pixels can be excluded from the analysis, or, with seed pixels, by adding them to the corresponding list of excluded pixels:

```
list<int> isExcludedFromAnalysis;
isExcludedFromAnalysis.push_back(39);
isExcludedFromAnalysis.push_back(2);
isExcludedFromAnalysis.push_back(17);
list<int> isExcludedFromSeed;
isExcludedFromSeed.push_back(2);
```

MimaRoot2CommonModeSelected

The common mode noise (CMN) of a run given by the *run number* is subtracted. The user can select whether gate CMN subtraction, scope channel CMN subtraction or both corrections are applied.

Acknowledgements

I would first like to thank my advisers Zdeněk Doležal and Peter Kodyš for kindly integrating me into their research group. I am grateful for their abundant help and advice.

I also would like to thank Christian Kiesling for his support and encouragement while writing my diploma thesis in Prague.

I am really grateful for all the friendly support I had from my colleagues in Prague, with a special mention of Ján Scheirich, the designer of the mini matrix setup electronics, who introduced me to the DEPFET sensor and the mini matrix system and Zbyněk Drásal who helped me in my first steps in implementing the geometry.

I also wish to thank my colleagues from the Max-Planck Institute. This work would not have been possible without the close collaboration with the team from the semiconductor laboratory, notably, Christian Koffmane, Jelena Ninković and Andreas Ritter. Moreover, Andreas Moll was a great help with the basf2 framework.

I am indebted to the DAAD[1] for the scholarship I obtained for my stay in Prague.

[1]German Academic Exchange Service

Bibliography

[1] K. Nakamura et al. Review of Particle Physics. *Journal of Physics G: Nuclear and Particle Physics*, 37:075021, 2010.

[2] T. Aushev, W. Bartel, A. Bondar, J. Brodzicka, TE Browder, P. Chang, Y. Chao, KF Chen, J. Dalseno, A. Drutskoy, et al. Physics at Super B Factory. *Arxiv preprint arXiv:1002.5012*, 2010.

[3] J. Charles, A. Höcker, H. Lacker, S. Laplace, F. R. Le Diberder, J. Malclés, J. Ocariz, M. Pivk, and L. Roos. CP violation and the CKM matrix: assessing the impact of the asymmetric B factories. *The European Physical Journal C - Particles and Fields*, 41:1–131, 2005.

[4] A. Bettini. *Introduction to elementary particle physics*. Cambridge Univ Pr, 2008.

[5] T. Abe et al. Belle II Technical Design Report. Technical Report KEK Report 2010-1, KEK, November 2010.

[6] L. Rossi, P. Fischer, and T. Rohe. *Pixel detectors: From fundamentals to applications*. Springer Verlag, 2006.

[7] SM Sze and K.K. Ng. *Physics of semiconductor devices*. Wiley-Blackwell, 2007.

[8] W.R. Leo. *Techniques for nuclear and particle physics experiments: a how-to approach*. Springer Verlag, 1994.

[9] JF Bak, A. Burenkov, JBB Petersen, E Uggerhoj, SP Moller, P Siffert, et al. Large departures from Landau distributions for high-energy particles traversing thin Si and Ge targets. *Nuclear Physics B*, 288:681–716, 1987.

[10] Private communication with Peter Kodyš.

[11] Hans-Günther Moser. Silicon detector systems in high energy physics. *Progress in Particle and Nuclear Physics*, 63(1):186–237, 2009.

[12] MJ Berger, JH Hubbell, SM Seltzer, J. Chang, JS Coursey, R. Sukumar, and DS Zucker. XCOM: Photon cross sections database, NIST standard reference database 8 (XGAM). *Available on URL www. physics. nist. gov/PhysRefData/Xcom/Text/XCOM. html*, 2010.

[13] Adrian Sorin Niculae. *Development of a low noise analog readout for a DEPFET pixel detector*. PhD thesis, Universität Siegen, 2003.

[14] Stefan Rummel. *Investigation of DEPFET as Vertex Detector at ILC – Intrinsic properties, radiation hardness and alternative readout schemes*. PhD thesis, Technische Universität München, 2009.

[15] J. Kemmer and G. Lutz. New detector concepts. *Nuclear Instruments and Methods in Physics Research Section A: Accelerators, Spectrometers, Detectors and Associated Equipment*, 253(3):365–377, 1987.

[16] E. Gatti and P. Rehak. Semiconductor drift chamber–An application of a novel charge transport scheme. *Nuclear Instruments and Methods in Physics Research*, 225(3):608–614, 1984.

[17] DEPFET Pixel Vertex Detector for the ILC, October 2007.

[18] Robert Kohrs. *Development and Characterization of a DEPFET Pixel Prototype System for the ILC Vertex Detector*. PhD thesis, Universität Siegen, September 2008.

[19] L. Andricek et al. The MOS-type DEPFET pixel sensor for the ILC environment. *Nucl. Instrum. Meth.*, A565:165–171, 2006.

[20] M. Trimpl. *Design of a current based readout chip and development of a DEPFET pixel prototype system for the ILC vertex detector*. PhD thesis, Universitäts-und Landesbibliothek Bonn, 2005.

[21] M. Moll et al. Development of radiation tolerant semiconductor detectors for the Super-LHC. *Nuclear Instruments and Methods in Physics Research Section A: Accelerators, Spectrometers, Detectors and Associated Equipment*, 546(1-2):99–107, 2005.

[22] R. Turchetta. CMOS Monolithic Active Pixel Sensors (MAPS) for future vertex detectors. *Journal of Instrumentation*, 1:P08004, 2006.

[23] J. Baudot, G. Bertolone, A. Brogna, G. Claus, C. Colledani, Y. Degerli, R. De Masi, A. Dorokhov, G. Doziere, W. Dulinski, et al. First test results of MIMOSA-26, a fast CMOS sensor with integrated zero suppression and digitized output. In *Nuclear Science Symposium Conference Record (NSS/MIC), 2009 IEEE*, pages 1169–1173. IEEE, 2010.

[24] L. Andricek, G. Lutz, M. Reiche, and RH Richter. Processing of ultra thin silicon sensors for future e+ e- linear collider experiments. In *Nuclear Science Symposium Conference Record, 2003 IEEE*, volume 3, pages 1655–1658. IEEE, 2004.

[25] J. Scheirich. *Title not yet available*. PhD thesis, Czech Technical University in Prague, 2013.

[26] Andreas Wassatsch. *Mini-Matrix-Sequencer Manual* . MPI für Physik, HLL, Otto-Hahn-Ring 6, D-81739 München, 2009.

[27] J. Scheirich. Design of Readout Electronics for the Mini-matrix DEPFET Detector. Master's thesis, České vysoké učení technické, 2008.

[28] R. Brun and F. Rademakers. ROOT–An object oriented data analysis framework. *Nuclear Instruments and Methods in Physics Research Section A: Accelerators, Spectrometers, Detectors and Associated Equipment*, 389(1-2):81–86, 1997.

[29] E. Belau, R. Klanner, G. Lutz, E. Neugebauer, HJ Seebrunner, A. Wylie, T. Böhringer, L. Hubbeling, P. Weilhammer, J. Kemmer, et al. Charge collection in silicon strip detectors. *Nuclear Instruments and Methods in Physics Research*, 214(2-3):253–260, 1983.

[30] Private communication with Rainer Richter, October 2010.

[31] OZ Optics. *Data sheet: Collimators and focusers - Pigtail Style*, February 1995.

[32] Pavel Bazant et al. Laser measurement of absolute charge collection efficiency of a silicon detector. *Nucl. Instrum. Meth.*, A581:306–309, 2007.

[33] R.B. Firestone and L.P. Ekström. LBNL Isotopes Project - LUNDS Universitet.

[34] M. Trimpl et al. Performance of a DEPFET pixel system for particle detection. *Nucl. Instrum. Meth.*, A568:201–206, 2006.

[35] Hans-Gunther Moser et al. DEPFET active pixel sensors. *PoS*, VERTEX2007:022, 2007.

[36] Andreas Moll, Takanori Hara, and Thomas Kuhr. Geometry Handling. First Belle II Software Tutorial, July 2010.

[37] *8SMC1-USBhF 1.5A Microstep Driver with USB Interface* , 2008.

[38] *Remote Programming Switching Mode DC regulated Power Supplies, SDP Series*, 2009.

Selbstständigkeitserklärung

Ich erkläre hiermit, dass ich die vorliegende Arbeit selbstständig verfasst und keine anderen als die angegebenen Quellen und Hilfsmittel verwendet habe.

Ort, Datum Unterschrift